TRIBOLOGICAL PERFORMANCE ANALYSIS OF COATED HYDRO TURBINE BLADE MATERIALS

A thesis submitted in fulfilment of the requirements for the award of the degree of
DOCTOR OF PHILOSOPHY

By
Rajesh Kumar
(Registration No.: 951708001)

Under the supervision of

Dr. Deepa Mudgal
(Assistant Professor)
Mechanical Engineering Department
Thapar Institute of Engineering and Technology
Patiala, Punjab, India

Dr. Satish Kumar
(Associate Professor)
Department of Mechanical Engineering
National Institute of Technology
Jamshedpur, Jharkhand, India

MECHANICAL ENGINEERING DEPARTMENT
THAPAR INSTITUTE OF ENGINEERING AND TECHNOLOGY
PATIALA-147004, PUNJAB, INDIA

September 2023

THAPAR INSTITUTE OF ENGINEERING AND TECHNOLOGY, PATIALA, INDIA

(Established in 1956)

CERTIFICATE

This is to certify that the work presented in dissertation entitled *"Tribological performance analysis of coated hydro turbine blade materials"* in partial fulfilment of the requirements for the award of degree of **Doctor of Philosophy** of my own work carried out under the supervision and guidance of **Dr. Deepa Mudgal** (Assistant Professor, Mechanical Engineering Department, Thapar Institute of Engineering and Technology, Patiala) and **Dr. Satish Kumar** (Associate Professor, Department of Mechanical Engineering, National Institute of Technology, Jamshedpur).

Rajesh
28/09/2023

Rajesh

Rajesh Kumar

Date: 28.09.2023.

Registration No.: 951708001

This is certified that the above statement made by the student is correct to the best of our knowledge and belief.

Deepa
28/09/2023

Dr. Deepa Mudgal
(Assistant Professor)
Mechanical Engineering Department
Thapar Institute of Engineering and Technology
Patiala

28/09/2023

Dr. Satish Kumar
(Associate Professor)
Department of Mechanical Engineering
National Institute of Technology
Jamshedpur

Dr. Satish Kumar
Associate Professor
Mechanical Engg. Department
NIT. Jamshedpur (Jharkhand)

ACKNOWLEDGEMENT

I accord my recondite gratitude to the almighty God whose grace enabled me to achieve the chosen ambition and for whatever I am today. No words can suffice my feelings of gratitude towards my father, my mother whose blessings and unconditional love were the driving force during the entire period of my study. I also acknowledge the sincere thanks to my brother *Sumit Kumar* for his great support and motivation which always have acted as a beacon of light for me for completion of this Ph.D. work. I am also grateful to my wife for her support during the journey of my Ph.D.

The most pleasant part of work is the opportunity to express my gratitude to *Dr. Deepa Mudgal* and *Dr. Satish Kumar* for being my thesis supervisor. Under their consistent supervision, able guidance, concrete suggestions, constructive criticism and persistent encouragement this work was planned and successfully completed. I owe a deep sense of gratitude to them for their constant efforts at each and every step.

The work has not been possible without the help of my seniors *Dr. Jashanpreet Singh* and *Dr. Varinder Singh* who encouraged me at each and every stage of work to solve every problem during the journey of my Ph.D.

I am also thankful to *Mr. Narinder Singh*, *Mr. Sarabjit Singh* and *Mr. Sukhbir Singh* (Lab Technicians of different laboratories, Mechanical Engineering Department, Thapar Institute of Engineering and Technology, Patiala) for their instructions and indispensable help during all experimentation conducted for dissertation work.

I would like to acknowledge *Mechanical Engineering Department, Thapar Institute of Engineering and Technology, Patiala* and *Sophisticated Analytics Laboratories, Patiala* for providing the necessary facilities to carry out the various testing and experiments.

Rajesh Kumar

Dedicated to Shri Mata

Vaishno Devi Ji

&

My Loving Family

ABSTRACT

Hydro turbines are one of the most vital and essential components for the production of hydroelectric power. Since the hydro turbine is always operating under the influence of water and the silt transported by the water from the hilly region, it poses a lot of threat and damage to the turbine blades working constantly under the action of silt laden water. Erosion wear is the most common type of damage, and drastically affects the life of turbine runners and blades. The introduction of thermal spray coatings, namely high-velocity oxy-fuel (HVOF) technique has resulted in a major improvement in stainless steel erosion resistance. On stainless steel substrates of grade 304, ceramic coating powders primarily Al_2O_3, Cr_2O_3, and a composite mixture of composition 55% Cr_2O_3+45% Al_2O_3 were deposited. The thorough experiments utilizing silt slurry are conducted at different particle size of silt in the range 212-250 µm, 150-212 µm, and 53-106 µm. The silt concentration has been varied in the range 12-42% by weight and the substrate rotated at rotational speed in the range 600-1500 rev/min for the test time of 4 hours. SEM images were used to assess the surface morphology of the required testing samples. The erosion observance and the material removal mechanism were investigated and discussed on the basis of microstructure studies. Under all test conditions, Cr_2O_3 coating is found to be more resistant to erosion than other coatings. Also, the composite coatings of composition 65% Cr_2O_3+35% Al_2O_3 has been modified by the addition of CeO_2 to the percentage of 0.5%,1% and 1.5%, a rare earth element for analysing the silt erosion behaviour at particle size 212-250µm, 150-212µm, 53-106µm and the concentration of the silt range from 10-40% by weight. The rotational speed of the pot tester has been varied between 500-1500 revolutions per minute and the test duration has been kept to 4 hours. It has been found that the erosion wear resistance of the uncoated SS-304 has been greatly enhanced by the application of HVOF sprayed Al_2O_3-Cr_2O_3 composite coatings. Also, the addition of CeO_2 has a significant impact in reducing the erosive wear caused by silt slurry. The composite coating powder composition of 65%Cr_2O_3+34.5%Al_2O_3+ 0.5%CeO_2 has shown the highest erosion resistance. The developed coatings have the potential to be used for hydro turbines as subjected to silt slurry conditions. Also, the Taguchi approach has been applied for tribo-erosion wear of Al_2O_3-Cr_2O_3 composite coatings. It has been analysed that of all the control variables such as particle size and silt concentration, rotational speed is the most dominant factor among all.

Keywords:

- Tribology
- Erosion
- Silt erosion
- Hydro turbines
- Dam silt
- Coatings
- Thermal spray
- HVOF process
- Ceramics coatings.

TABLE OF CONTENT

LIST OF FIGURES

LIST OF TABLES

NOMENCLATURE

Symbols	Descriptions
A	Area (m^2)
A_p	Area of particle (m^2)
C	Electrochemical mass loss
C_w	Solid concentration (wt. %)
d or d_p	Particle diameter function (µm)
$D_{maxfret}$	Maximum Feret diameter
E or E_w or E_T	Erosion wear (g/m^2 or mm^3 or g/mm^2 or mm^3/year)
f_i	Solid percentage
$f(\alpha)$	Impact angle function
H_T or HV	Vickers hardness of target
K	Material constant
K_c or K_T	Fracture toughness
m	mass loss from the target surface
M	Mechanical failure
M_p or m_p	mass of erodent particle per unit time rate (g/sec)
N	Rotational speed (rev/min)
N_i	B.S.S. number of the particle size range
P	Perimeter (µm)
r	Particle radius (µm)
Ra	Surface roughness (µm)
Re	Reynolds number
Rq	Maximum peak in roughness testing length (µm)
R_w	Weight of the solid that was kept in the sieve (g)
Rz	Maximum – minimum roughness value (µm)
S	Synergistic effects of erosion and corrosion
S_1	Silt concentration coefficient
S_2	Silt hardness coefficient
S_3	Silt particle size coefficient
S_4	Silt particle shape coefficient

St	Stokes number
T	Time duration (min or hours)
T_w	Total weight of the solid that passed through all of the sieves (gm)
V_p	Particle velocity (m/sec)
V or v	Velocity (m/sec)

Greek letters

α	Impact angle (°)
ε	Deformation factor
ρ_f	Fluid Density
ρ_p	Particle density
φ	Constant of kinetic energy
ψ	Ratio of depth of contact to depth of cut
ψ	Average sphericity
σ	Deformation wear coefficients
σ_{cr}	Critical stress of material
γ	Cutting wear

Superscripts

a	CF exponent
m	Velocity exponent
n	Weight mean diameter exponent
p	Concentration exponent

Subscripts

Avg	Average
c	Cutting
ch	Convex hull
cr	Critical
D	Deformation
N	Normal
T	Tangential
p	Particle
w	Weight

Abbreviations

B.S.S.	British Standard Sieves
CF	Circularity factor
CFD	Computational fluid dynamics
CHEP	Chilmi Hydro Electric Plant (CHEP)
CR	Cavitation erosion
CVD	Chemical vapour deposition
EDS	Energy dispersive spectroscopy
HVAF	High-velocity air-fuel
HVOF	High-velocity oxy-fuel
HVFS	high-velocity flame spray
IEA	International Energy Agency Report
PF	Paris factor
RD	Roundness
SF	Shape factor
SMAW	Shielded Metal Arc Welding
SEM	Scanning electron microscopy
TVL	Total volume loss (mm^3)
XRD	X-ray Diffractometery

CHAPTER 1

INTRODUCTION

Hydropower is one of the major sources of renewable energy, and its development is more important than that of fossil fuels or other types of resources that do not replenish themselves. Hydroelectric power is a resource that has potential which is not yet been fully realized, and nations like India should invest in it so that they can meet the vast energy needs of their country. After thermal energy, hydropower is the second most important source of energy in India, accounting for 17.55% of the country's total installed power capacity of 225,793.10 MW (*Ministry of Power report*, 2019). Currently, thermal energy is the most important source of energy in India. Ten countries are responsible for 66% of the total net installed capacity of hydroelectricity on the globe, which is 1267 GW. India made it to number seven on the list (*International Energy Agency report (IEA)*, 2019). Because India has such a significant need for energy, the country's vast, unused hydroelectric power potential must be used. The hydroelectric potential of India is 145,000 MW, which is adequate to meet the demand of the nation, which is 88,537 MW (*Ministry of Power report*, 2019). This is based on a load factor of 60%. According to the most recent figures available, the installed capacity of India's power plants is 39,896.40 MW. The Central Electricity Regulatory Commission (CERC) of India has given its approval for an increase of 5921.755 MW in the amount of hydropower that may be generated in 2019. With 15,569.75 MW of installed capacity, the hydroelectric utilities in the Northern region of India have the largest total capacity of any area in the country. Punjab is home to the bulk of northern India's installed capacity, which accounts for 19.42% of the total. Himachal Pradesh (H.P.) and Uttarakhand, both of which are situated in the Himalayas, have the largest hydroelectricity-producing capacity in the whole nation. The path to hydropower development is still littered with several roadblocks. It is necessary to find a solution to the issue of silt erosion.

Engineers, researchers, and scientists are unanimous in their agreement that the protection of the machines, equipment, and other systems that are placed in hydropower plants is a need. An in-depth understanding of the underlying processes is required to find solutions to failure situations that are both effective and cheap. Failure due to fatigue, scaling, abrasion, adhesion, fatigue, erosion, corrosion, and erosion-corrosion are some of the most prevalent causes of surface failure. Other reasons include adhesion and fatigue. A significant problem that affects northern Indian hydropower installations is silt erosion in the hydro-turbines and the components of such turbines. Erosion in a water-immersed components of a hydroturbine is a common phenomenon in the auxiliary industrial environment (*Ministry of Power report*, 2019). Substantial research has previously been conducted experimentally and analytically to determine the factors that cause severe erosive wear damages in hydro turbines caused by silt-laden water (Awal et al., 2019; Fecarotta et al., 2018; Gallani et al., 2018; *International Energy Agency report (IEA),* 2019; Malavasi et al., 2018; Mansouri et al., 2015, 2014; Messa et al., 2019). In the Himalayas, the riverbeds are composed of abrasive elements such as quartz, feldspar, and other similar minerals. River silt that the river transports during the monsoon season has the potential to seriously harm turbine parts. When hydro-turbine components, such as blades, runners, seals, liners, and passageways, are subjected to high levels of silt, the rate of wear and tear on these parts accelerates (Awal et al., 2019). Quartz makes up more than 50% of the silt, which presents several challenges for turbines (Chitrakar et al., 2018; Kapali et al., 2019; Padhy and Saini, 2009). Examples include silt erosion, flow leaks, interruptions in secondary flow, structural failures, runner and blade deformation, impeller and casing erosion, power output decreases, and so on. To generate electricity, hydroelectric power plants use a combination of pumped storage and run-of-river (ROR) energy generation processes. Both of these models illustrate that silt erosion may occur as a result of particle sedimentation (Sangroula, 1970). Small hydropower projects of the ROR kind face a significant risk from silt erosion. Silt erosion has harmed several power plants, including Maneri Bhali Stage-I and Stage-II, Nathpa Jhakri, Bariasul, Dehar, Salal, Chilla, Khatima, and others (Swarnakar et al., 2008). Significant silt erosion problems exist at locations of the Himalayan mountain range, which is in the north and northeast of the country, and is suitable for the production of hydropower. All of these malfunctions contribute to an increase in operating and maintenance (O&M) costs and a decline in the hydropower plant's overall efficiency. Erosion produces difficulties for hydropower facilities, such as broken guiding vanes and runner blades, leakage flow, and clogged strainers in the turbines; all of these problems lead to greater operating and maintenance costs. Erosion may also generate leakage. The pace of silt erosion has an impact on this aspect of the hydropower plant since the shorter service life of the turbine and the components that make it up brings down the overall efficiency of the plant.

1.1 CLASSIFICATION OF HYDRO-TURBINES

The quantity of water and the head conditions are the two most important factors in determining the amount of electricity that hydroelectric power plants can generate from a particular water source. The hydro-turbines are adapted to the distinct river conditions that are present in each region. The major factors in selecting a hydro-turbine are the conversion of energy, the water head that is accessible on the unit, the turbine-specific speed, and the water volume that can be used in the generation of continuous power. **Figure 1.1** illustrates the factors that should be considered when selecting hydro-turbines based on head and flow rates. **Table 1.1** presents an overview of several head conditions that might affect impulse turbines.

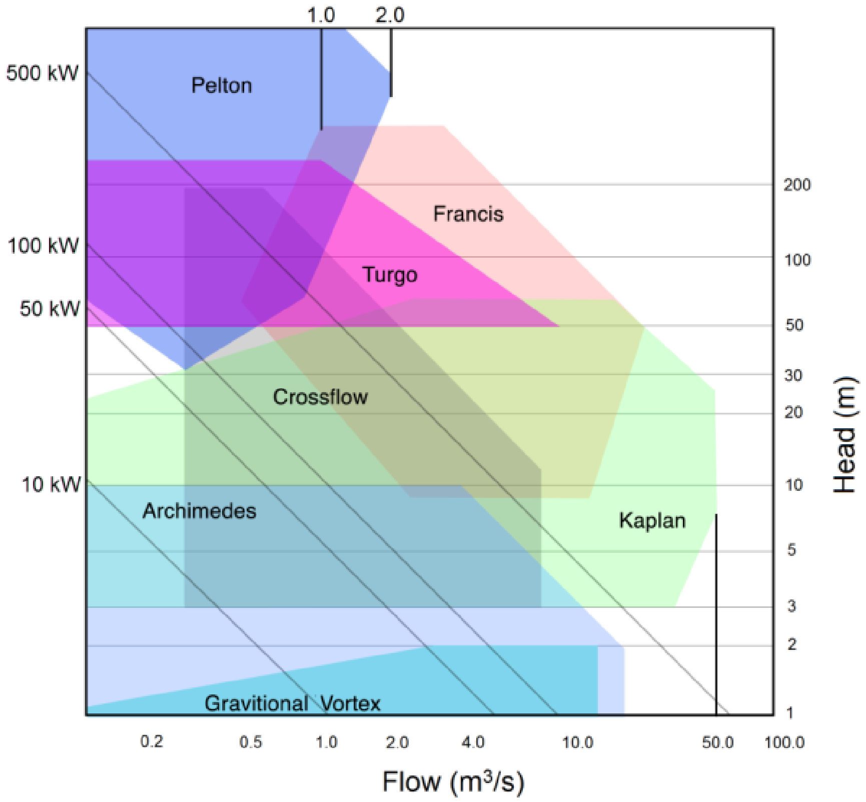

Figure 1.1. Selection criteria of various hydro-turbines (Fraenkel et al., 1991).

There are two fundamental categories of hydro turbines: impulse turbines and reaction turbines (Kjolle, 2014). It is vital to classify turbines to determine the cause of a malfunction and silt erosion. Cavitation, abrasion, corrosion, fatigue, and material faults are the most prevalent causes of failure in impulse and reaction turbines (Padhy and Saini, 2012; Szala et al., 2014). Cavitation, erosion, abrasion, and corrosion may be affected by the functioning of the power plant; however, fatigue in the material and material faults are not reliant on the water supply. The following is an in-depth review of the many different types of hydro-turbines as well as the potential failure modes of each:

Table 1.1: Head Conditions of Different Turbines

S. No.	Turbine Type	Turbines	Head (m)		
			High (>50 m)	**Medium (10–50 m)**	**Low (<10 m)**
1	Impulse turbines	Pelton	√		
2		Turgo	√	√	
3		Cross-flow		√	√
4		Multijet Pelton		√	
5		Undershot water wheel			√
6	Reaction turbines	Francis (spiral casing)		√	
7		Propeller			√
8		Kaplan			√
9		Francis (Open fume)			√
10	Gravity turbines	Overshot water wheel			√
11		Archimedes screw			√

1.1.1 Impulse Turbines

The high-velocity jets and high-pressure surroundings are necessary to power an impulse turbine. These turbines, on the other hand, may be adjusted to operate in a wide range of head conditions, from very low to very high. Pelton, Turgo, and cross-flow turbines are the three most frequent types of impulse turbines; however, there are a few more varieties as well. A graphical representation of the operation of an impulse turbine is shown in **Figure 1.2(a)**. In Pelton turbines, the runner or buckets are lined up in a row along the outer edge of the shaft. This allows the turbine to make very efficient use of space. When water is released from the dam at a high velocity via nozzles and directed into the turbine, where it collides with the blades, the turbine creates mechanical energy by spinning the shaft. This freshly produced mechanical energy is sent into a generator, which then converts it into electrical energy. The needles, nozzles, and runner buckets of Pelton turbines are the locations where cavitation may be found. **Figure 1.3** illustrates the usual surface wear that occurs on the buckets and nozzles of a Pelton turbine.

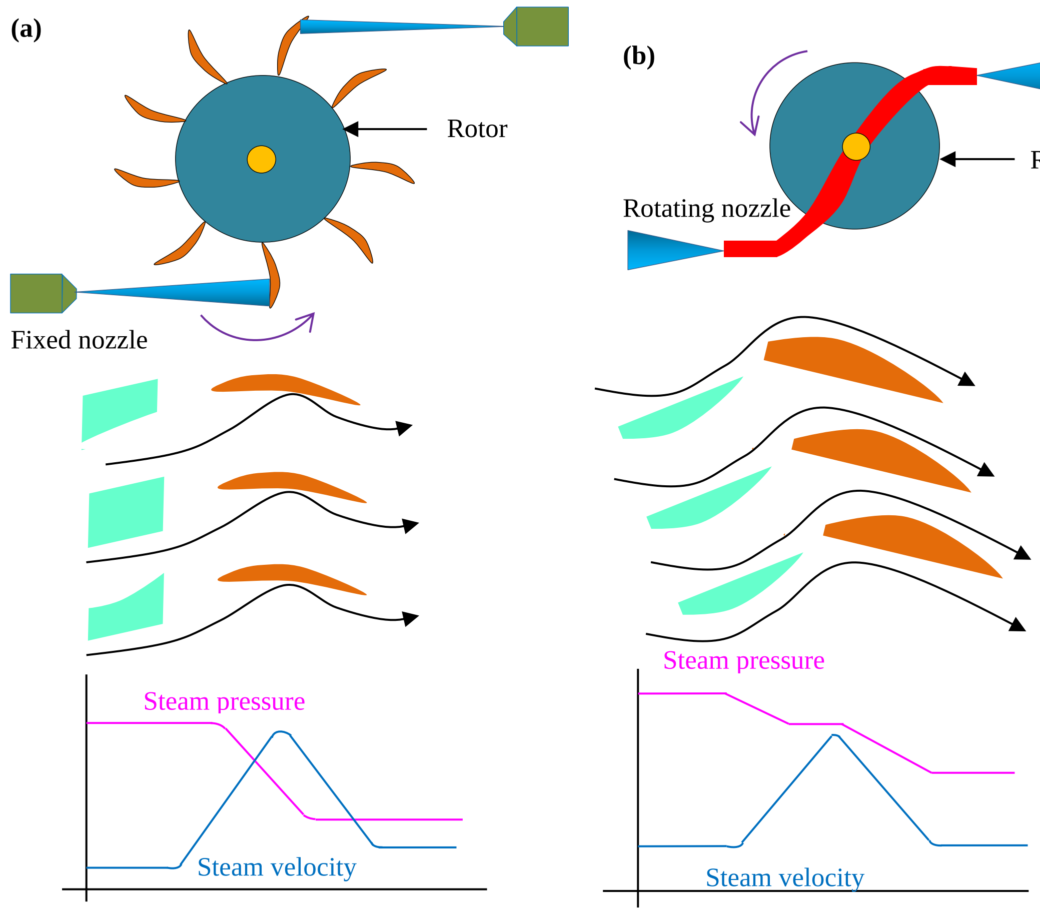

Figure 1.2. Working principle of (a) impulse and (b) reaction turbines.

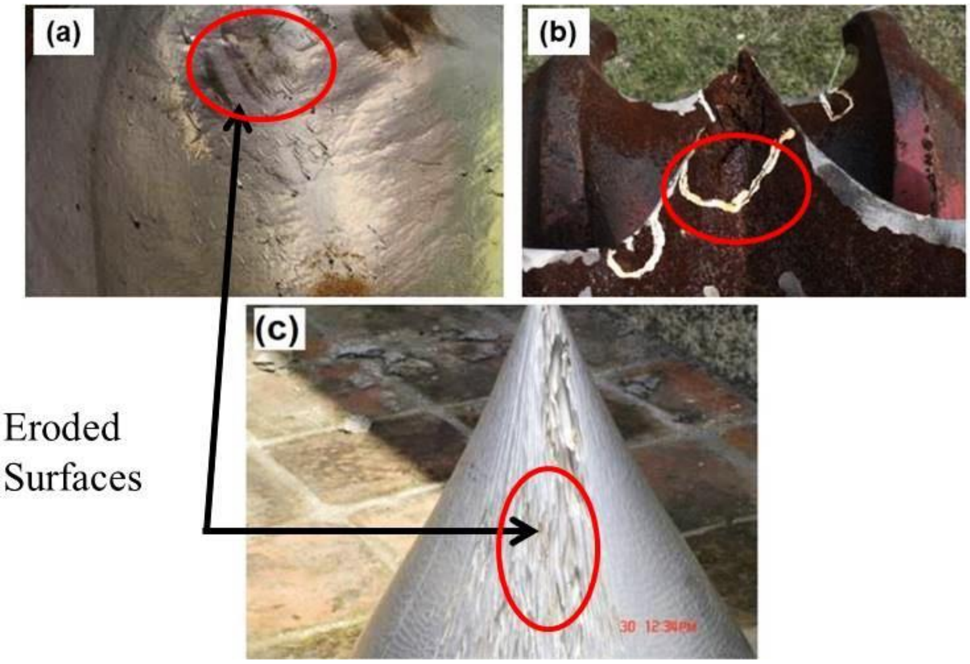

Figure 1.3. Typical wear on the surface of Pelton turbine; (a, b) cavitation on the bucket (Chávez et al. 2015), and (c) nozzle of Chilime Hydropower Plant, Nepal (Bajracharya et al., 2008a).

1.1.2 *Reaction Turbines*

The parameters of having a medium head are perfect for driving reaction turbines. The response turbine has rotors that are completely submerged in water and are housed inside a pressure vessel for protection. The runner blades, which are fashioned similarly to the wings of an aircraft, are designed to experience lifting forces, which causes them to rotate at a higher rate than a jet. The operation of reaction turbines is shown in diagrammatic form in **Figure 1.2(b)**. According to the research that has been done, both the runners and the draught tube cones of the Francis and Kaplan turbine are sensitive to cavitation (Kjolle, 2014). A typical picture of silt erosion in Baglihar Hydro Electric Power Plant, Jammu and Kashmir (India) is shown in **Figure 1.4**. The blades, guiding vanes, runners, seals, liners, and passageways of a Francis turbine are only some of the numerous elements that are vulnerable to silt erosion (Padhy and Saini, 2009). There is a chance that the structure may fail, that there will be leaks, that the runners and blades will be distorted, and that the power output will be reduced (Chitrakar et al., 2018).

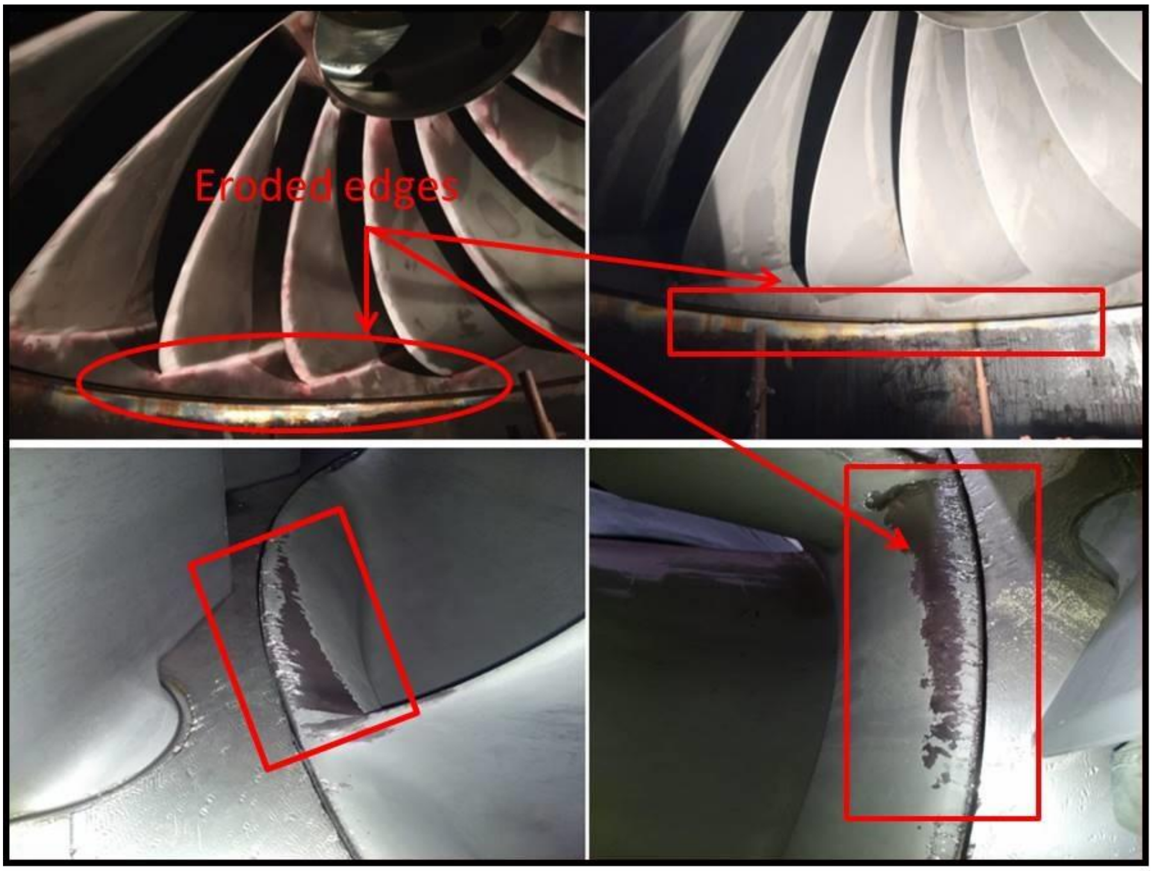

Figure 1.4. Silt erosion in a hydro turbine at Baglihar Hydroelectric Power Plant, Jammu and Kashmir, India (Case of present study

1.2 WEAR MECHANISMS DUE TO EROSION

As previously discussed, the most probable reasons for failure for an impulse turbine are erosion and cavitation, while the most likely causes of failure for a response turbine are erosion and abrasion (Kjolle, 2014; Neopane et al., 2019; Padhy and Saini, 2009). A surface may corrode when it suffers slow and steady erosion as a result of an electrochemical process. 'Pitting action' and 'crater formation' are the two fundamental processes that take place during corrosion (Rajahram et al., 2009). The primary and secondary forms of abrasion, chip formation, separation, crack development, and fracture, respectively, are shown in **Figure 1.5**. Cavitation erosion is a kind of erosion that is caused by bubbles in the slurry. In cavitation erosion, elements such as a material's hardness, surface roughness, and surface defects are all essential contributors. Nevertheless, the process of erosion is a convoluted one that has not been completely explored.

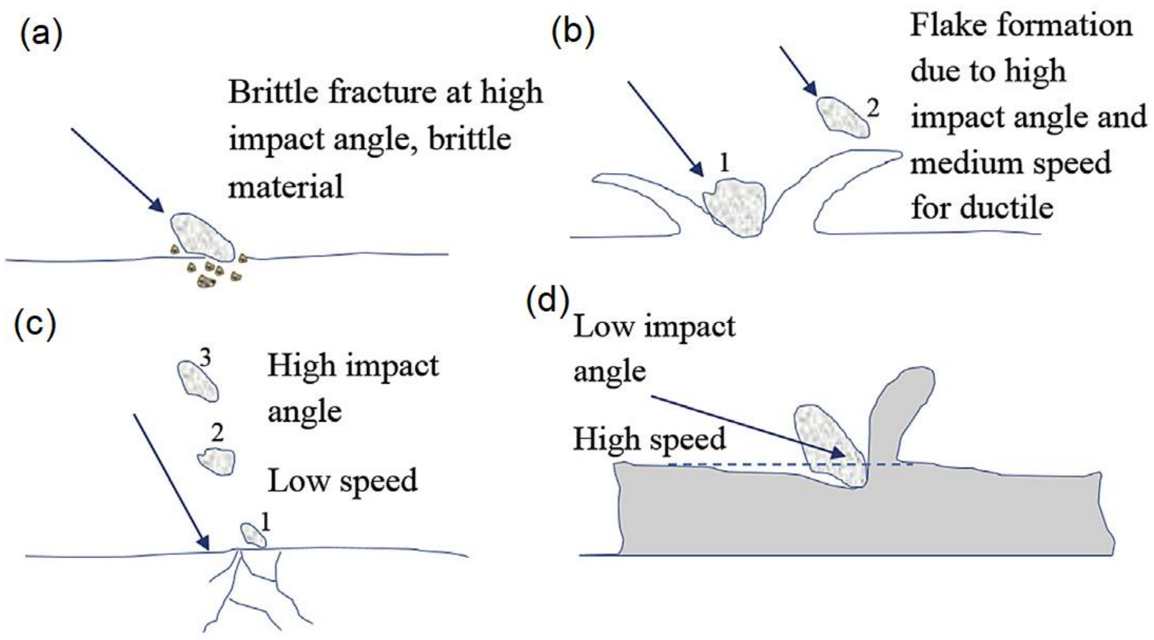

Figure 1.5. Various mechanisms of erosion wear: (a) brittle fracturing, (b) deformation, (c) fatigue, and (d) cutting erosion (Chitrakar et al., 2016).

The complexity of the erosion process is caused by several elements, including the composition of the particles, the quality of the material that is being eroded, and the parameters of the procedure. According to Finne (1960), the process of breakdown is determined by how the material behaved early on in terms of its hardness. Damage caused by erosion is more prevalent in ductile materials owing to the plastic deformation that occurs during erosion, while damage caused by erosion is more common in brittle materials due to the cutting action that occurs during erosion. According to the findings of Levy (1996) the rate of erosion in ductile materials was higher at the beginning of the operation and get reduced as the process went on. Bellman and Levy (1981) have described the silt erosion processes that are present using macro-particles. The processes that were classified as shallow craters and platelets were identified as being induced by the impact of macroscopic particles. Many different types of erosion processes may take place in ductile materials (Pintaude et al. 2003, 2009, 2019; Wang and Yang, 2008). Some examples of these processes include deformation, micro-plowing, micro-cracking, lip-formation, platelets, and small craters. They also hypothesized that the surface of the device would gradually deteriorate owing to the rapid impingement of particles, which was triggered by the first collapse of the delicate components. This theory was based on the fact that the delicate components would fail first. **Figure 1.6** illustrates the erosion of both ductile and fragile materials over time. When dealing with ductile and fragile materials, it is possible to disentangle the erosion process from the primary mechanism of wear. The initial phase in the erosion of ductile materials is material deformation, which ultimately results in the creation of groves with lips. On the other hand, the first step in the erosion of brittle materials is the commencement of cracks, which ultimately results in the development of fragmented material in the form of chips. According to Finne (1960), the crater will get larger if the particles that hit the object did so at a low angle of impact. However, shooting takes place when particles reach the target at acute angles, and the particles themselves are destroyed when they make forceful interactions with the substance.

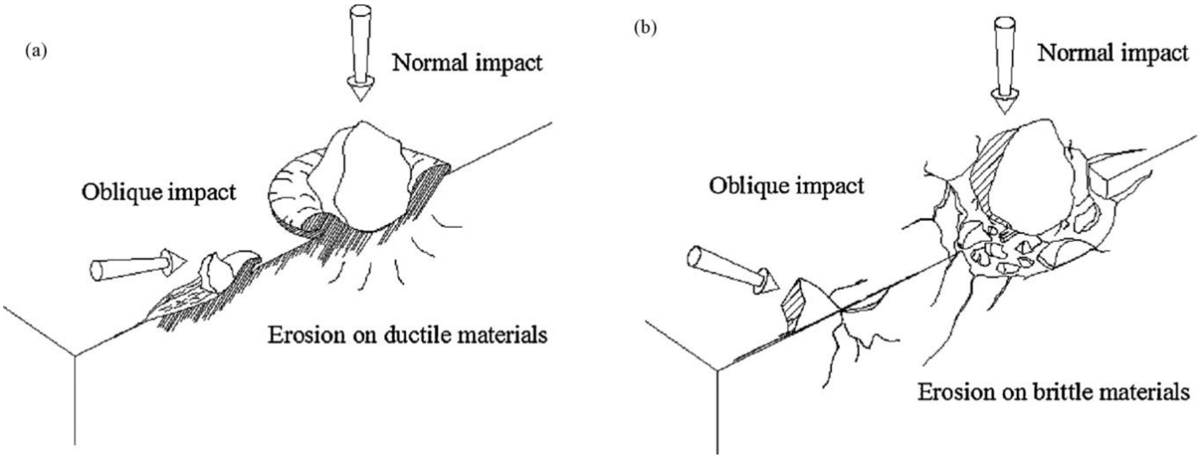

Figure 1.6. Schematic diagram of erosion in (a) ductile and (b) fragile materials (Wang and Yang, 2008).

It should be remembered that the above erosion processes are not absolute and may be combined at the same time. To overcome this tragedy, Sundararajan et al. (1990) proposed a correlation to evaluate the erosion efficiency (η) of material, as shown below:

$$\eta = \frac{2VH}{M_P V_P^2} \tag{1.1}$$

Where V = volume of removed material (m^3), H = hardness of the material (Hv), M_P = mass of the particle (kg), and V_P = velocity of the particle (m/s). They pointed out $\eta > 1$ represents the mechanism of fragility, i.e., brittle mechanism, while $\eta < 1$ is a mechanism of plastic erosion deformation, i.e., ductile mechanism.

The deformation (E_D) and cutting (E_C) mechanisms of silt erosion were defined by Clark and Wong (1995) as written below:

$$Er = \begin{cases} EC + ED \\ \dfrac{\frac{1}{2} M_p \left(V^2{}_N\right)}{\varepsilon} + \dfrac{\frac{1}{2} M_p \left(V^2{}_N \sin 2\alpha\right)}{\varphi} \end{cases} \tag{1.2}$$

Where the tangential and normal components of the velocity of the particle were denoted by V_T and V_N, respectively. Symbols α, ε, and φ are the impingement angle, empirical constant of specific energy required for deformation erosion, and constant of kinetic energy required for cutting erosion, respectively.

Grewal et al. (2013) proposed a method for determining the amount of energy required and consumed for the removal of material under the oblique and normal impact, which is as follows:

$$\xi = \frac{2V\sigma_{cr}\left(\dfrac{H_T}{K_T}\right)}{M_P V_P^2} \tag{1.3}$$

Where K_T stands for the material's toughness (measured in MPa), ξ denotes Erosion mechanism identifier and σ_{cr} stands for the material's critical stress (measured in MPa). When it comes to ductile materials, σ_{cr} is equivalent to the ultimate shear stress, but when it comes to brittle metals and alloys, it is equivalent to the ultimate tensile strength. Ploughing occurs when the value reaches near to 1, micro-cutting occurs when equal to 1, and brittleness occurs when the number 1 is exceeded.

1.3 DEPENDENCY OF WEAR IN HYDRO-TURBINES

Figure 1.7 shows the myriad of factors that contribute to the deterioration of silt. The properties of the silt, the medium, the target material, and the operating settings of the turbine all have a significant role in determining the amount of silt that is eroded. Hydro-abrasive erosive wear is dependent upon many parameters such as hardness, concentration, particle size, shape, and velocity of solid particles. These particles collide at a high enough velocity and produce severe surface damage to hydropower machine elements, which can be mitigated by managing the aforementioned parameters or, more importantly, the impact efficacy of the particles (Mann, 1999).

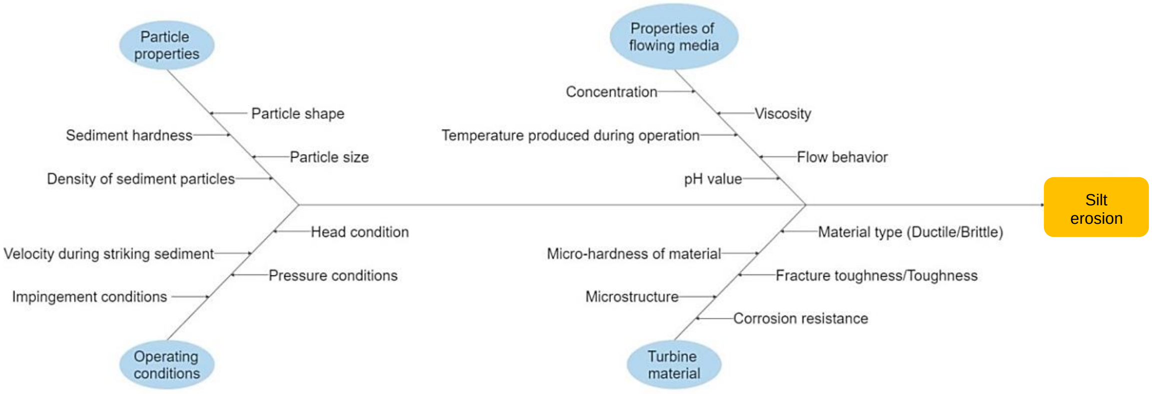

Figure 1.7. Cause-and-Effect diagram for silt erosion.

1.3.1 Particle Shape

The wide range of forms, sizes, and densities that silt particles shows significant impact on erosion. Spherical particles are said to result in much-reduced wear compared to their angular counterparts, as stated by Levy and Chik (1983). Bahadur and Badruddin (1990) conducted research to determine the effect that high-velocity erosion of solid particles (SiC, Al_2O_3, and Quartz) had on the particle grain size and form of the particles. Experiments were carried out using a jet tester employing particles with a velocity ranging from 40 to 65 meters per second and sizes ranging from 10 to 500 microns. The values of the circularity factor (*CF*) of the particles were discovered to range between 0.70 and 0.97. An expression of the correlation that Zou and Yu (1996) gave to identify whether or not particles have a spherical shape has been provided below:

$$\psi = \frac{A_s}{A_p} \tag{1.4}$$

Where ψ is ratio of depth of contact to depth of cut, A_p is area of particle (m^2), and A_s is area of sphere.

Hentschel and Page (2003) found evidence of yet another shape factor (SF), which they referred as the roundness factor.

$$RD = \frac{4 \times A_p}{\pi \times D^2{}_{maxfret}} \tag{1.5}$$

Where A_p is area of particle (m^2) and $D_{maxfret}$ is maximum feret diameter.

A revised version of the correlation established by Riley (1941) has been published by Bouwman et al. (2004), and it may be used to calculate the shape factor (SF) value.

$$SF = \frac{4\pi A}{P^2} \tag{1.6}$$

Where A is area (m^2) and P is perimeter (µm).

To investigate the particle shape of fault rocks, Heilbronner and Keulen (2006) made use of the Paris factor in the following manner:

$$PF = 2\left(\frac{P_p - P_{ch}}{P_{ch_A}}\right) \tag{1.7}$$

Where P_p is perimeter of particle, and P_{ch} is perimeter of convex hull of particle.

Desale et al. (2006) studied the effect of SF value on the silt erosion of ductile materials. After making the following modifications to the Riley (1941) correlation, they proposed using it to calculate the SF value:

$$SF = (SF_{Avg}\, SF_{Max}\, SF_{Min})^{1/3} \tag{1.8}$$

Where *SF* is shape factor. The subscripts *Avg* is average, *Max* is maximum and *Min* is minimum.

Woldman et al. (2012) carried out a study on the effects of dry wear on rubber combined with sand, and their findings indicated that the shape factor for sand fell somewhere in the range of 0.5-0.65. During an experiment involving erosion and wear using white cast iron, Walker and Hambe (2015) analysed photographs of particles to identify the morphologies of the particles. Silt erosion investigations were carried out by them with the assistance of a Coriolis tester, and the results revealed the following correlation:

$$E = K \times CF^{a} \tag{1.9}$$

Where *E* is erosion wear, *K* is constant, *CF* is circulatory factor and superscript '*a*' is exponent.

It was noticed that the amount of silt erosion induced by solid particles increased as the CF value of the sand decreased (the average was 0.73). According to the findings of the study, the structure of the particles plays an important part in the process of erosion and wear. Plastic deformations and micro-cutting action were produced as a result of the spherical shape of the fly ash particles as well as the nature of their rebounding contact with the target surface of the work piece. Irregularly formed, blocky particles are responsible for creating craters that have jagged surfaces but smooth interiors (Walker and Hambe, 2015). The process known as "chipping" of eroding particles happens when particles with an angular form cause fractures and craters (Desale et al., 2006).

1.3.2 Particle Size

The slurry erosion as a function of particle size effects on AISI 5117 steel has been studied by authors and reported that the erosion rate elevates with an increase in particle size of the erodent (Al-Bukhaiti et al., 2016). There is a link between particle size and erosion rate that follows a power law (Gandhi et al., 2003). Elkholy (1983) developed a link for erosion by making use of the solid-liquid velocity (*V*), the particle diameter (*d*), and the particle concentration (*C*). This connection is provided by the equation:

$$E_w = k \times V^m \times d^n \times C^p \tag{1.10}$$

The above equation displays the exponents of speed (represented by '*m*'), particle size (represented by '*n*'), and concentration (represented by '*p*'). The range of values that are considered to be normal for the exponent particle diameter (*n*) is 0.3–2.0.

When it reaches its destination, a bigger particle will damage a greater area than a smaller particle would. Increased potential energy is carried by larger particles while they are in motion, which results in increased surface wear. The number of particles with a size greater than 1000 µm has led to an erosion ratio that has remained the same (Tilly, 1973). The silts that are often found in river water have an uneven shape and range in size from very small to very large. The size fraction set or the particle size distribution (PSD) may be used to calculate the particle size once it has been known how large the particles are. Using any international standard of sieves, such as those developed by ASTM, BSS, or IS, it is possible to calculate the distributions of particle sizes in fractions. The following equation allows us to calculate the arithmetic mean diameter i.e. d_p (Gupta et al., 1995), which is as follows:

$$d_p = \sum_{i=1}^{n} fi \times (\mathrm{N}_i) \tag{1.11}$$

Where 'N_i' is the B.S.S. number of the particle size range and '*fi*' is the solid percentage. The 'N_i' is the B.S.S. number of the particle size range. The lower the particle size fraction, the less severe the erosion induced by these slurries, while the bigger the particle size fraction, the more severe the erosion (Gupta et al., 1995). Both the phenomena that occur during particle-particle interactions and those that occur during particle-target interactions are subject to change as a direct function of the size fractions (Tilly, 1973).

1.3.3 Silt Hardness

Silt has a Vickers micro hardness number that ranges from 900 to 1000Hv. According to Verma (1999), the micro hardness value of silt may reach up to 5 Mohs, which is sufficient to cause the components of the turbine to deteriorate. A limited group of researchers has created correlations between particle hardness and goal hardness. These correlations, which may be used to predict erosion rates, have been used by researchers. Wiederhorn and Hockey (1983) established the following erosion-related statistical connection between fracture toughness (k_T), specific radius (r_P), particle density (ρ_P), and particulate strength (H_P):

$$E_T = k \times V_P^{2.8} \times r_P^{3.9} \times k_T^{-18} \times H_P^{0.48} \times \rho_P^{1.4} \tag{1.12}$$

The following empirical link was established by Wada and Watanabe (1987) via the use of the hardness factor:

$$E \prec \left(\frac{H_T}{H_P} \right)^k \tag{1.13}$$

In the preceding equation, the letter '*k*' served as a symbol for the exponent that was associated with the hardness ratio. The hardness ratio may be calculated by taking the particle hardness (H_P) and dividing it by the material hardness (H_T). Elkholy (1983) employed four different materials, each of which had a Brinell hardness (HB) rating that ranged from 150 to 400. They were able to perform wear experiments and evaluate the weight loss of materials by varying the silica sand particle size while keeping the other parameters constant. This allowed them to determine how much material was lost. The hardness of silica sand was stated to be 710 Hertzian Brinell (HB). They gave the following information on the transition point for the hardness ratio (H_T/H_P):

$$\frac{H_T}{H_P} = 1.9 \tag{1.14}$$

The exponent '*k*' is fluctuating as a result of the previously indicated change in either the ratio of hardness's growing or lowering value. Levy and Chik (1983) investigated the relationship between the abrasiveness of the particles in an atmosphere and the rate at which carbon steel

(AISI 1020) was eroded. After raising the particle hardness to 700 kgf/mm^2, there was no further increase in the amount of silt erosion caused by the AISI 1020.

1.3.4 Density of Particles

The surface density of materials is another factor that determines the degree to which they degrade. By keeping some parameters constant, increasing the density of the material suggests a larger concentration of solid particles, which in turn influences the target and leads to improved erosion performance. This is the case even if you retain certain factors constant. Research on erosion was carried out by Stack and Pungwiwat (1999) utilizing SiC and Al_2O_3 as component materials. According to the results of the experiments, the presence of Al_2O_3, which has a higher density than SiC particles, has led the target to lose even more mass. Desale et al. (2006) discovered something almost similar to the original. When traveling at higher speeds, mass density emerges as the most important determining factor. The bulk density of the silt has a direct role in determining the amount of energy that is imparted by the impact. Particles with a larger mass density have a higher probability of possessing a high kinetic energy velocity. When these particles collide with their objective, they release their enormous potential energy, which further deteriorates the material.

1.3.5 Silt Concentration

The silt content in the majority of Himalayan rivers is very high, averaging 10 g/l, which is equivalent to 10,000 ppm. During the monsoon season, it may reach exceptional quantities (up to 20,000 ppm), depending on the location (Awal et al., 2019). The amount of silt that is suspended in water is a significant component that plays a role in erosion as a natural process. In hydroelectric plants, silt is a by-product that may be found in heterogeneous slurry at any concentration between zero and one hundred percentage by volume. The rate of material deterioration increases in proportion to the concentration of slurry that is present (Desale et al., 2011; Gupta et al., 1995; Prasad et al., 2004; Singh, 2019a). There is a range of between 0.9 and 1.3 for the value of the concentration exponent i.e. p (Grewal et al., 2013). Dasgupta et al. (1998) conducted research on the silt erosion that occurs on steel samples as a result of multisized sand slurry. According to the findings of the researchers, the rate of erosion was decreased by 30% to 50% with the increase in solid content. On the other hand, as seen in **Figure 1.8**, the rate of erosion slows down at low concentrations as the concentration of solids in the environment is increased (Grewal et al., 2013). This phenomenon may be traced back to the fact that the re-emerging particles have a shielding effect (Chandel et al., 2012;

Hawthorne, 2002). It was noted that the earliest phases often have high concentrations, which raise the erosion rate to an unacceptable degree. Interactions between particles, such as collisions and rebounds, are very important. When solid concentrations reach one weight percentage, the interactions between the particles, known as striking and bounding, result in a loss of momentum and a shift in the direction in which the particles are moving. Because the interaction with particulate matter lowers the amount of contact that exists between the particle and the target, the rate of erosion that occurs as a consequence of this interaction is enhanced. Important materials may be found close to the point of rebound. This impact is only valid for values of the variables that fall inside a particular range.

Given what has been discussed, it stands to reason that the slurry concentration influences some additional factors that have not received sufficient attention so far. Erosion is reduced in proportion to the concentration rate. There are contradictory claims among investigators (Kleis and Kulu, 2008; Singh, 2019b; Singh et al., 2017) on whether erosion slows down with increasing slurry concentration. Particle interactions with their targets and with other particles are all said to be affected by the concentration (Chandel et al., 2012; Dasgupta et al., 1998; Grewal et al., 2013; Hawthorne, 2002; Kleis and Kulu, 2008; Singh, 2019b; Turenne et al., 1990). Finally, it may be said that additional research is needed to know the hidden aspects and requires constant attention.

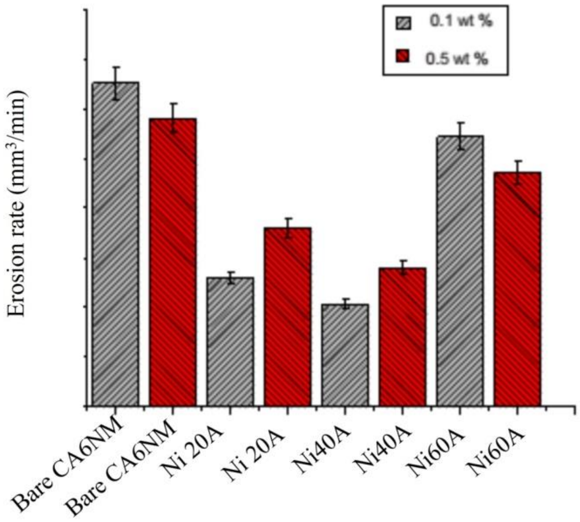

Figure 1.8. Erosion rate versus solid concentration (Grewal et al., 2013).

1.3.6 pH Value

The pH of the slurry may be adjusted to reduce or prevent erosion and corrosion. When determining the pace at which materials are being eroded, the pH level of the slurry may prove to be an essential aspect. According to Singh (2019b), the pH of silt slurry from the

Naptha Jhakhri Dam in H.P., India, ranges from 7.71 to 1.16 when the concentration is in the range of 30-60 wt.%. The erosion and corrosion of AISI 4330 steel in a saline and sand slurry was investigated by Peña Ballesteros et al. (2016). In the instance of pH-3 saline-sand, the volume loss caused to AISI 4330 was found to be larger than the volume loss caused by pH-7 saline-sand. Karafyllias et al. (2019) discovered that there was a link between total volume loss (TVL) from materials and the following factor:

$$TVL = M + C + S \tag{1.15}$$

The volume loss that occurs as a result of mechanical failure, simple electrochemical decay, and the synergistic effects of erosion and corrosion, respectively, are represented by the M, C, and S symbols in the equation that was just discussed.

1.3.7 Flow Behaviour

The rate at which slurry moves through a fluid is determined by several elements, including the viscosity of the fluid, the size and shape of the particles, and the concentration of the slurry. Rheology is the study of fluids and their relationships with the solids they come into contact with. The rheological quality of slurries may be affected by a variety of characteristics, such as their form, size, density, and mass fraction (Singh et al., 2017). When determining flow characteristics, it has been established that concentration is a crucial factor in many different situations. A shift in concentration has the effect of altering the dimensionless numbers known as Reynolds (Re) and Stokes (St). The drop in the viscosity of the slurry occurs as the concentration of Re in the slurry goes from high to low. This information was discovered by (Bong et al., 2015), as seen in **Figure 1.9**.

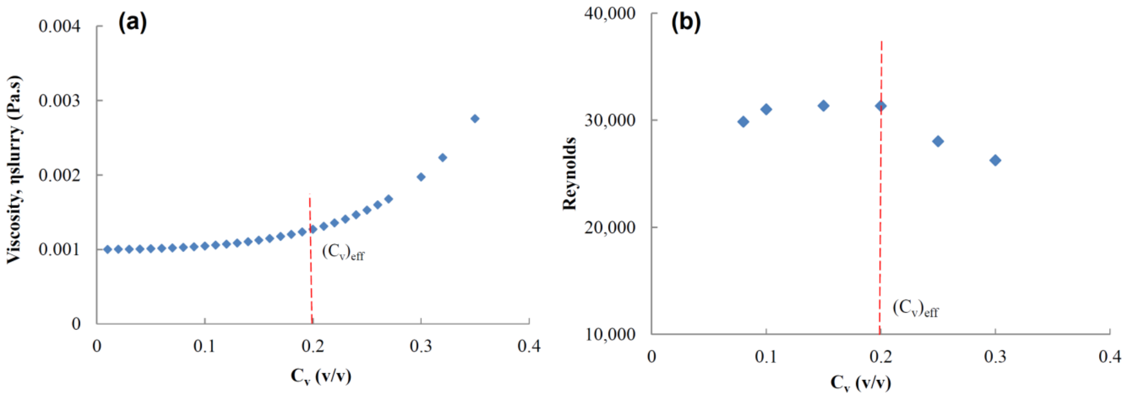

Figure 1.9. Effect of solid concentration on (a) viscosity and (b) Reynolds number (Bong et al., 2015).

Flows are understood to be laminar when their Reynolds numbers (*Re*) are less than 2100, transient when their *Re* values are between 2130 and 4000, and turbulent when their Re numbers are more than 4000. Shehadeh et al. (2014) used sand-water slurry with concentrations ranging from 3-9 g/l to determine the resistance of carbon steel to erosion and corrosion. As can be seen in **Figure 1.10**, the rates of erosion and corrosion, as well as the Re values, both have a role in increasing the detrimental consequences of the processes. Particles are regularly influenced by the fluctuations in concentration that occur in the real world. It's possible that the Stokes number, or *St*, might provide some insight into this occurrence. The researchers Dabirian et al. (2016) discovered that when the particle size and solid concentration escalate, so did *St.* On the other hand, Bartosik (2010) looked at the significant impact that a high particle concentration and large particles have on the shear stress that exists between the particles and the target wall.

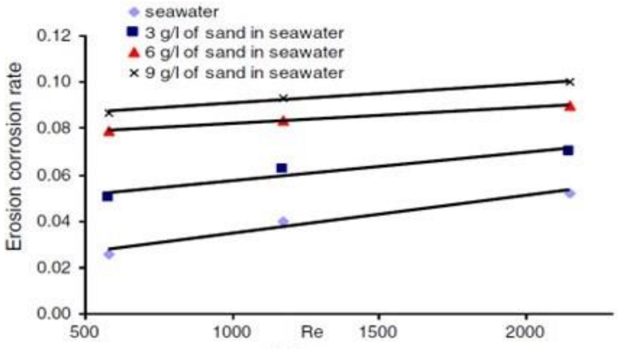

(a) Laminar flow

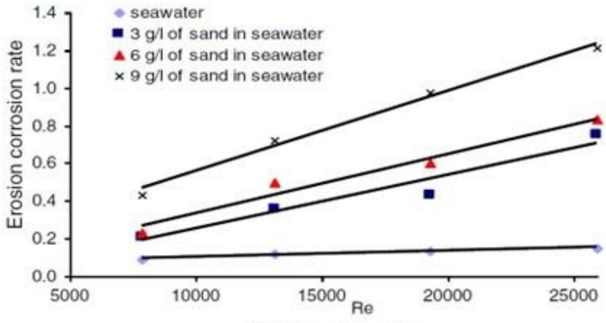

(b) Turbulent flow

Figure 1.10. Corrosion and erosion rates (mg/m^{2}min) versus Reynolds number (Shehadeh et al., 2014).

1.3.8 Effect of particle velocity

Numerous researchers have done considerable research on the effect of particle velocity on the erosion rate using different steels and found erosion rate increases with an increase in slurry velocity (Alam et al., 2016). Since the kinetic energy of an impacting particle is related to its mass, a minute particle that is traveling at a slow speed will only produce a little distortion of the surface of the target. Even if just a very small portion of the erodent material is moving, its total kinetic energy is enough to cause the target surface to undergo irreversible deformation. When the number of particles exceeds, a high threshold energy with the rise in velocity occurs (Desale et al., 2008; Islam et al., 2015; Rajahram et al., 2009). This results in an increase in the rate at which the surface deforms. The change in mass with change in time is also termed as erosion, as written below:

$$-\frac{dm}{dt} = kv^n \tag{1.16}$$

Where symbol *t* represents the amount of time that was spent during experimenting, *m* represents the mass that was lost from the surface of the target, *k* stands for the experimental constant, and *n* represents the velocity exponent. Depending on the chemical, the value of *n* might vary anywhere from 2 to 5 (Sharma et al., 2015).

1.3.9 Impingement Conditions

Islam and Farhat (2014) identified the following as the primary erosion mechanisms for API X42 steel by their findings on the impact angle and particle size:

- When particles collide with a surface at a shallow angle of attack, they push the metal ahead and, as they descend, generate ridges on the edges of the surface as they go along. Therefore, the process of "ploughing," which occurs under these conditions, is the primary mechanism for erosion. This is separate from the "cutting" process, which occurs elsewhere. During the ploughing process, the material does not separate from the surface, and instead, 'lips' form along the erosion groove. At higher speeds, however, the mechanism responsible for cutting takes the lead. As a consequence of ridge fracture, the material is shaved away from the surface during the cutting process, resulting in the production of dust and debris.
- Plastic deformation and flattening are two of the several types of wear that may occur at low speeds. The repeated impact of the particles induces plastic deformation and the elimination of weak lips as a result of the action. When particles are subjected to higher velocities and impact angles, primary metal cutting is followed by secondary metal cutting. If the eroding particle collides with the particles that are implanted in the material

and are then redirected through the substance, the surface that it is going for will be harmed. Because of this, just a very tiny portion of the material (about two to three micron meters in diameter) has been compromised.

1.3.10 Material Type

Since the start of the 20th century, the industry of materials has seen phenomenal growth. Materials that are easily available and can withstand tensile force, compressive force, impact loading, fatigue loading, and other types of loading are abundant. Researchers and designers have put in a significant amount of time to develop the construction of the materials so that they can withstand these qualities. Surface failure processes are affected by a material's micro hardness, toughness, elasticity, elongation, and ductility, among other properties, in addition to the phase microstructure of the material. The past literature adds to the body of knowledge that the use of stainless steel is extensively accepted for hydroelectric power plants because of its resistance to solid particle erosion and good corrosion properties (Agarwal et al., 2014; Brunetti et al. 2014; Hutchings and Shipway, 2017; Kishor et al., 2018, 2016, 2014). Even though proper steel has been selected for hydro turbine parts the material still gets damaged in due course of time due to solid particles action in the form of silt. **Table 1.2** outlines the various features of turbine steels. High-chromium steels are often used in the fabrication of turbine components. The term "high-chromium steels" refers to the austenitic steel 18Cr8Ni, the martensitic steel 13Cr1Ni, and the martensitic-austenitic steels 13Cr4Ni or 16Cr5Ni. These three types of steel are all martensitic. Steels with the compositions 13Cr4Ni and 16Cr5Ni are used in the production of the great majority of today's turbines (Jain, 1999). The Swedish-grade steel 13Cr6Ni was developed in the late 1960s; nevertheless, the restriction of its utilization due to patent rights led to the production of 13Cr4Ni, 16Cr5Ni, and 17Cr4Ni stainless steels. Of these stainless steels, 13Cr4Ni and 16Cr5Ni are widely employed in the turbine industry. There is a lack of fatigue and creep resistance in austenitic steel 18Cr8Ni with less than 0.2% Mo (Jain, 1999), even though this steel has good corrosion and cavitation resistance. This kind of steel was also used in the manufacturing of the turbine runners of the hydroelectric facilities located in Pathri, Uttar Pradesh, and Mattur, Tamil Nadu, India (Goel and Sharma, 1996). Even though martensitic steel 13Cr1Ni was developed as a substitute for 18Cr8Ni, it has poor resistance to corrosion, cavitation, and sand erosion due to its low hardness, low toughness, and low Ni concentration. According to the findings of Thapa and Brekke (2004), the erosion resistance of 13Cr4Ni and duplex steel is greater than that of 16Cr5Ni turbine steel.

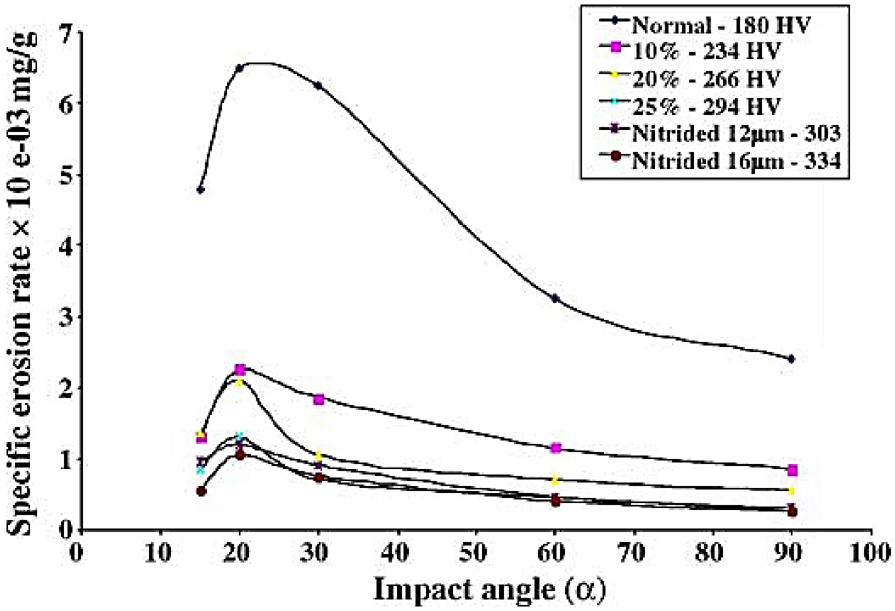

Figure 1.11. Erosion rate of different materials at room temperature (V = 32 m/s, dp = 102 µm) (Divakar et al., 2005).

The erosion rate is swayed by the substrate material hardness and the particles impinging on the material surface and the examination revealed that an increase in the hardness of the material provides higher erosion resistance (Divakar et al., 2005; Singh, 2019a; Singh et al., 2019a, 2018b, 2018c, 2018a; Singh and Singh, 2021a). The results of measurements performed on the micro hardness of various materials are shown in **Table 1.2**. Several studies have highlighted the significance of the ratio of the target hardness to the particle hardness (Bellman and Levy, 1981; Evans et al., 1978; Reddy and Sundrarajan, 1986). Oka et al. (2005) developed a model to forecast the total silt erosion for a range of material hardness (GPa, H_T) and other method factors, such as impact velocity (m/s, V_P) and particle diameter (m, d_P):

$$E_T = k \times V_P^m \times d_P^n \times H_T^{K_1} \times \sin\alpha^{n_1} (1 + \mathrm{H}_T (1 - \sin\alpha))^n 2 \tag{1.17}$$

Where m represents a velocity exponent and n represents a particle size exponent. The angle of impact between the particle and the target determines the values of the variables n_1 and n_2, whereas k and K_1 stand for the experimental constant and the exponent of material hardness, respectively.

According to the findings of Levy and Hickey (2010), materials with a higher hardness were subjected to a larger amount of wear than those with a lower hardness. On the other hand, plastic deformation is brought about by the ductility of the material owing to the transfer of kinetic energy of particles, which results in less surface degradation. This phenomenon is caused by less surface degradation. As can be shown in **Figure 1.11**, Divakar et al. (2005) observed the erosion of cold-rolled and case surface-hardened SS 316L stainless steel.

Table 1.2: Materials and Properties of Turbine Steels (Jain, 1999).

S. No.	Material	Tensile Strength (MPa)	Yield Strength (MPa)	Elongation (%)	Impact Strength (*J*)	Microstructure/ Type
1	13Cr1Ni (0.06C 0.4Mo)	630	470	18	39	Martensite, Hard and brittle
2	13Cr6Ni (0.06C 0.4Mo)	800	550	16	70	Martensite (70%) Austenite (30%)
3	17Cr4Ni (0.06C)	880	650	12	59	Martensite+ Austenite+ Ferrite, Hard and ductile
4	13Cr4Ni (0.04C 0.4Mo)	823	686	23	81	Martensite, Hard
5	16Cr5Ni (0.05C 1.5Mo)	880	600	21	100	Martensite (65%) Austenite (35%), Hard and ductile

1.4 SILT EROSION REMEDIES

Surface engineering is a flexible method used in many different fields. Mechanical loads and fatigues, wet environments, tribological reactions, biological activities, and so on are just some of the situations where a surface's characteristics might be altered to improve its performance (Datta and Gray, 1993). This field encompasses a wide range of methods that can be used to make these modifications. The numerous methods of surface modification are organized and labelled in **Figure 1.12**. Coating deposition techniques are the surface modification method of choice across all industries and economic sectors, safeguarding equipment components and increasing their usable life. Multiple layers of coating powders are applied over the surface of another material, called a substrate.

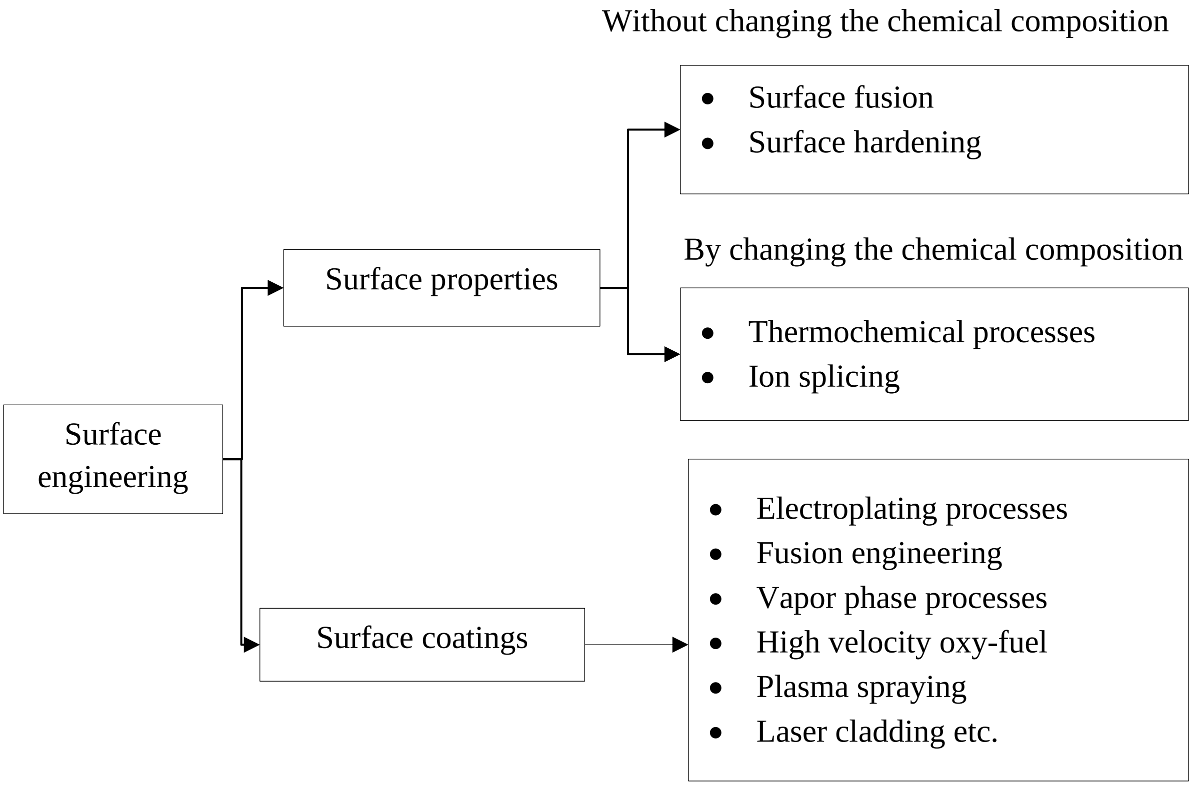

Figure 1.12. Various surface modification processes (Singh et al., 2023).

The pace at which silt erosion occurs may be decreased by modifying material surfaces, but it cannot be eliminated. In the absence of human intervention, most metals soon rust. A discussion on how to reduce silt erosion in hydro turbine materials is done in **Chapter 2**. There are several ways to lessen the effects of erosion and wear, such as via improved component design, material choice, environmental management, coating application, and so on. Erosion causes wear, although it may be mitigated with frequent monitoring and maintenance. The silt erosion reduction model is shown in **Figure 1.13**.

1.4.1 Design

The most effective design for a component serves to lessen the amount of erosion and wear on the surface. Some of the design aspects that assist decrease silt erosion are inadequate drainage, shape bends, irregularities in surface, surface finish, and maintenance design, etc. During the design process, some of the environmental factors that are taken into account include velocity, concentration, pH, and dissolved components.

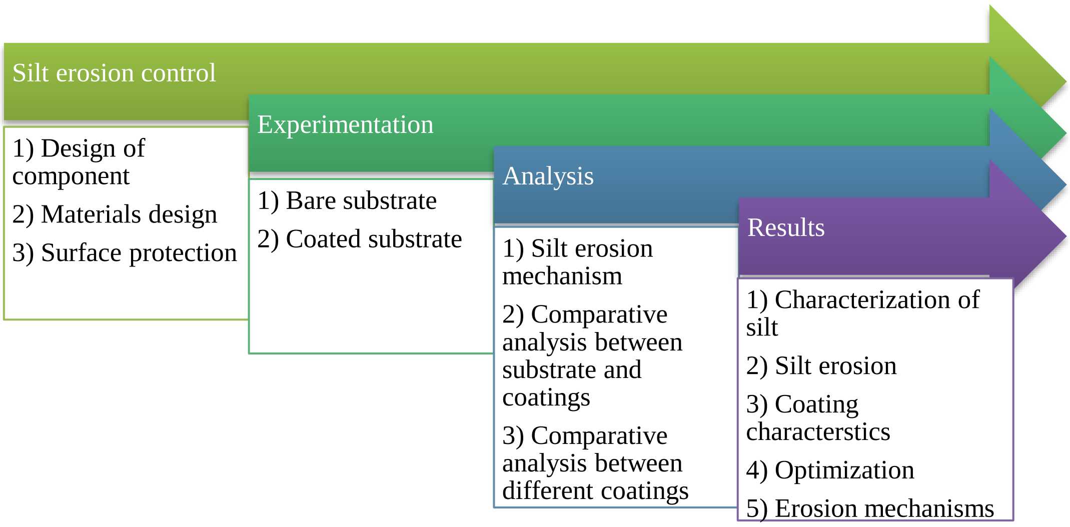

Figure 1.13. Erosion and wear monitoring process flow diagram.

1.4.2 Materials design

The choice of materials is quite important if there is a requirement to reduce the impacts of erosion and wear on a surface. Erosion and wear are both affected by a variety of material properties, including micro hardness, toughness, elasticity, and ductility. These values are insufficient since the material component in question is going to be vulnerable to particle contamination and mechanical loadings. As a result, the other characteristics of the material should not be overlooked either. The selection of material is made more difficult by several aspects, including aesthetics, the ease of manufacturing, availability, and the mechanical properties of the material.

1.4.3 Surface protection

To reduce the amount of erosion and wear that occurs, several kinds of coatings have been applied (this topic is covered in **Chapter 2**). There are various coating technologies available which can be used to deposit suitable material on the substrate. They are generally illustrious by coating thickness: deposition of thick films (20-400 µm) and deposition of thin films (below 10-20 µm). The coatings may be broken down into one of three groups, which are as follows:

- Metallic coatings may be created using a variety of processes, including electrodeposition, hot dipping, cladding, diffusion, laser alloying, and thermal spraying.
- Inorganic coatings include anodizing, phosphating, thermal competing, and spraying.
- Typical organic coatings include paints, epoxy, bitumen, rubber, and plastic lining.

1.5 THERMAL SPRAY COATING

Thermal spray coating technique can be used to deposit variety of coating powders such as metallic, ceramic and oxides with varying thickness of 50 to 500 µm. In this method, a spray of molten particles is focused on a region to create the coating in the deposition technique known as thermal spraying. This technique can be used to improve the qualities of designed surfaces by shielding the components from corrosion, wear, and high temperatures. Processes for thermal spray coating are frequently used to repair damaged and worn parts. Thermal spraying might occasionally be helpful for decoration, enhancing the aesthetic qualities of parts. The substance used for coatings can be in the form of powder, wire, rod, or molten metal. The process's operations can be carried out manually, mechanically, or automatically. Thermal spraying was mentioned for the first time in the patents of the Swiss engineer Max Ulrich Schoop (1870-1956) at the beginning of the 20th century (Davis, 2004). The various advantages offered by thermal spray coatings are low porosity, excellent coating, good adherence to substrate, low permeability, excellent corrosion or wear resistance, reliability, long-lasting protection, improved electrical properties (resistance and conductivity), clearance and good dimensional control (Fauchais and Vardelle, 2012). The same basic idea underlies all thermal spraying techniques to heat a feed stock (such as powder or wire), accelerate it to an extremely high velocity, and then allow the resulting particle collisions to occur on the substrate. The particles will deform and freeze onto the substrate. A coating layer will develop when millions of particles are stacked on top of one another. The primary mechanism for the bonding between the particles and substrate is mechanical or metallurgical bonding (Talib et al., 2003).

There are various steps in thermal spraying technique, as illustrated in **Figure 1.14**. Surface activation is the first step of any thermal spraying process. This includes cleaning and grit blasting of surface to be coated. Masking methods are generally adopted for components that require only definite area of coatings. In the second step, the material is melted. The feed stock material is introduced in the hot gas stream. The hot gas stream is either produced by physical reaction (Plasma) or by chemical reaction (combustion). In the third step, the particles are accelerated to the substrate by hot gas and particles deform to form the coating. Finally, the coatings are examined and evaluated for excellence either by microstructural or mechanical evaluation (Šimuvonic, 2010).

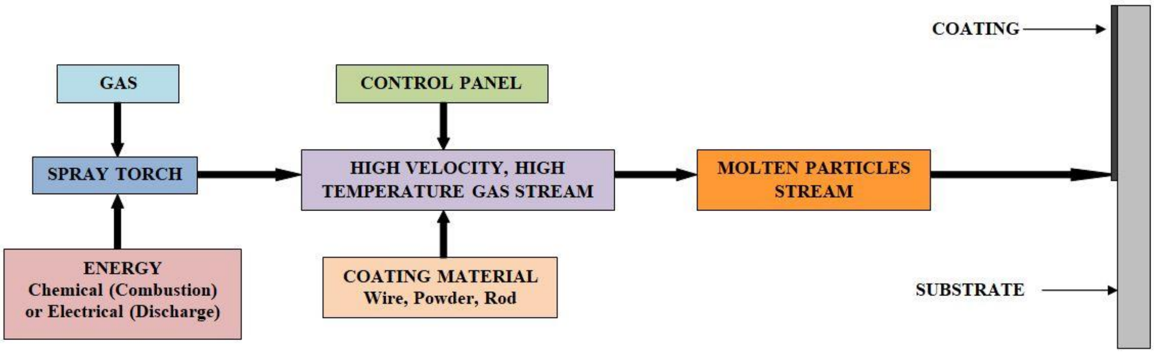

Figure 1.14. Schematic diagram of thermal spraying technique.

The family of Thermal Spray processes are generally grouped into four major categories i.e., flame spray, electric arc spray, plasma arc spray and kinetic spray (cold spray) with many subsets falling in each category. Selection of suitable thermal spray process is determined by desired coating material, economics, coating requirement performance, part size and portability (Talib et al., 2003). **Figure 1.15** shows the classification of thermal spray coatings. All the processes have certain advantages and disadvantages. Plasma spraying is generally regarded as the most versatile of all the thermal spray processes, hence can be sued for wide variety of applications (Ranjan et al., 2023, 2019). A wide powder particle size range can be used, normally 5-100 µm as compared with HVOF spraying. Plasma spraying is a widely accepted and well-understood coating process. However, electrodes and other internal parts of the plasma spray gun quickly degrade. As a result, gun electrodes must be replaced frequently, and quality control is required to maintain coating consistency. When spraying in the air, high temperatures associated with the plasma jet can cause carbide breakdown or intense oxidation, resulting in carbide coatings with greater oxide levels or less metallic coatings than HVOF sprayed coatings. Similarly, electric arc process can be used to spray only electrically conductive materials that are accessible in an appropriate wire form. It cannot be used to spray ceramics or cermet. In comparison to coatings deposited by HVOF and plasma spraying, arc sprayed coatings typically have more additional porosity, more oxide, and lower bond strengths. It was observed that among all the four type of processes, HVOF technique is one of the versatile technologies which can deposit wide variety of coating of different thickness.

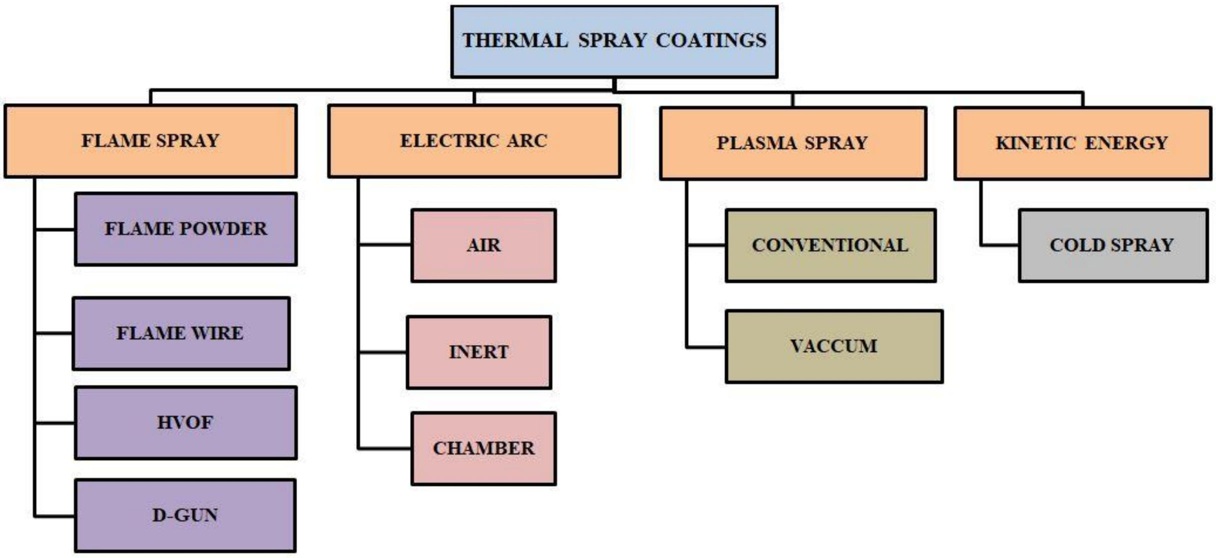

Figure 1.15. Classification of thermal spraying coatings.

1.6 HIGH-VELOCITY OXY-FUEL (HVOF) TECHNIQUE

The high velocity oxy-fuel technique is a high velocity process which was invented only 20 years ago. In an HVOF, a combustion jet is produced by combining fuel gas (such as propane, hydrogen, or propylene) and oxygen at a temperature of between 2500 and 3000°C. Burning occurs at extremely high pressure, exiting through a narrow barrel (typically 8 to 9 mm) to create a supersonic gas jet with high particle velocity (Yuan et al., 2023). Additionally, feedstock in the form of powder or wire can be dispersed at average rates of 2.3 to 14 kg/h (Li et al., 2002). Due to a higher impact velocity the method creates coatings that are incredibly dense and well bound. Smaller powder sizes and faster impact velocities result in smoother as-sprayed surfaces and lower it oxide content (Sobolev et al., 2004). HVOF sprayed coatings can have extremely complex microstructures that depend on a variety of processing factors. Powder used for deposition must have small size distributions and are restricted to a range of around 5 µm to 60 µm. Although, deposition of coatings is difficult to achieve on to internal surfaces of small cylindrical components, or other limited access surfaces, because HVOF spraying wants line of sight to the surface and a spray distance of 150-300 mm (Verdon et al., 1998). Its advantages of spraying variety of coatings with low porosity and high bond strength make it a versatile technology. Hence, in the present study, HVOF coating technique has been used to deposit the coatings on the substrates. As the foremost requirement of the sprayed coating in case of silt erosion is hardness, bond strength with low porosity. Otherwise there will be more chances of failure of coating in such a destructive environment.

1.7 MOTIVATION BEHIND THE PRESENT STUDY

An additional concern is the silt erosion that might occur as a result of the movement of different types of slurries. Erosion and wear are encouraged by accelerated conditions, which results in decreased equipment durability. The mining industry, the chemical industry, and the thermal power generating sector are the most common places where slurry erosion may be found. In a wide variety of industries, examples of equipment that has been worn out include runners, guide vanes, casings, impellers, nozzles, valve seats, tubes, tees, and flanges, etc. Both the impeller and its blades are exposed to conditions that provide the greatest risk due to their very high velocities. In actual conditions, the silt concentration remains <10% in upper Himalayan range (high altitude) hydropower plants. However, the concentration of silt becomes higher at the lower Himalayan range (lower altitude) hydropower plants. Sometimes, the silt concentration becomes higher as 30%. In these conditions, a high silt erosion wear that occurs.

The wear that occurs as a result of gas-solid erosion is also simpler to understand in comparison to the wear that occurs as a result of solid-liquid erosion. The jet-impingement test methodology is the standard approach, and it may be used to analyse the erosion that is caused by gas-solid flow. This technique was authorized by the ASTM Standard (ASTM-G76-95, 2000). However, Desale et al. (2006) advised utilizing a slurry pot tester to analyse erosion in pumps and pipes for the transfer of solid-liquid slurries. This was done to determine how well the pumps and pipelines were functioning. For design reasons, it is necessary to evaluate the abrasion and erosion that different pump materials are subject to. Researchers also uses slurry pot tester to know the combined effect of cavitation and slurry erosion as well for different materials (Agarwal et al., 2014; Amarendra et al., 2012; Rajat Gupta et al., 1995).

It may be possible to extend the pump or its components useful life by making adjustments to the design of the component, the material choice, or the surface quality. Based on the findings of the present study, the researchers determined that surface modification is the most efficient approach to improve the silt erosion performance of turbine materials. HVOF spraying provides the highest degree of flexibility when compared to other processes for the deposition of coatings. According to researchers (Jonda et al., 2023; Maruszczyk et al., 2017; Nayak et al., 2023, 2022; Nowakowska et al., 2022; Singh et al., 2019d; Szala et al., 2021, 2020, 2014; Szala and Łukasik, 2016), the HVOF process can be used successfully with both pure metals and ceramics/cermets. In the present experiment, ceramics were used which led to an improvement in both the silt erosion performance of hydro turbine materials. In this context, the HVOF approach is strongly suggested to be used in these kinds of situations.

1.8 THESIS OUTLINE

The chapters of the thesis are broken up into six sections, each covering a different aspect of the work presented here. Below is a synopsis of what each chapter covers:

- *Chapter 1* provides an overview of the many facets of silt erosion is summarized. Types of hydro turbines, processes of silt erosion, various hydro turbine materials, and strategies for reducing silt erosion for a variety of materials are discussed in this chapter.
- *Chapter 2* provides an overview of the literature on silt erosion of various coatings and hydro turbine materials. This chapter also includes references to the literature on various bench scale test rigs, thermal spraying procedures, and factors impacting silt erosion.
- *Chapter 3* explains the research methodology and various approaches adopted to conduct the experiments. Selection of hydro turbine materials, collection of samples, bench scale equipment, and testing procedures approaches are all presented in this chapter, as well as the characterization of silt particles and slurry. Surface morphology, chemical composition, dispersion, particle size/shape, static settling concentration, bulk density, pH value, and crystalline structure are only some of the features of dam silt discussed in this chapter.
- *Chapter 4* summarises the silt erosion findings made with hydro turbine materials and HVOF coatings with respect to parameters namely propeller's rotational speed, particle size, and solid concentration. The approach of design of experiments has been used to analyse the most influential element. Ceramics based coatings namely Al_2O_3, Cr_2O_3 and 55% Cr_2O_3+45% Al_2O_3 composite HVOF coatings were used to protect the hydro turbine's blade materials. This chapter also explains the synergistic impact of CeO_2 addition on silt erosion of these ceramics coating. The microstructure, crystalline phases of as-sprayed coatings, roughness, porosity, micro hardness, and other properties of coatings are also studied.

- *Chapter 5* summarizes the optimization of erosion wear using Design of Experiments. The effect of parameters namely rotation speed of propeller, particle size, and solid concentration is also discussed.
- *Chapter 6* compiles overall summary of the thesis. Various findings from this thesis work with future perspectives.

CHAPTER 2
LITERATURE REVIEW

From the previous chapter, it can be concluded that the materials specifically used in areas of corrosion and erosion suffer from degradation due to the catastrophic environment. This leads to the loss of life of the material which further creates problems such as unwanted shutdowns or downtimes. This will directly impact the working of the hydropower plant and also increase the cost of maintenance and repair. Such a phenomenon of erosion is inevitable. However, according to the available literature, certain surface modification techniques can be used to enhance the properties of such materials. A number of researchers have studied the silt erosion characteristics of various hydro turbine materials under the effect of a wide range of conditions. So, a literature survey is carried out with the objective of providing an inclusive literature survey about erosion wear of hydro turbine materials and coatings. This chapter provides a state-of-art on different types of coatings based on the coating process, coating parameters, coating materials, materials type, etc.

2.1 STATE-OF-ART ON SILT EROSION IN HYDROTURBINES INSTALLED IN THE HIMALAYAN RANGE

As was discussed in the prior chapter, silt erosion is a major issue for many hydroelectric facilities, particularly those situated in or near the Himalayas. Several factors, including particle size, particle concentration, particle hardness, etc., affect the rate at which silt erodes. The material's lifespan decreases as the rate of erosion increases. Therefore, it is crucial to understand which parameters boost the erosion rate and which do not have much of an effect. These investigations will make it simple to understand and overcome an erosion issue, which will be time saving. Swarnakar et al. (2008) studied on silt erosion in hydro turbines and discovered it to be a common issue in the lower Himalayas. There is a lot of quartz in the silt that is found in India. Reasons for this include the Himalayas' young age as a mountain range, the high river gradients in the region, widespread deforestation, and severe climate extremes. Here is a summary of the research done by a variety of scholars on hydro turbines in the Himalayas:

Naidu (1997) proposed the following formula for estimating the rate of silt erosion:

$$W = S_1 S_2 S_3 S_4 M_r v^x \tag{2.1}$$

Where S_1 represents the silt concentration coefficient, S_2 represents the silt hardness coefficient, S_3 represents the silt particle size coefficient, S_4 represents the silt particle shape coefficient, M_r represents the base material wear resistance coefficient, and v represents the velocity of the water. There are a few other potential numbers for x: for a Francis runner, it can be equal to 3, for guide vanes and pivot ring liners, it can equal 2.5, for a Pelton nozzle, it can equal 2.5, and for Pelton runner buckets, it may equal 1.5.

Bajracharya et al. (2008b) carried out an investigation of the Pelton turbine runner at the Chilmi Hydro Electric Plant (CHEP) in Nepal. They determined that there is a correlation between the rate of erosion of the nozzle's spear and the loss of efficiency experienced by the runner. The major purpose of the study was to investigate the link between erosion of a Turgo impulse turbine runner and factors such as the size of the silt particles, the concentration of the silt particles, the jet velocity, the jet diameter, and the amount of time the turbine was in operation. They tested the hypothesis that there was a correlation between the particle size and the rate of erosion throughout a spectrum of quartz concentrations by collecting data from several locations. It has been suggested that the erosion rate include the following elements:

$$\textit{Erosion rate} \propto a(\text{size})^b \tag{2.2}$$

Where a and b are constants with changing values depending on the proportion of quartz. Furthermore, the following equation may be used to illustrate the link between erosion rate and efficiency of reduction:

$$\textit{Efficiency reduction} \propto a\ (\textit{Erosion rate})^b \tag{2.3}$$

Chauhan et al. (2008) explored the 13/4 martensitic stainless steel, which is often used for underwater component manufacturing in hydropower projects. However, there is a number of upkeep issues associated with using this steel. Nitronic steel, also known as 21-4-N, was created as a solution to these problems. Using a gas jet tester, researchers tested and compared the eroding behaviour of steels with the grades 13/4 and 21-4-N when subjected to solid particle impingement. Throughout the duration of the erosion testing, the particle velocity, the impingement angle, and the test duration were all meticulously controlled. The nozzle was maintained 10 mm from the target for the erosion test, and the particle velocity was 120 m/s. Both 30 and 90 degree impingement angle were used in the tests. Ploughs, created by the ejection of platelets from the impact zone were seen in the topography of degraded surfaces of both steels. The plough in 13/4 martensitic steel is much broader than that in 21-4-N steel, indicating more erosion damage in the former material. According to certain sources, 21-4-N nitronic steel has superior erosion resistance over 13/4 martensitic stainless steel. In addition to its high level of hardness, high level of tensile toughness, and capacity to work harden, nitronic steel has an austenitic matrix, which provides it with outstanding erosion resistance.

Padhy and Saini (2009) investigates the impact that silt erosion has on Pelton turbine bucket efficiency under varying conditions of silt concentration, particle size, jet velocity, and turbine run time. They found that turbine efficiency loss is a function of these variables that may be useful to turbine manufacturers in predicting efficiency loss for the Pelton wheel:

$$W=4.02\times10^{12}\times(s)^{.0567}(C)^{1.2267}\times(v)^{3.79}\times t \tag{2.4}$$

Where C is concentration, s is the silt size, v is the velocity and t is the operating time.

Mittal et al. (2019) identified the silt erosion area on turbine using numerical simulation and shows that significant erosion occurs at leading edge followed by sparse erosion on the bottom of the guide vanes.

Senapati et al. (2019) conducted experiments using mild steel test specimens for silt slurry using pot tester. The average metal loss was calculated for different silt slurry trails. The experimental results obtained were in good agreement with theoretical calculated values using Finnie’s model for metal loss.

Din and Harmain (2020) investigated the erosion of pelton spear and nozzle at Chenani power plant for sediment erosion. The hydro abrasive wear was defined on the measurement of material removal of erosion on spear and nozzle.

Khurana et al. (2016) conducted study to investigate the effect of silt size, silt concentration, jet velocity and operating time on performance of turgo impulse turbine for actual flow conditions. It has been reported that the efficiency loss in turbine mainly depends upon silt parameters.

Rai et al. (2020) analysed the hydro abrasive erosion due to suspended sediments which leads to failure of hydro power machinery. Experiments were conducted utilizing diverse velocity ranges, exposure time, sediment size and concentration for developing different erosion models which are useful for proper planning of preventive measures.

Gautam et al. (2020) investigated that the life and efficiency of the turbine part deteriorates due to the erosive and abrasive wear. The parts mostly eroded include guide vanes and runner blades of Francis turbine at Bhilangana hydro power plant. Numerical flow analysis of turbine is conducted to define the causes of various erosion patterns in turbine parts. Also, the effects of shape and size of quartz particles have shown that the erosion is directly proportional to these parameters.

Kumar and Saini (2022) analysed the silt erosion problems for the underwater hydro power plants. An investigation has been done to develop the correlations for efficiency factor using curve fitting, ANN and support vector machine methods. The developed correlation can be useful for developing efficient operating and maintenance strategies for hydropower plants.

2.2 STATE-OF-ART ON EROSION OF VARIOUS COATINGS FOR HYDROTURBINES

Numerous studies have improved our understanding of silt erosion in hydro turbine coatings, and that knowledge is summarized here. Coatings are placed to the surface of the turbine material in order to increase its usable life and decrease the likelihood of it being damaged. According to the literature research, the thermal sprayed surface coatings and claddings, depending on the mechanical and chemical qualities of the deposited material and the conditions of the deposition, are a substantial asset for strengthening the component's resistance against slurry erosion (Sugiyama et al., 2005; Wang et al. 2020, 2021; Zhang et al. 2022; Zhou et al. 2021). The most common types of thermal spraying are known as wire-arc spraying, detonation gun spraying, plasma spraying, and high-velocity oxy-fuel (HVOF) (Tucker Jr, 1994; Vasudev et al., 2022, 2021, 2020). Components needing protection from corrosion, erosion, and wear often make use of HVOF coatings. When compared to alternative spraying processes, it has low porosity, superior density, and noticeable coating cohesive strength (Crawner, 2004; Prasad and Modi, 2009). Many studies have looked at various coating compositions to better protect hydraulic parts from erosion wear (Mann, 2000; Santa et al., 2009, 2007). Recent studies have indicated that WC-based coatings have gathered the most interest, with WC-Co-Cr coatings demonstrating good results against slurry erosion. This is due to the fact that these coatings are more resistant to erosion (Clark et al., 1999; Grewal et al., 2012). Ni-Al_2O_3 based coatings, which have been explored by certain researchers, are a step forward since they are low-cost coatings that considerably increase erosion resistance (Grewal et al., 2013b). Tribological research have been performed by just a select few authors in order to optimize Al_2O_3+TiO_2 blends for enhanced erosion resistance when placed on mild steel (Singh et al., 2020).

Increasing the hardness of intermetallic Ni-Al based coatings by adding CeO_2 was studied by certain researchers, and they came to the conclusion that coating hardness plays a major role for increasing erosion resistance (Wang et al., 2003). Researchers have observed that nitriding 13/4 stainless steel increases its hardness and decreases its nitriding temperature, both of which have a knock-on impact on erosion resistance when exposed to silt (Prakash and Nath, 2018). In addition, several researchers have conducted a wide variety of studies to generate new kinds of compositions. The great hardness, high strength, excellent oxidation, and anti-wear qualities of oxide ceramics make them another viable coating option (Dong et al., 2013; Edlmayr et al., 2010). Below, we'll go into detail about the studies conducted by various researchers on various hydro turbine coatings:

Zu et al. (1990) a jet-type slurry tester was used in order to investigate the impact that slurry erosion has on aluminium, copper, mild steel, and alumina specimens. Researchers have looked at what the link is between the rate of erosion and the velocity of slurry of silica sand that ranges in size from 66 to 1000 micron meter. It was also discovered that due to the brittle nature of alumina, erosion wear increases with an increase in impact angle, with the maximum value being observed at an angle of 90 degrees. In contrast, the rate of erosion of other materials rises with increasing impact angle at a small angle of incidence, reaching a peak around 40 degrees, and then progressively decreasing for higher impact angles. This phenomenon occurs when the angle of impact is increased from a small angle to a larger one. Alumina having greater hardness was shown to have the lowest erosion rate compared to the other materials studied. As the impact angle increases towards 90 degrees, the rate of erosion of alumina elevates as well.

Tianmin et al. (2003) consider utilizing martensitic steel that is 2Cr13Ni in composition and can be hardened with a laser. In a ball-on-flat impact device, a hypo eutectoid laser-hardened 2Cr13Ni martensite stainless steel that had been laser-hardened was put for impact testing behaviour. According to the findings, the impact behaviour of 2Cr13Ni that had been treated with a continuous wave CO_2 laser was much better than that of 2Cr13Ni that had been treated with conventional heat. Results revealed that impact wear scars on 2Cr13Ni specimens decreased in size when the surface hardness was raised. Researchers observed that when laser surface-processed steel was compared to conventionally treated 2Cr13 Ni steel, the former displayed much improved impact wear resistance. This was due to both the grain refinement and the greater martensite concentration near the surface that occurred from quick cooling. Both of these factors were the consequence of rapid cooling. They discovered that fatigue spalling was the primary source of wear for surfaces that were constructed of 2Cr13Ni stainless steel that had been heat treated in the typical manner. The beginning of fatigue spalling in 2Cr13Ni stainless steel may be delayed by the use of laser treatment.

Wang et al. (2003) studied HVOF coatings based on the intermetallic NiAl which were tested with cerium oxide (CeO_2) and chromium. CeO_2 and Cr increased the binding strength and improved wetness of sprayed intermetallic compounds. This addition minimized thermal spraying-induced brittle peeling of NiAl intermetallic coatings. Intermetallic coatings containing CeO_2 and Cr outperform pure NiAl coatings in cracking, porosity, hardness, and elastic modulus. NiAl coatings containing CeO_2 and Cr are more valuable than Pure NiAl coatings. Sand was utilized in blast-nozzle erosion tests. Intermetallic NiAl coatings with CeO_2 and Cr resist erosion better than pure NiAl coatings. Coatings using NiAl with CeO_2 and Cr are employed because they maintain physical integrity and offer better mechanical qualities. They found that ceria may significantly increase the coating's toughness. The worn coating surface morphology was most noticeable after ploughing and cutting operations.

Zhang and Zhang (2005) were tested laser-clad Ni-Cr_3C_2 and Ni-WC coatings for ECW on martensitic stainless steel. Argon was pumped into the melt pool to insulate the alloy powder from oxidation. Treating samples at overlapping clad tracks required a 2 kW continuous wave CO_2 laser. Erosion investigations employed slurry pots. In a bowl, quartz sand and acid solution make the slurry. Stainless steel has 63.10 grams per square meter per hour ECW. Clad layers with Ni and 50% Ni and 50% Cr_3C_2 decreases the ECW rates to 43.8 and 26.5, respectively and having 30% and 60% reduction. ECW resistance rises with micro hardness, clad layer toughening, and structural carbide content. Smaller impact craters, pro-turbulent deformed lips, and smoother chipping-type craters on Ni+50%WC and Ni+50% Cr_3C_2 coatings show their robustness compared to stainless steel substrates. These analyses helped explain wear mechanisms. The toughened structure and improved work hardening ability of the Ni-Cr_3C_2 coating consume the impact energy of eroded particles in the substrate with plastic deformation, increasing ECW resistance compared to the Ni-WC coating with high hardness.

Wei et al. (2006) have looked at the plasma-enhanced magnetron sputtering (PEMS) approach for depositing thick nitrides like ZrN, CrN, and TiN, and carbonitrides like ZrSiCN and TiSiCN, on Ti-6Al-4V and SS-304 substrates for sand erosion protection. According to ASTM Standard G76-04, sand erosion tests were conducted using a nozzle at a 30 degree incidence angle to the surface. The nano-hardness and elastic modulus of the necessary substrates were also examined by the authors. The testing shows that the softest material is CrN at 24.5 GPa and the hardest material is TiSiCN at over 40GPa. The TiSiCN coating is more durable than other coatings because its elastic modulus is lower, at 299.7 GPa. The high hardness and toughness of the coatings may account for their superior erosion resistance, as stated by the authors in the following order: TiSiCN>ZrN>TiN>ZrSiCN>CrN. TiSiCN has a mass loss that is 5 to 10 times lesser than any other nitride and roughly 25 times lower than that of bare stainless steel or Ti-6Al-4V during the course of the test. The technique is most often used to shield the blades, vanes, and rotor blades of turbine engines in cutting-edge aircraft and fluid pump impellers.

Yarrapareddy et al. (2006) successfully deposited nickel-tungsten carbide powders with variable proportions of tungsten carbide particles using a laser-based direct metal deposition (LBDMD) technique on 4140 steel substrates. The coatings come in a variety of thicknesses, denoted by the numbers Ni-40W, Ni-50W, and Ni-60W respectively. Over a wide range of impingement angles, research was conducted to determine how susceptible coatings are against slurry erosion. In order to evaluate the slurry's resistance to erosion, a centrifugal force-driven jet erosion testing apparatus is used. On 4140 steel samples, coatings of functionally graded materials (FGMs) are evaluated and compared to monolithic depositions of Ni-W40. According to the results, it is possible to use the LBDMD approach to deposit defect-free Ni-W FGMs that have a constant distribution of tungsten carbide particles in a nickel-based matrix. These FGMs may be formed using nickel-based electrodes. When compared to their monolithic counterparts, it was discovered that Ni-W FGMs have a much higher resistance to slurry erosion than Ni-W40 and 4140 steels do. This is the case even though both of these steels are monolithic. Large volumes of exceptionally hard tungsten carbide particles are responsible for Ni-W FGMs' outstanding slurry erosion resistance. Erosion MRR values for required coatings will decrease when the impingement angle is reduced. For Ni-W FGMs, Ni-W40, and 4140 steels, the link between MRRs, crater depth, crater area, average surface roughness values, and impingement angles was evaluated. According to the research, there is a definite connection between all of these elements. When looking at the surface profiles of the eroded samples, it was required to use a needle-shaped probe in conjunction with a linear scale that has a digital readout. This is necessary in order to get accurate results. Calculating the depth of penetration of the craters that were formed by the slurry jet is the method that is used to accomplish this goal. The researchers found that a greater jet angle of impingement resulted to deeper erosion craters zones and a high degree of microcutting for the materials that were eroded. The observation had led to conclusion that microcutting is the main mechanism of material removal.

Manisekaran et al. (2007) examined hydro turbine steels, such as 13Cr-4Ni martensitic steels, which experience heavy-erosive wear, leading to efficiency loss as a consequence of solid particle entrapment in the water. It has been shown that surface-modified steels are more effective in terms of erosive wear resistance. This study investigates the influence of particle size (150-300µm, 150µm) and angle of impingement (45°, 60°, and 90°) on the slurry-jet erosion behaviour of laser-hardened and pulsed plasma-nitride 13Cr-4Ni steels. Because the laser hardening process martensitise retained austenite while maintaining a moderate hardness, the material performs well at all impingement angles. Chip formation and micro cutting occurred in pulsed plasma nitride steels because these materials could not withstand the repetitive stresses induced by jet impingement. All damage spots on the laser-hardened surface were also characterized by the plastic deformation mode of material removal. Pulsed plasma nitride steels, on the other hand, have shown evidence of chip formation and a micro-cutting mechanism of erosive wear. Particles in the slurry between 150 and 300 µm in size caused twice as much erosion as those at 150µm in size.

Sharma et al. (2008) reported the addition of CeO_2 into flame-sprayed coatings that are based on Ni, increases the hardness and abrasive wear behaviour of the coating. Due to the substantial high porosity, poor hardness, and big particle size, these coatings are seldom employed despite their cheap cost. This is due to the characteristics of the material and process. The tribological and mechanical qualities of coatings are determined by the microstructure, grain size, and elemental distribution of the coating. The microstructure may be fine-tuned with the use of rare earth elements (oxides). The characteristics of a powder based on Ni that is currently for sale have been improved by the addition of 0.4, 0.8, 1.2, 1.6, and 2% weight of CeO_2 respectively. Six different coatings were developed, and they are as follows: NiCrBSi+ 0% CeO_2, NiCrBSi+ 0.4% CeO_2, NiCrBSi+ 0.8% CeO_2, NiCrBSi+ 1.2% CeO_2, and NiCrBSi+ 2% CeO_2. In order to evaluate the flame-sprayed coatings' resistance to abrasion, an abrasive wear tester consisting of a pin-on-disc was used. Standard Ni-based coatings with and without CeO_2 addition were compared in terms of grain size, elemental distribution, hardness, porosity, and abrasive wear behaviour. Coatings benefit from an addition of CeO_2 at a weight percentage of 0.8 for the greatest refinement in grain size, increase in hardness and improvement in abrasion resistance. Coatings with the optimal amount of CeO_2 (0.8 weight %) have an abrasive wear rate that is 21% lower than coatings that do not include CeO_2. The increased resistance to abrasive wear is a result of many factors, including the refining of the grains and the hardness of the coatings. In addition, by doing XRD on both the original coating and the modified coating, we were able to establish the ideal percentage of CeO_2 to add to the coating, which was 0.8% by weight. The most obvious evidence of ploughing and cutting processes was found on the worn surfaces of various coating types.

Arji et al. (2009) examined Ni-Cr-Si-B coatings on mild steel which were investigated for sand slurry erosion resistance under various conditions. Slurry pot tester assessed coating and mild steel wear. Weight loss was used for measuring the wear. An electronic balance with 0.1 mg resolution weighed the specimen. The erosion wear experiments employed silica sand with concentrations of 20, 40, and 60% at three rotational speeds of 600, 800, and 1000 revolutions per minute. When using slurry with 20% silica sand, weight loss increased with rotational speed from 600 to 1,000 rpm, while when using a 40% slurry, weight loss increased from 600 to 800 rpm and then decreased marginally at 1,000 rpm. The wear ratio showed that Ni-based alloy thermal spray coating on mild steel improves wear resistance. Ni-Cr-Si-B coating wear ratios were from 1.4 to 2.8 under different test circumstances. During microstructural research, pitting, ploughing, and indentation produced Ni-Cr-Si-B coating wear. When both the concentration of the slurry and the rotating speed are high, the soft eutectic matrix that is dominated by nickel is put through extrusion and plastic deformation. In addition to this, it has been shown that an increase in the coating hardness results in improved resistance to erosion and wear in comparison to mild steel.

Iwai et al. (2009) used a chemical vapour deposition (CVD) method to study the coating's tribological characteristics. A micro-slurry jet erosion tester was used to perform the research. Alumina particles of 1.2 µm in size are used as the erodent material. CVD deposited TIC/TIN coatings placed on cemented carbide have been impacted by the high-velocity particles. Both single-layer and multi-layer coatings are tested. The authors found that compared to the TiN layer, the TiC layer had double the wear resistance. The carbon diffusion during the CVD process may be attributed for the brittleness of the interface zone of the WC substrate. The increased hardness of the coating has also been observed to make the worn debris less when it is scraped from the surface of TiC.

Shivamurthy et al. (2009) observed the laser surface alloyed coatings for 13Cr-4Ni stainless steel to better understand their slurry erosion properties. Using a slurry jet erosion test apparatus with erodent like silica sand and river sand, they investigate how changes to a number of factors affect the erosion performance of the coatings and the substrates. The authors have discussed how boron carbide improves the erosion performance of laser surface alloyed coatings by making them harder, thereby making them more resistant to erosion. In addition, the larger the size of erodent, the more it contributes to increasing the erosion wear rate.

Liu et al. (2010) has examined AC-HVAF-sprayed WC-10Co-4Cr coatings on wear-prone components. This research examines the erosion of nano WC-12Co-modified WC-10Co-4Cr powder using AC-HVAF coatings. The addition considerably led to increased hardness for AC-HVAF sprayed coatings. Addition of 15% nano WC-12Co powder to AC-HVAF coating increased its hardness from 1677 to 1873 HV. The performed sliding wear and slurry erosion tests depict how nano WC-12Co affected the material. After Nano powdering, HVAF-coated substrates showed improved resistance for wear and erosion. Compared to three different compositions i.e. AC-HVAF-0, AC-HVAF-5, AC-HVAF-10, AC-HVAF-15 has been tested the best among all for more hardness and lesser porosity. Adding more nano WC-12Co may boost wear and erosion resistance. Surface cracking was observed utilizing quartz sand with particle sizes between 400 and 625 µm in erosion experiments.

Ramesh et al. (2011) have investigated the reaction of Inconel-718 powder to slurry erosion after it has been thermally sprayed onto a substrate made of mild steel using an APS (air plasma spray) thermal spraying technique. Powders with an average particle size of 50 µm were used by APS in the production of coatings with a thickness of 200 µm and 250 µm respectively. Microstructure analysis and micro hardness testing were performed on the created coatings. Tests for slurry erosion were performed using a mixture of silica sand and 3.5% NaCl in distilled water. Microstructural analyses show that the Inconel-718 covering is homogeneous, with strong bonding and few pores. The generated coatings have a surface hardness that is superior to that of the substrate, and this advantage develops as the thickness of the coating increases. The newly developed coatings have an improved resistance to the erosive wear caused by slurry compared to uncoated mild steel. Coatings with thicker layers have been shown to have higher hardness and less porosity. Inconel-718 coatings have greater slurry erosive wear resistance than uncoated mild steel in all test circumstances, and coating thickness boosts this resistance. The created coatings are more resistant to erosion than uncoated steel when considering factors such as rotating speed, particle size, particle concentration, and time duration.

Singh et al. (2012) compared the dry slide resistance, slurry erosion, and cavitation erosion of conventional coatings to those of nano-structured Al_2O_3 coatings produced on SS-304 utilizing an atmospheric plasma spray technique. Dry sliding, slurry erosion, and cavitation erosion are just a few examples of how nano-alumina coatings' increases the tribological performance as compared against that of more traditional coatings. A pin-on-disc wear testing equipment with end loads of 5, 10, and 15 N was used to conduct dry friction and sliding wear tests. The sliding speed was maintained at a constant of 1.0 metres per second throughout. Cavitation erosion investigations used an ultrasonic vibratory tester. However, a slurry pot utilizing various silica concentrations were used for slurry erosion tests. The fact that both coatings had a laminar structure is a new finding that contributes to the existing body of literature. The NCs had a higher wear resistance compared to traditional coating and a lower friction coefficient. Slurry erosion is caused by microcutting, microploughing, and lamellar delamination. They found that Nano-structured coatings perform better than others due to their high hardness and excellent obstruction of fracture growth.

Grewal et al. (2012) has used a detonation spray cannon to deposit WC-Co-Cr coatings on certain 13Cr-4Ni and 16Cr-5Ni steel used in hydro turbines. Coatings' ability to reduce steel's slurry erosion was evaluated by analysing their behaviour in slurry erosion. The impacts of operating parameters on erosion wear were investigated with the use of a high-velocity jet-type test rig. These operating factors included velocity, impact angle, concentration, and particle size. The goal of this comparison was to determine which kind of steel, uncoated or coated, is more effective at preventing erosion wear. Sand gathered from a power plant is used as the erodent to simulate real-world turbine operating conditions. Erosion resistance in steel has been claimed to be improved with the use of a specific cermet coating. The erosion behaviour of coatings has been shown to be mostly influenced by velocity, whereas that of uncoated steels has been found to be primarily influenced by particle size. The necessary coatings demonstrated a three- to three-and-a-half-fold increase for the velocity effect. The substrate steel was also discovered to have an effect on the coating's microstructure. The erosion performance of bare 16/5 steel is superior to that of bare 13/4 steel. This is because 16/5 steel has a greater micro hardness. While plastic deformation predominates in the erosion mechanism for bare steel. Fracture originating from the interlinking of cracks predominates for deposited coatings.

Purkayastha and Dwivedi (2012) investigated the possibility of using flame spraying to produce coatings containing CeO_2 that are resistant to wear. Researchers have looked at the impact that the incorporation of rare earth oxide (CeO_2) has on the microstructure, hardness, frictional forces, and sliding wear resistance of Ni/WC. As a consequence of this, we developed six coatings each containing different percentages of ceria using nickel tungsten carbide (NiWC) and cerium oxide (CeO_2) having percentage as NiWC+0%CeO_2, NiWC+0.3% CeO_2, NiWC+0.6% CeO_2, NiWC+0.9%. The analysis revealed that improving the coatings' hardness and decreasing their porosity led to a rise in their resistance to sliding wear. Tribological testing over a wide range of sliding velocities and applied loads has shown that coatings containing 0.6 and 0.9 wt. % CeO_2 are superior. The authors state that the improved sliding wear resistance may be attributed to the material's high hardness and low porosity.

Romo et al. (2012) evaluated the resilience of the 13-4 stainless steel and Stellite 6 coatings against slurry and cavitation erosion (CR) using the Shielded Metal Arc Welding (SMAW) process. The slurry erosion tests were carried out with the assistance of the jet testing apparatus. The slurry is made up of particles of SiO_2 and regular tap water. The CR was tested in accordance with ASTM G-32 standards. Runners and liners are two examples of hydraulic turbine parts that experience slurry erosion and comparable to tests of the Slurry Erosion Resistance (SER) to those seen at high velocities and impingement angles. The findings demonstrated a 15-fold increase in CR due to the coatings compared to that of uncoated stainless steel. All impingement angles evaluated increased the coatings' SER, with the maximum erosion rate seen at 45^o. Micro-cracking was the most prominent wear mechanism in the cavitation testing, while micro-cutting and micro-ploughing were the most prominent wear mechanisms in the slurry erosion experiments. An increase in material hardness has been observed by the authors to have a significant impact on both erosion and cavitation resistance.

Grewal et al. (2012) reported the erosion behaviour of hydro turbine steels (13Cr4Ni and 16Cr5Ni) coated with WC-Co-Cr and sprayed with a detonation gun. Research has been carried out to explore the erosion effect that takes place over coated and uncoated steels by using a variety of various operating elements, such as velocity, impact angle, concentration, and particle size. These factors all play a role in the process. The experiments were performed on a high-velocity jet-style testing apparatus. The Naphta Jhakri hydroelectric facility in Himachal Pradesh, India provided the erodent particle (abrasive medium) which is used to simulate operating conditions in the turbine. Authors indicated that particle size is the most important factor in erosion of uncoated steel, but the velocity was the most important component in erosion of D-gun coated surfaces. The slurry erosion resistance of uncoated 16Cr5Ni steel was higher than that of uncoated 13Cr4Ni steel. SEM pictures revealed that plastic deformation predominated in the erosion process for the uncoated steels, whereas fracture due to the development and interlinking of fractures predominated for the coatings. It was discovered that the D-gun sprayed coating improved the substrate steels' resistance to slurry erosion.

Grewal et al. (2013b) deposited the Ni-Al_2O_3-based composite coatings on CA6NM steel using high-velocity flame spray (HVFS). Among the mechanical properties that were studied in relation to alumina content were micro hardness, density, fracture toughness, residual stress, and scratch resistance. It has been shown that the concentration of alumina in the coatings has a considerable influence on the microstructural features of the coatings. These qualities include, but are not limited to, surface roughness, splat size, porosity, and the amount of unmelted particles. The coating that was constituted of 60 weight percentage of Al_2O_3 was determined to have the greatest average micro hardness of 1159 HV. As the percentage of Al_2O_3 in the coating decreased, the micro hardness also did, with the Ni+20%Al_2O_3 coating having the lowest average hardness (563 HV). After conducting scratch tests, it was discovered that cracking and spalling of layers were the primary factors responsible for the damage to coatings. There was not a linear connection between the proportion of alumina and the fracture toughness of the material. When coated with nickel and 40% aluminium oxide, the material exhibited the highest level of toughness.

Goyal et al. (2012) used a high-speed erosion test setup to examine the performance of HVOF-sprayed Cr_2O_3 on selected turbine steel in a variety of hydro-operative settings with lean slurry. It was discovered that Cr_2O_3 coated samples fared better against slurry erosion than their uncoated counterparts, with the coating displaying a mixed behaviour that was mostly brittle.

Grewal et al. (2013a) reported friction stir processing (FSP) on the surface of 13Cr4Ni steel, popular steel for use in hydro turbines, was reported. They hypothesized that applying FSP to a metal's surface would improve the metal's mechanical qualities, such as its hardness and toughness. They ran some tests and found that the treated steel was much harder than the untreated steel.

Hong et al. (2013) examined the cavitation erosion behaviour of HVOF sprayed Cr_3C_2-NiCr coating. They came to the conclusion that a higher concentration of silt led to a higher rate of wear.

Yadav and Mishra (2013) tested the D-gun thermal sprayed ceramic coatings applied on 431 stainless steel for providing the erosion resistance and found that both Al_2O_3-40TiO_2 and Al_2O_3-13TiO_2 performed well. A pot-type slurry erosion tester was used in order to assess the resistance of the coatings to erosion caused by slurry. The basic conditions for slurry erosion wear testing include the angle of impingement, the concentration of the slurry, and the kind of coating used. SEM images were used to analyse the surface morphology. Micro-structural analysis was used to investigate and analyse erosion behaviour and the process of material loss. Ceramic coatings of Al_2O_3-13TiO_2 were placed on SAE 431, and they proved to be more resistant to slurry erosion than both Al_2O_3-40TiO_2 and the uncoated substrate. This might be because of high surface hardness. The decreased erosion rate may be attributed to the increased concentration of Al_2O_3, the harder phase, in this coating. Erosion wear was observed to be greatest at 30 degrees and least at 90 degrees impact angles. Erosion wear is caused by microcutting, ploughing, and scratching mostly.

Singh et al. (2014) tested dry sliding and slurry erosion of plasma-sprayed nano-structured Cr_2O_3-3TiO_2 coatings put on a 304 stainless steel substrate and compared to normal Cr_2O_3/TiO_2 powder coatings. When the performance of the coatings is studied in terms of mechanical and tribological characteristics, it has been discovered that NC3T produces stronger adhesion strength than CC3T, which suggests that NC3T provides better intersplat bonding. According to reports, coatings constructed of NC3T, which are harder and less porous than other coatings, have demonstrated improved resistance to the erosion caused by slurries. When compared to the conventional coating, the nano-structured coating demonstrates a 25.8% increase in its resistance to sliding wear. The nanostructured Cr_2O_3-3TiO_2 coatings that were coated by plasma spray suffer from abrasive wear as a result of their exposure to dry environments. The wear mechanism of typical plasma-sprayed coatings is a combination of abrasive wear and brittle fracture; nonetheless, abrasive wear is by far the more important of the two types of wear. On the worn surface of the CC3T samples, in comparison to the NC3T samples, larger pits and more debris can be visible, which indicates that sliding wear is the mechanism of wear. Pits are an indication of wear caused by ploughing, while worn debris on the sliding surface stimulates abrasion.

Yang et al. (2016) have looked at how the plasma spray method may deposit Al_2O_3, Al_2O_3-Cr_2O_3 composite coating on stainless steel. A novel solid particle impact slurry jet tester was used to measure the coatings' resistance to erosion and wear. The Al_2O_3-Cr_2O_3 composite has been shown to outperform the Al_2O_3 coating in mechanical tests. Compressed air was combined with the slurry in the nozzle before being injected at high speed into the coated surface. When slurry was injected onto the surface of the coating material, it caused wear advancement, also known as wear rate, which was directly proportional to the erosion resistance of the coating material. A coating composed of an Al_2O_3-Cr_2O_3 combination has a stronger resistance to erosion and wear than a coating made of pure Al_2O_3. We also tested the coatings' resistance to sliding wear under rigorous circumstances. Based on the data, it seems that Al_2O_3-Cr_2O_3 composite coatings are superior than Al_2O_3 coatings in terms of mechanical, thermal, and anti-wear qualities. Al_2O_3 may be stabilized with the help of Cr_2O_3. Composite coatings improve in terms of porosity, hardness, bending strength, and heat conduction performance when Cr_2O_3 concentration in the starting composite powders rises. Al_2O_3 and Al_2O_3-Cr_2O_3 coatings were found to have porosities of 3.150±4.6% and 1.860±2.8%, respectively, and micro hardness values of 9.670±15 and 12.170±12, respectively. At the same time, the bending strength of AC70 composite coating is maximum. As a result, 70 wt.% of the composite powder employed in this investigation included 70wt% Cr_2O_3 for which composite coatings' improved resistance to erosion is due to their higher hardness and low porosity value.

Rao et al. (2017) examined plasma-sprayed Cr_2O_3 coatings on steel substrates which were subjected to sand slurry containing 3.5% NaCl solution to determine their slurry erosion behaviour. The slurry was made using silica sand with particles measuring 312 µm in size and distilled water. Using an atmospheric plasma spray method, Thermal spraying was used to apply Cr_2O_3 powder particles to a Ni/Cr bond-coated 410 steel surface. The typical coating thickness was around 200 µm. Researchers examined the effects of changing variables, such as sand slurry concentration, on slurry erosion. SEM, XRD, and EDS studies were performed on both coated and uncoated steel surfaces to determine the mechanism of erosion. The resistance to erosion was measured by the amount of weight lost. The result shows that the thick and hard Cr_2O_3 coated surface provides excellent erosion resistance in comparison to uncoated substrates.

Goyal (2018) determined the erosion behaviour of Cr_2O_3-50%Al_2O_3 HVOF and plasma sprayed coatings on CA6NM hydraulic turbine steel using a jet tester under hydro-accelerated conditions of lean silt slurry. Different operating parameters, including velocity, impact angle, slurry concentration, and average particle size, have been examined to better understand erosion behaviour. Samples were examined to determine their micro hardness, surface roughness, and porosity in their as-coated state. SEM-EDS analysis was used to examine the as-coated samples to determine the microstructure of the coatings. According to the results, the erosion rate of these coatings is primarily affected by the velocity, impact angle, and slurry concentration. The erosion rate was only moderately affected by the average particle size. Higher micro hardness, lower porosity, and better surface finish were observed in Cr_2O_3-50%Al_2O_3 coatings deposited using the HVOF process compared to coatings sprayed using the plasma process. The high velocity and relatively low temperature of the HVOF spraying technique may be responsible for this phenomenon. The corrosion resistance of HVOF-coated CA6NM samples was much better than that of plasma-coated samples. This was due to the improved hardness of the HVOF coating. When testing coated and uncoated steel samples, it was discovered that the greatest amount of erosion occurred at an impact angle of 90 degrees, while the least amount of erosion occurred at an impact angle of 60 degrees.

Hu et al. (2019) studied on Q345 low alloy steel, coatings of TIG-welded cobalt and laser-clad nickel as potential materials for higher resistance to cavitation erosion (CE) and slurry erosion (SE). These two types of erosions are caused by different types of fluids. Specific erosion models were suggested after a comparison of the commutative mass loss, erosion morphology, and roughness of CE and SE resistances. They claimed that the cobalt-based coating that is used in TIG welding mostly comprises of a γ -Co matrix and inter-dendrites that are composed of $Cr_{23}C_6$, and that it has a hardness of around 368.5 $HV_{0.2}$. The laser cladding process resulted in the production of a coating made of nickel-based phases. These phases comprised 650.6 $HV_{0.2}$ hard γ -Ni/$FeNi_3$, BNi_3, $Ni_{2.9}Cr_{0.7}Fe_{0.38}$, $Ni_{31}Si_{12}$, and Cr_xC_y phases. Both coatings had a smooth appearance and did not exhibit any signs of pores. When compared to the coating made of nickel, the CE resistance exhibited by the coating made of cobalt was nearly two and a half times as high. The resistance to SE was about 8.4 times higher in the coating that was based on nickel as compared to the coating that was based on cobalt. The high SE resistance of a material is determined by the ideal balance of the material's hardness, elastoplasticity, anchoring, and shielding activities. This optimal balance is what defines the high SE resistance of the material.

Singh and Zafar (2019) investigated the microwave cladding's potential as a surface modification approach for reducing the impact of slurry erosion. In the current study, a microwave cladding procedure is used to apply a Ni+20wt%Cr_7C_3 composite clad on CA6NM hydro turbine steel. Microwave exposure period is analysed for its impact on clad microstructure and on the slurry erosion characteristics. Developed clads were tested for fracture toughness, micro hardness, and microstructure. In order to determine how susceptible completed cladding is to erosion, slurry jet erosion tester is used. The erosion trials were ran for a total time of one hour and twenty minutes at a jet speed of forty metres per second and at an impact angle of ninety degrees. Performance in slurry erosion was evaluated by measuring wear loss, wear rate, and wear processes of the created clads. The microstructure and performance of produced clads are said to be primarily affected by the length of time they were exposed to microwaves. The microstructure analysis also indicates that as the matrix composition of the cladding is minimal, thus the carbide stays firmly rooted in it, giving it the highest erosion resistance compared to the uncoated steel.

Wahab and Ghazali (2019) investigated the durability against erosion of Al_2O_3-13%TiO_2 coatings produced via laser textured plasma spraying (LST) on mild steel. The textured coating was evaluated by the researchers and contrasted with a non-textured coating in terms of attributes such as its resistance to erosion and wear, as well as its hardness and phase composition. A series of conventional slurry pot erosion experiments were carried out in silica (SiO_2) slurry in order to investigate the effects that different impact angles have on erosion. The tests were carried out in sequence from smallest to largest. The technique of scanning electron microscopy (SEM) was used in order to define the microstructural properties of both textured and non-textured coatings for the purpose of determining the mechanism of erosion wear for the coatings. The LST approach was proven to be an effective way of changing the surface characteristics of a plasma-sprayed Al_2O_3-13%TiO_2 coating, while having only a small influence on the coating's mechanical properties and phase composition. This was shown by the fact that the LST method was successful in accomplishing this goal. The erosion scar and fracture propagation patterns may be seen by the SEM study of the coated surface. Coating mass was lost more rapidly at an impact angle of 90 degrees than at 30 degrees. This research discovered that the coating's resistance to erosion could be improved by as much as 45% at an impact angle of 90 degrees and a slurry velocity of 750 revolutions per minute (rpm) by etching a micro-grooved structure into the surface of the coating. The researchers used slurry with a velocity of 750 revolutions per minute (rpm). The authors state that the LST method is an easy way to create a textured surface on ceramic coating with little or very little surface degradation. Based on the results, it seems that the textured ceramic coating performs better, especially in slurry erosion situations. It has also been observed that the grooves were quite effective in stopping fractures from spreading to other regions, thereby decreasing the amount of material lost from the Al_2O_3-13%TiO_2 coating surface, which has significant applications in a number of different sectors, most notably the maritime sector.

Sharma et al. (2020) examined on SS-304 steel, the effect of impact velocity, impact angle, and slurry concentration as it related to HVOF sprayed coatings of Cr_3C_2-25NiCr and WC-10Co-4Cr. It was determined that the superior performance of WC-10Co-4Cr was due to the coating system's high hardness.

Prasad et al. (2022) measured the effectiveness of AZ91 alloy by slurry erosion studies with and without ceramic coatings. Al_2O_3, Al_2O_3-30%CeO_2, and Al_2O_3-40%CeO_2 are the compositions of the coating particles that will be coated on the surface of the AZ91 alloy. HVOF process was used to apply the coating. Microstructure examination by scanning electron microscopy (SEM), X-ray diffraction (XRD) analysis of the deposited coatings to learn how separate phases were formed, indentation resistance measurement by micro hardness testing, and mass loss by slurry erosion testing were all performed on the newly fabricated composite coatings. Mass loss was also measured by conducting a slurry erosion test. Measurements of mass loss of both uncoated and coated substrates were made as a function of slurry particle size (100–400 µm), slurry concentration (50–150 g/l), and slurry speed (500–1500 rpm). SEM micrographs taken in cross section revealed strong adherence to the AZ91 surface and little porosity. Micro hardness was measured and found to be highest for the Al_2O_3-40%CeO_2 coating and lowest for the uncoated AZ91 alloy. The coating was subjected to a slurry erosion test, and the increase in percentage of CeO_2 in the composite coating reduced the amount of mass lost. The authors found that erosion rates were directly proportional to increase in erodent particle size, slurry concentration, and slurry velocity. The eroded surfaces of uncoated AZ91 alloy showed ductility in a slurry erosion test, whereas the eroded surfaces of coated AZ91 alloy showed brittleness.

Zamani et al. (2022) studied the properties and erosion-corrosion resistance of carbon steel with composite coatings of Al_2O_3, Cr_2O_3, and Cr_2O_3-25, 50, and 75 wt.% Al_2O_3 deposited with atmospheric plasma method. Both as-sprayed and epoxy resin-sealed coatings were subjected to corrosion investigations, including potentiodynamic polarisation, electrochemical impedance spectroscopy, and extended immersion in a 3.5 wt.% NaCl solution. Microstructure and phase composition of coatings were investigated by XRD, optical microscopy, and SEM before and after corrosion experiment. The results showed that the Cr_2O_3 coating offered the highest protection against corrosion because of its dense microstructure and maximum adhesion strength. The Cr_2O_3-25% Al_2O_3 coating was the least corrosion resistant because it exhibited the most interconnecting porosities. The as-sprayed coatings caused the polarization resistance (R_p) to rise by a maximum of 3.93 times during the polarisation experiment, but the charge transfer resistance (R_{ct}) rose by a 3.5 times during the EIS experiment. After being submerged for an extended period of time, a coating composed of 25%Cr_2O_3-5%Al_2O_3 spalled off of the substrate due to stresses produced by the accumulation of corrosion products at the coating-substrate interface. One factor is how long coatings lasted was how well they stuck to their surfaces as determined by the adhesion strength.

According to the research that was conducted, it was discovered that surface treatments, such as coatings, may improve the surface's hardness, and this was discovered to be the most effective and widely used method that can be used to customise the property of base metal (Singh and Nath, 2022). Coatings applied using the thermal spray technique were found to be one of the efficient ways that can be utilized to deposit a broad range of powders with fewer difficulties after thorough observation from the research published before. Depending on the base metal and the intended use, coating may significantly improve the metal's mechanical qualities. It is important to weigh the benefits and drawbacks of each thermal spray procedure before settling on one for a certain application. Despite the fact that many reports have demonstrated the usefulness of HVOF sprayed coatings on turbine materials, some scepticism remains. Nonetheless, HVOF sprayed coatings have a lot of untapped potential that could be explored by experimenting with different powder combinations. The great hardness, strength, and chemical inertness of ceramic powders like Al_2O_3, Cr_2O_3, and CeO_2 make them promising candidates for use in applications requiring the transport of slurries.

2.3 NEED FOR PROPOSED RESEARCH WORK

The hydropower potential of the area is the most suited source of energy that can be settled in the upper and middle Himalayan landscape. Over the course of many years, many hydropower plants have been producing electricity by tapping into the region's abundant hydro resources. Rivers in the Himalayas are sourced by Quartz, feldspar, and other hard particles due to weathering and sedimentation of rocks. The monsoon season brings a lot of runoff, which carries a lot of silt into the hydro turbines, severely harming the turbine components. In upper Himalayan range (high altitude) hydropower plants, the silt concentration typically stays below 10%. However, hydropower plants in the lower Himalayan range (lower altitude) have a higher concentration of silt. The silt content might reach 30% at times. Turbine blade erosion is further exacerbated by the high amounts of silt (almost 12000 ppm) in Himalayan rivers. Hydro turbine blades may be eroded depending on a number of factors, including the size and hardness of the silt, the concentration of the silt, the flow rate through the turbine, the angle of contact, and the quality of the base material. Silt is very abrasive, and it may accelerate the wear of hydro turbine components including blades, runners, seals, liners, passages, and more. Guide vanes, runner blades, liner plates, etc., in Francis turbines show extreme erosion. Silt erosion at Maneri-Baira-Siul, Salal, Dehar, etc., has caused serious problems for a huge number of Francis turbines. The turbine components degrade rapidly in the high quartz-rich silt. Silt causes hydro turbines to erode, which decreases their efficiency and lifespan and must be addressed urgently. The operational and maintenance costs skyrocket as a result. Silt erosion of hydro turbines is a known issue, and it is especially problematic in the Himalayas because to the youth and fragility of the mountains there. Erosion may be reduced in turbine blades by improving their surface qualities, which is why our study is necessary. Thermal spray coating methods are often used to deposit a broad range of metallic, cermet, and oxide coatings on surfaces, and may be employed to accomplish this goal. Due to their high bond strength and low porosity, HVOF and Detonation-gun spray processes are gaining a lot of attention among the thermal spray processes. Therefore, this research will analyse the differences between silt erosion on uncoated and thermal spray-coated surfaces. The substrate will be coated with a variety of coatings. Silt slurry collected from operational hydropower plants will be used to expose the samples. This research will aid in determining which of the investigated coating/substrate combinations is the most effective.

2.4 GAPS IN LITERATURE

Based on the literature review, the following gaps in erosion wear characteristics of the solid-liquid suspensions are observed:

1) Erosion wear parameters for multi-sized silt slurries and their effect on hydro turbine components have only been partially studied.
2) The procedures for surface modification may increase the resistance of the material to erosion and wear. There is a wide range of scope available for surface modification with different combinations of coating materials.
3) There is a significant amount of variance in the data produced by the various test rigs because it is difficult to regulate the numerous factors that are responsible for erosion and wear.
4) The literature review on erosion wear reveals that most of the studies performed with the variation of velocity, solid concentration, and time duration. There is just a very little amount of data available about the impact that different silt particle sizes and shapes have on erosion wear.

2.5 PROBLEM STATEMENT

Many examinations and evaluations have been done for hydro coated turbine materials; still a lot of scope is available for drawing attention on HVOF sprayed coatings by using various commercially available powders. In this context, this study is conducted for the improvement of the turbine material by HVOF coating at high silt concentration. In the present study the endeavour is to experiment the impact of the multi sized silt slurry of different particle range by using the slurry pot tester on the erosion behaviour of the bare stainless steel material SS-304 and also on the different coatings of Al_2O_3, Cr_2O_3 and composite coating of composition 55% Cr_2O_3 + 45% Al_2O_3 developed by HVOF process on the substrate material which were then analysed in terms of the erosive wear in order to approximate their potential applications for use in an hydraulic turbines under controlled slurry erosion conditions. Secondly, the conventional coatings can be also modified by using Ceria (CeO_2). Therefore, to analyse the effect of addition of CeO_2 at different concentrations to the composite coatings for studying the silt erosion wear characteristics at different experimental testing parameters as limited literature is available to this context. CeO_2 has been chosen in the present study because of its ability to enhance the properties of coating and alloys. A study has been reported where the researchers have given the few insights and have evaluated the increase in hardness, improvement in microstructure and abrasive wear resistance of the flame sprayed nickel based coatings after adding CeO_2 (Sharma et al., 2008).

2.6 OBJECTIVES OF THE PRESENT STUDY

1) Investigation of physical characteristics of slurry suspension of silt.
2) Investigations of erosion wear characteristics of uncoated and HVOF/D-gun coated turbine materials under the influence of rotational speed, solid concentration, and particle size.
3) Identification of dominant factors for erosion wear using design of experiments.

2.7 RESULTS ORIENTATION

Results from different experiments were plotted by using different mathematic tools like Root, Origin 8.5, Image Analyzer, Minitab, etc. The use of software tools is written below:

- The graphical representation of different terms was done by using Origin 8.5 and Root.
- Minitab 17.0 was used to apply the design of experiment (DOE) techniques.
- Image Analyzer software package was used to perform the porosity analysis from SEM images.

CHAPTER 3

CHARACTERIZATION OF ERODENT MATERIAL

In previous sections, the motivation and objectives of the present work were highlighted. To achieve these objectives, different facts have been identified which are given in detail in this chapter. Various equipment, methods, techniques and procedures were employed to achieve the objectives of the present work. The methodology behind the present study has been explained in the flow chart represented in **Figure 3.1**. The parts of the research methodology in the present study are the selection of materials and the selection of equipment, procedures, methods and techniques.

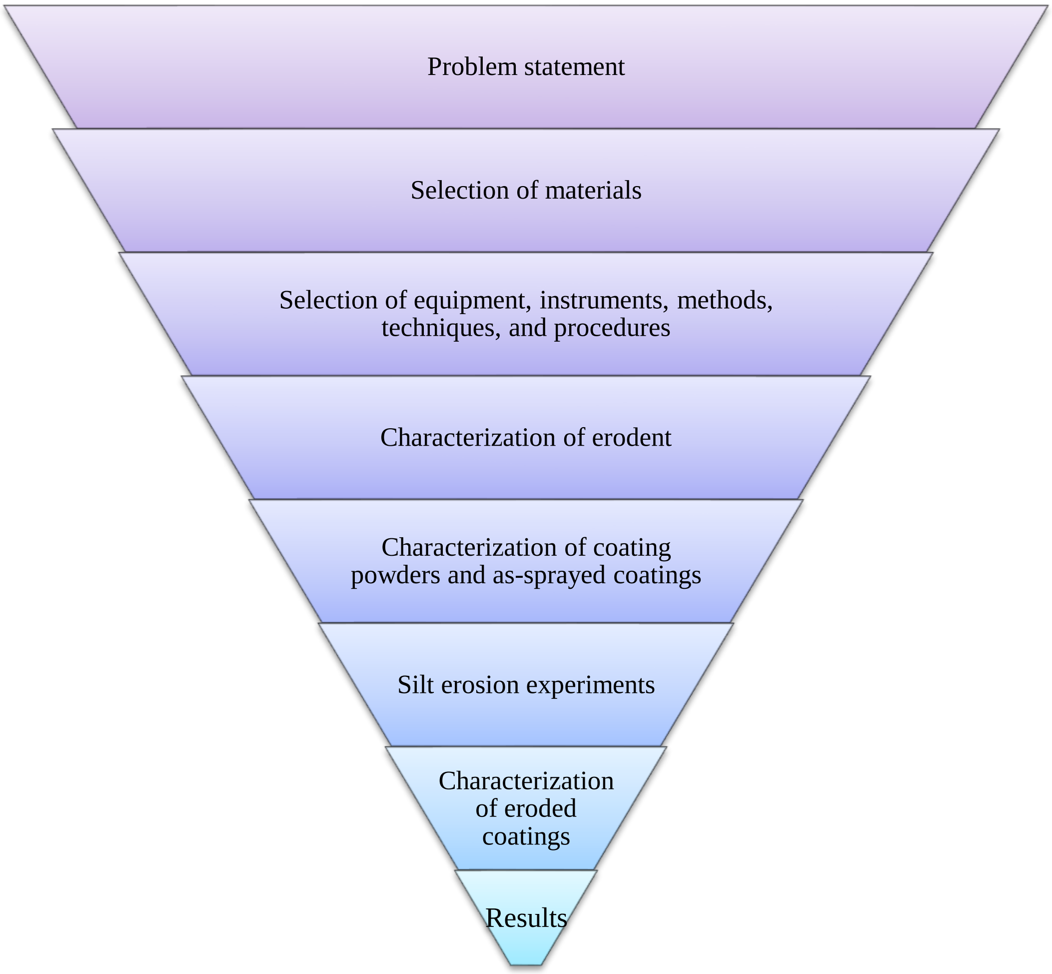

Figure 3.1. Flow chart for experimental methodology.

3.1 SELECTION OF MATERIALS

There are three categories of different materials i.e. hydro turbine blade material, erodent, and coating powder. A flow chart on selection methodology is illustrated in **Figure 3.2**. In this section, the selection of these materials has been explained.

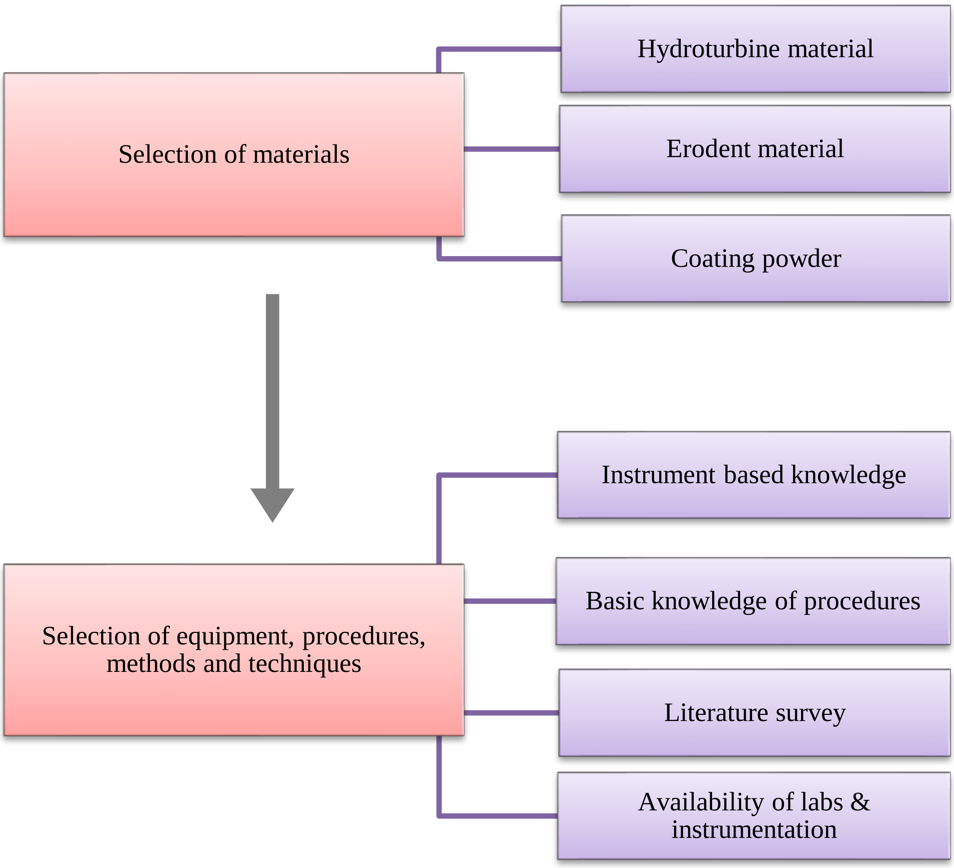

Figure 3.2. Flow chart of selection methodology.

3.1.1 Collection of erodent samples

Silt laden rivers flows through the mountainous region and to hydropower plants. This erodent material is dangerous for the life of hydro turbine blades. Sand silt was chosen to act as the eroding medium for the investigation of silt erosion that was carried out for this particular research project. The northern region of India provided the location for the collection of silt samples. The silt has been collected from the Baglihar hydropower project in Jammu and Kashmir (J&K) India, as shown in **Figure 3.3**.

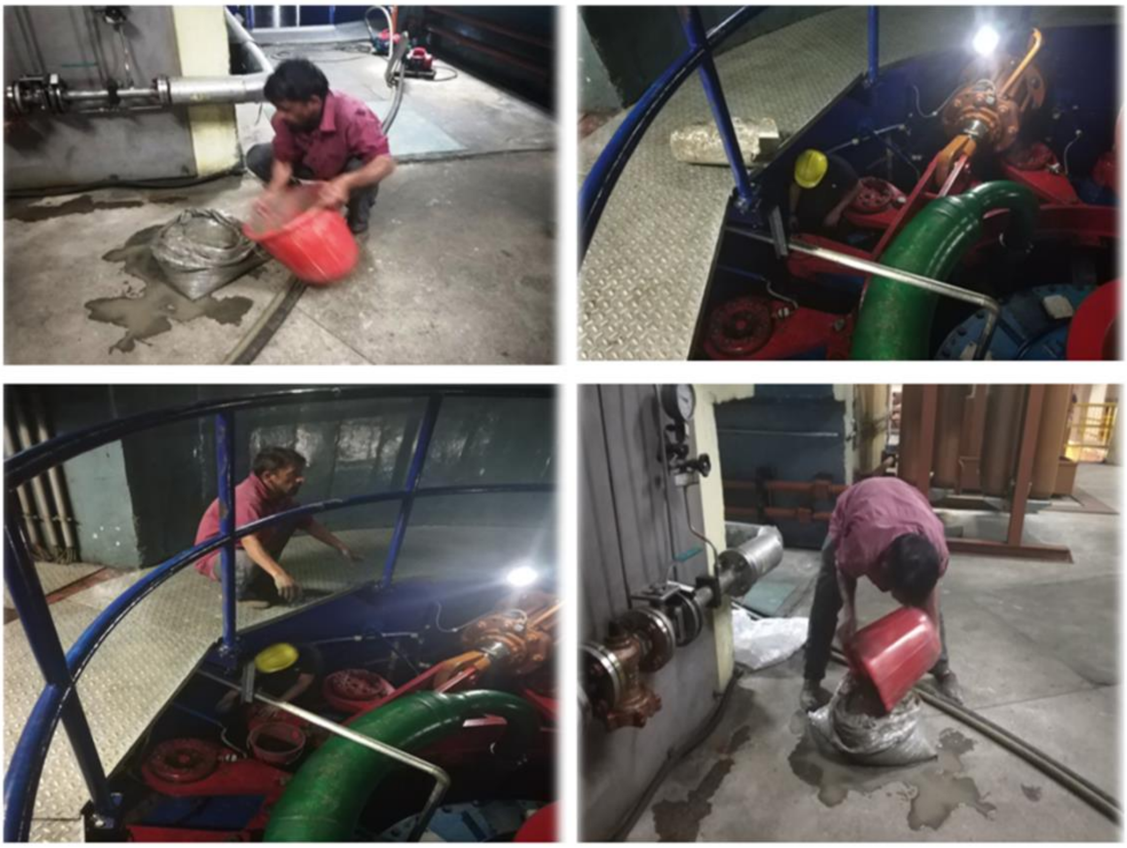

Figure 3.3. Silt Collection at Baglihar Hydro Electric Power Plant, J&K, India.

3.1.2 Hydro turbine and coating materials

The hydro turbine material SS-304 (18Cr10Ni) was selected based on the literature survey and hydro turbine application. This material is widely used to fabricate turbine blades, valve seats, casings, etc. However, the coating materials namely Cr_2O_3, Al_2O_3, and CeO_2 were also selected based on the literature survey. Various combinations are tried and optimized by blending different weight percentages which has been deeply investigated in this study.

3.2 MATERIALS CHARACTERIZATION TECHNIQUES AND METHODS

The literature review that was carried out in the previous chapter indicated that the varied characteristics of erodent materials have a significant impact on the silt erosion of hydro turbine materials. So, the characterization of the materials is an essential aspect of the evaluation of silt erosion. In this context, it is required to study the physical, chemical, and mineralogical properties of silt particles and slurry. In this chapter, an investigation of numerous properties of silt particles is carried out such as the surface morphology, chemical composition, particle size distribution, bulk density, pH value, and crystalline structure. Apart from the study of silt particles and slurry, the hydro turbine material and coatings are also characterized for their physicochemical as well as mechanical properties. The physicochemical characterization involves surface morphology, elemental composition, and crystal composition analysis. The other properties such as roughness, micro hardness, and porosity of the coatings were also studied. The different instruments, equipment, methods, techniques, and procedures were selected based on the literature survey, instrument-based knowledge, basic knowledge of procedures, and availability of instrumentation in institute laboratories and departments, as illustrated in **Figure 3.2**. The techniques of surface investigation that were used in this study are referred to as scanning electron microscopy (SEM), energy dispersive spectroscopy (EDS), and X-ray diffractometry (XRD). Each of these methods will be addressed in more depth in the following sections:

3.2.1 Scanning electron microscopy (SEM)

To investigate the surface microstructure of erodent particles, morphological analysis is often used. At the Sophisticated Analytical Instruments (SAI) Laboratories in Patiala, India, the current investigation's morphological examination was conducted with the assistance of a scanning electron microscope with the model number JSM 6510LV, which was made by JEOL in the Netherlands. Following is an explanation of the operating mechanism to determine electron microscope results.

- *Preparation of samples*

The silt sample was dried in the sunlight for the removal of the moisture and excess moisture if present is removed by placing the silt in the microwave oven (Sentwin Ltd. India). For SEM-EDS investigation, a sample that has been coated in gold is necessary to use the JEOL, JSM 6510LV scanning electron microscope. The gold coating was applied to the materials with the assistance of an auto fine coater made by JEOL in the Netherlands (Model: JFC-1600), which makes the conduction behaviour to insulated erodent particles easier. After that, they positioned the specimen into the sample holder, which was then installed within the SEM machine. **Figure 3.4** depicts the sample holders that are used inside the SEM machine.

- *Working Principle*

In the beginning, coated powder samples of a tiny amount are used (a few mg), and these samples are put in a sample holder, which is then mounted in a high vacuum chamber of the SEM machine (about 2 x 10^{-6} torr). To produce an electron beam with a diameter of less than 10 nanometers and acceleration voltage of 20 kilovolts, tungsten filament electron cannon is the tool of choice. When the electron beams produced by the tungsten filament impact the mounted sample, they cause a chain reaction those results in the generation of secondary electrons, X-rays, back-scattered electrons, diffused electrons, and other forms of electrons. The EDS spectrum may be measured using the X-rays that are generated by the sample. SEM micrographs may be made at a resolution of one nanometer or higher. In the current investigation, scanning electron micrographs were obtained at a range of magnification scales, including 100x, 300x, 500x, 1000x, and 2000x, depending on the level of representation that was required.

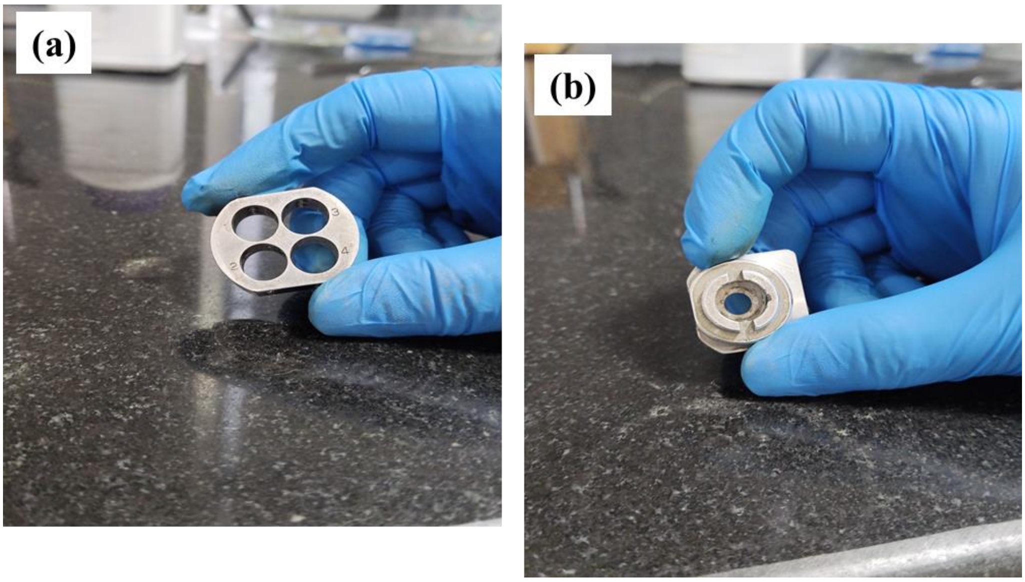

Figure 3.4. (a) Multiple sample holder, and (b) single sample holder for SEM of powdered samples.

- *Morphological results*

The multisized silt in the particle ranges of <53 µm, 53-106 µm, 150-212 µm, and 212-250 µm chosen for the morphological investigation. SEM image of silt particles is shown in **Figure 3.5(a-d)**. The different form of silt particles are found ranging from spherical to particles with angular edges according to SEM imaging.

3.2.2 Energy dispersive spectroscope (EDS)

The energy dispersive spectroscope (EDS), which was coupled with a scanning electron microscope (SEM) was used to analyse the samples to identify the chemical composition of the erodent, coated, and eroded samples. Energy-dispersive X-ray spectroscopy, or EDX for short, is another name for energy dispersive spectroscopy (EDS). In the current investigation, the EDS spectra were further used to carry out the mapping of various element distributions in coated samples. As discussed in the previous section, X-rays are generated when electron beams from a filament impact a material. An interaction takes place between the sample specimen and the X-rays. This interaction enables a unique set of peaks to appear on the electromagnetic (Em) emission spectrum from the sample. The elements that exist in the mounted sample are diverse from each other and each of those elements has its distinct atomic structure. An energy-dispersive spectrometer is used to quantify the energies released from the sample surface as a result of the interaction with X-rays. The variance in the energy generated by X-rays is used to determine elemental composition. Since the energy levels of many different elements are similar to one another, the accuracy of the EDS spectrum suffers due to the similarity in energy levels. The elemental composition found from the EDS analysis is shown in **Figure 3.5(e)**. In **Figure 3.5(e)**, the EDS spectrum reveals the presence of numerous elements in silt including Si, Al, O, Mg, K, Ca, Ti and Fe having percentages as 51.17, 1.65, 45.58, 0.37, 0.35, 0.36, 0.2 and 0.32% respectively.

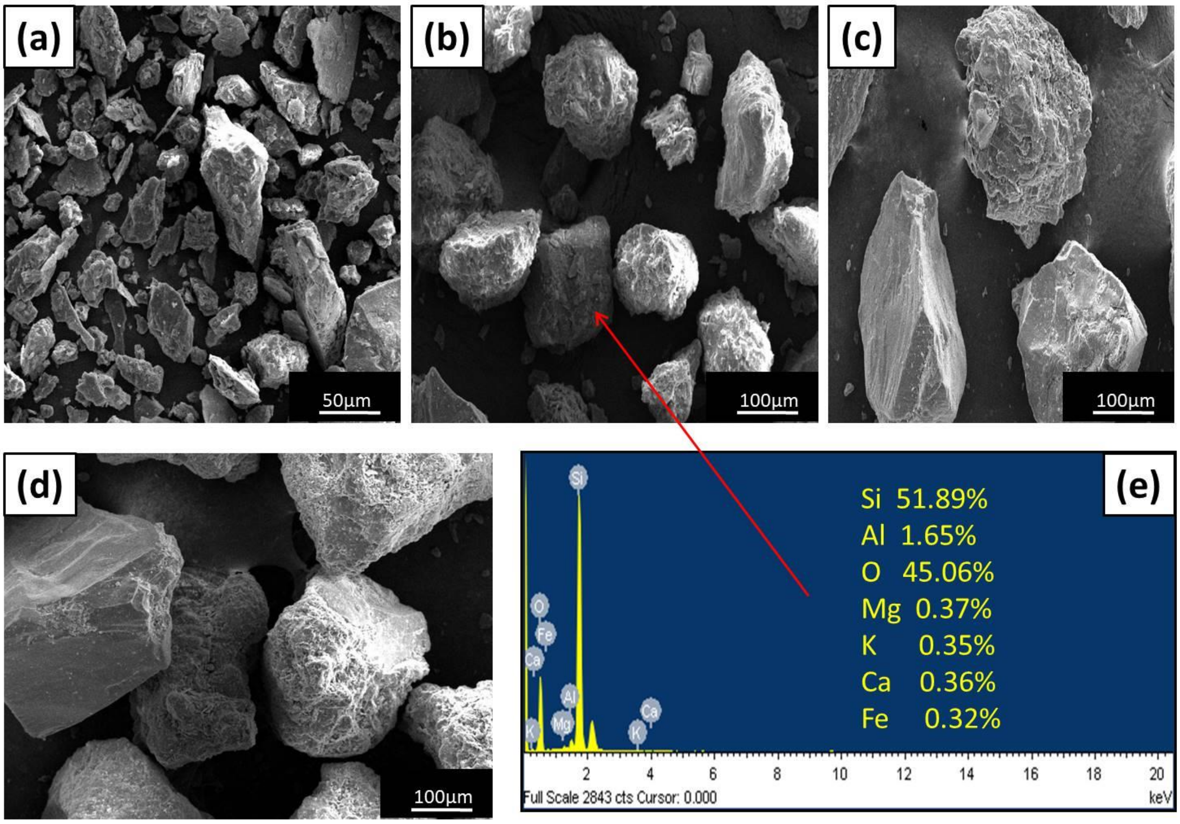

Figure 3.5. Silt SEM with particle sizes of (a) <53 µm (b) 53-106 µm (c) 150-212 µm (d) 212-250 µm, and (e) EDS of silt.

3.2.3 X-ray Diffractometry (XRD)

Silt samples and coatings were subjected to X-ray diffractometry (XRD) which is used to carry out the crystallographic analysis. X-ray diffraction is a well-established method for determining the nature of undiscovered crystalline solids and phases present in a variety of solid substances. In this work, X-ray diffractometry was utilized to detect the distinct crystalline phases of different compounds present in erodent materials as well as coated surfaces.

- *Preparation of samples for XRD*

The preparation of the samples is carried out inside a sample holder, as shown in **Figure 3.6**. Before beginning the process of sample preparation, the sample holder was subjected to an acetone bath to eliminate the presence of any contaminant. Afterwards, a powdered sample having a quantity of a few grams was placed in the cavity of the sample container. Then, a piece of glass was used to make the surface of the filled cavity on the sample holder as flat as possible. A square shape sample with a dimension of 2 × 2 cm and a thickness of 5 mm was developed for coated materials. In the end, the sample holder was fixed inside the XRD unit for the examination of the crystal structure.

Figure 3.6. Sample holder for XRD.

- *Working Principle*

An X-ray diffractometer is made up of many different components like an X-ray tube, a specimen container, a goniometer, and a detector. The X-ray tube is responsible for producing an electron beam at a high voltage. An angle of 'θ' is applied to the rotation of the specimen while it is held in the sample holder. The angle '2θ' represents the rotation of the X-ray detector. To determine the angle of rotation of the sample, a goniometer is used. The X-ray diffraction technique relies on the scientific method of diffractometry, which is based on Bragg's equation. According to this concept, when electron beams impact various materials, the electrons are diffracted, backscattered, or diffused depending on the nature of the material. On a detector that records the signal in terms of count rate, both the location and intensity of X-rays that have been diffracted may be monitored. In addition, the count rate may be utilised to determine whether or not distinct phases are present. The distance between crystals that was utilised to create the diffraction pattern (10–100 A°) is a representation of the wavelength of X-rays. In the current investigation, the X-ray diffraction patterns of coated surfaces and erodent materials were obtained with the assistance of a Philips X'Pert diffractometer with the model number PW 1710. It functioned at 40 kV and 30 mA while using Cu K radiation with a reference wavelength of 1.542 microns. In the current experiment, the value of theta (θ) was adjusted between 10 and 100 degrees.

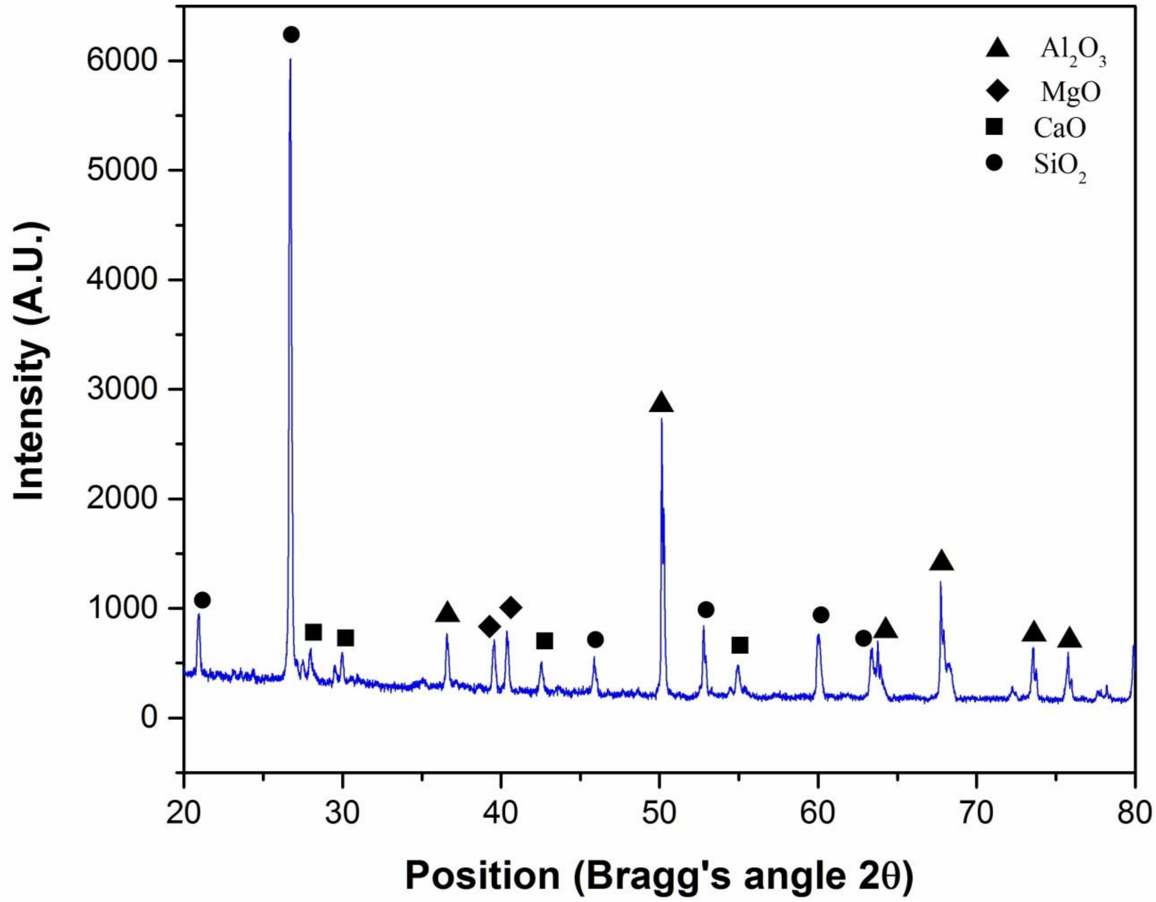

Figure 3.7. XRD pattern of silt sample.

- *XRD Results*

XRD pattern of silt particles is shown in **Figure 3.7**. Quartz (SiO_2) was detected in the highest concentrations. Periclase (MgO), quicklime (CaO), and alumina (Al_2O_3) are some more crystalline phases. Compounds of K and Fe were not seen as amount these elements are negligible in the EDS analysis. In the XRD spectrum, quartz $2\theta=26.72°$ generated the most intense peak, indicating the presence of quartz in substantial quantities. The XRD results are in good accord with those of previous studies (Grewal et al., 2013; Singh and Singh, 2021b).

3.3 BENCH SCALE TESTING

The pH value, particle size distribution, and bulk density of silt slurry were analysed using a variety of bench-scale tests. However, the coating characteristics such as roughness, micro hardness, and porosity were also tested through bench scale tests and standard procedures. The detail of these tests with instrument or standard is given as follows:

3.3.1 Particle size distribution

An examination using sieves was done so that the particle size distribution of silt particles could be determined. In this experiment, the particle size distribution was determined using a sieve shaker that was made by Mody Testing Instruments Co. in Vadodara, Gujarat, India. The sieve shaker was equipped with British standard sieves.

- *Procedure adopted for sieving*

An oven was used to dry the erodent material before the sieve test was performed. Throughout this procedure, the temperature of the sample was kept at an even and consistent level. After that, the sieves were adjusted such that various particle size ranges of the powdered samples could be obtained. In a column, the sieves are given their appropriate settings. The sieves were stacked such that the mesh size corresponding to the lowest BSS number was on the top and the mesh size corresponding to the highest BSS number was on the bottom. This order was determined by the British standard size (BSS) number. The circular pan at the bottom of these sieves is referred to as the receiver. The top sieve received 1 kg of powdered materials to be evaluated. After that, the sieve shaker was turned on and left running for fifteen to twenty minutes. After that, the weight that was kept in each of the various sieves was determined by using a CAY-220 electron weighing machine, which was produced in India by CAS Corporation and had the least count of 0.0001 g. The repeatability was taken into consideration by doing each test a total of four times to assure the precision of the data collected from the results. After doing the sieve analysis, the following particle size ranges were determined: <53, 53-106, 150-212, and 212-250 µm respectively. After the samples had been sieved, the information about the weights that were kept in each sieve was plotted between the particle size range and the percentages of the finer particles. The following equation was used to determine the proportion of finer particles:

$$\% \, finer = \frac{R_w}{T_W} \times 100 \tag{3.1}$$

Where R_W and T_W stand for the weight of the solid that was kept in the sieve and the total weight of the solid that passed through all of the sieves, respectively (in gms). The PSD of silt particles using standard British sieves is shown in **Figure 3.8**. From the results data of silt particles, it was observed that about 9.8% of particles lie in the range 53-75 µm, 11.52% silt particles are found finer than 106 µm, 52.3% particles were finer than 200 µm, and 20.5% particles were coarser than 250 µm.

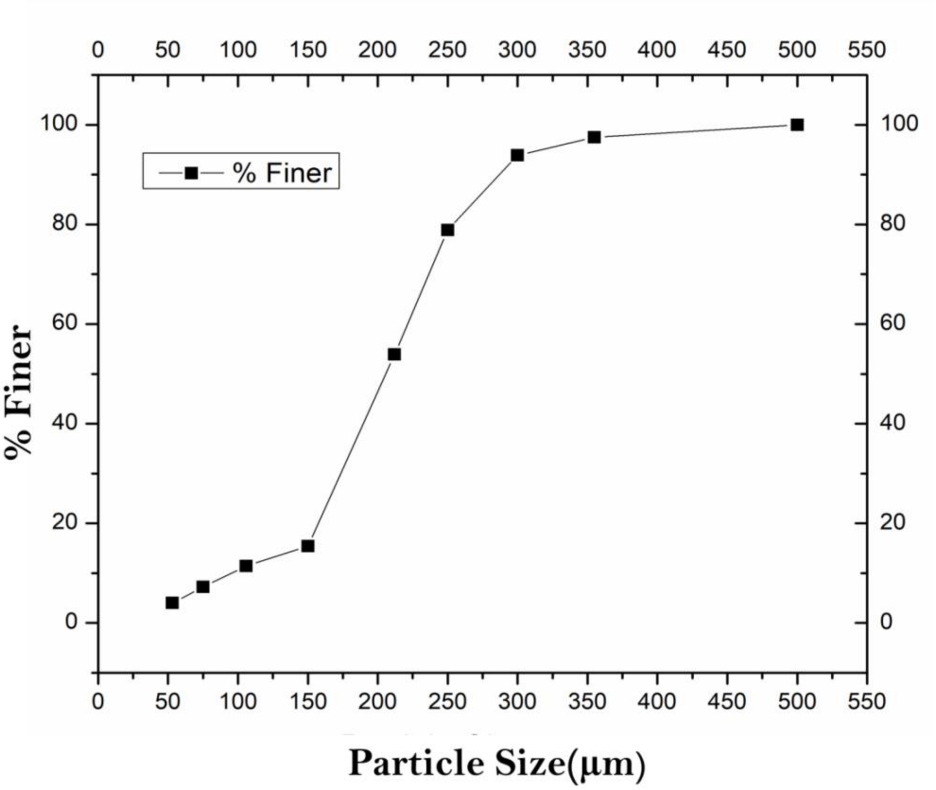

Figure 3.8. Particle size distribution of silt particles.

3.3.2 *Potential of hydrogen (pH value)*

The amount of hydrogen ions present in a liquid or solution is referred to as its pH value. This number is used as a term to characterize the chemical composition of the liquid or solution. The negative log of an aqueous solution's hydrogen ions is the value that is used to determine its pH. In general, the pH value of acids is lower than 7, while the pH value of alkalines (basics) is higher than 7. The pH level of a solution that is considered to be neutral, such as water, is always equal to zero. Using a digital pH metre is the most straight forward way to get an accurate reading. In the current study, a digital pH metre was used to determine the pH value of silt slurry suspensions at various solid concentrations. A glass electrode is connected to the pH metre that was made by Orino 5 Star and is sold under the brand name pH ISE Cond DO Benctop. To calibrate the electrode of the metre before beginning the analysis, the aqueous solution, which was distilled water, was used. After that, it was rinsed once again with distilled water, and then it was submerged in each of the three slurries so that the pH value could be determined. The pH of silt slurry was measured to fall somewhere in the range of 7.81-7.10. It was discovered that the silt slurry had an alkaline composition.

3.3.3 *Bulk density*

The ratio of the measured density of a material to the density of a reference substance is referred to as the substance's specific gravity or bulk density. The concept of 'density' refers to the amount of mass contained inside a certain volume. The following equation may be used to define specific gravity:

$$Bulk\ density = \frac{Density\ of\ slurry}{Density\ of\ water} \tag{3.2}$$

In the current investigation, the specific gravity of silt-water slurry was determined with the use of the pycnometer technique. To begin, a beaker with a capacity of 100 ml was filled with tap water and rinsed well. After that, it was placed in a microwave oven and remained there for an hour. After that, the beaker was placed on an electron weighing machine, which had a minimum count of 0.0001 gm. The reading on the machine was measured, and then it was reset to zero. After pouring the oven-dried sample (W_s) into the beaker, the weight of the sample was also determined. After the sample had been weighed, the slurry of the sample was created by combining it with distilled water and stirring it for anywhere from five to ten minutes to ensure that it was well combined. For the sake of subsequent measurement, the level of slurry in the beaker was indicated. After that, the weight of the slurry sample was measured once again after an hour, and the result was deducted from the weight that had been determined for the beaker to arrive at the accurate value for the weight of the slurry sample (W_{sw}). Following the completion of this procedure, the weight of water (W_w) was determined by refilling the same beaker to the level that had been previously indicated. The numbers that were measured were written down and then entered into the following correlation to compute the precise density of the slurry in question.

$$\mathit{Bulk\ density} = \frac{W_s}{(W_w - W_{sw}) + W_s} \tag{3.3}$$

By using this method, the bulk density of silt particles was calculated as 2.65.

3.4 REMARKS

The following remarks are noticed from the characterization of erodent:

- The surface of the silt particles has both imperfections and sharp edges can be seen.
- Silt particles have a high proportion of silica, which gives them a high micro hardness which means that they may contribute to the erosion of turbine material and coatings.
- Silt is composed of particles that are often larger in size. About 71.7% of particles lie in the range 75-250 µm, and 7.2% particles are below 75 µm.
- The pH of silt slurry was measured to fall somewhere in the range of 7.81-7.10.
- According to present study, silt particles have a bulk density of 2.65.

CHAPTER 4

SILT EROSION PERFORMANCE OF HYDROTURBINE MATERIAL AND COATINGS

In this chapter, the silt erosion of different hydro turbine material (SS-304) and ceramics coatings was analysed. SS-304 was taken as the base material for coatings. This chapter also covers the various analyses like elemental composition, surface microstructure, coating thickness, crystal structures, micro hardness, roughness, porosity, and other properties of coatings. The major part of this chapter covers development of coatings, characterization of coating powders and coatings, and silt erosion performance of SS-304 and coatings.

4.1 BASE MATERIAL AND SPECIMEN

The specimen SS-304 utilized in the erosion test was purchased from Jain Metal Industries, New Delhi (India). The erosion tests are performed on a specimen having dimensions (65 mm × 25 mm × 5 mm) that shown in **Figure 4.1**. The elemental composition of stainless steel is determined using an optical emission spectrometer (**Table 4.1**). A deep hole of 8 mm diameter has been drilled in the specimen's centre to accommodate the pot tester spindle through screw threaded bolt.

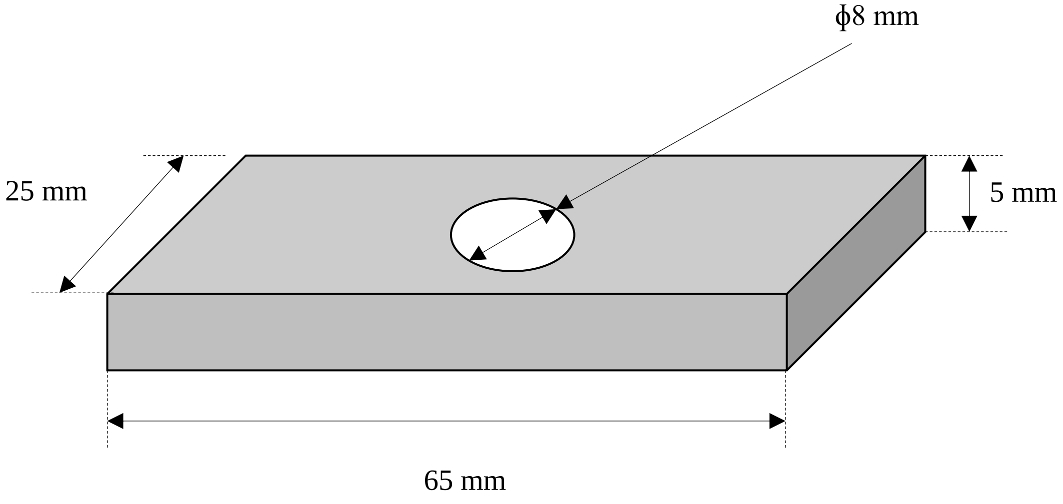

Figure 4.1. Geometry of the specimen.

Table 4.1. Elemental composition of SS-304 (wt. %).

C	P	S	Si	Cr	Mn	Ni	Fe
0.12	0.014	0.026	1.81	17.8	1.35	9.8	Balance

4.2 COATING POWDERS AND DEPOSITION

4.2.1 Detail of coating powders

The powders have a particle size range 5µm - 45 µm were purchased from Parshwamani Metals, Mumbai (India). The coating powders Al_2O_3, Cr_2O_3 and the 55% Cr_2O_3 +45% Al_2O_3 were applied to the SS-304 specimens by using the high-velocity oxy-fuel (HVOF) process for improving the erosion wear resistance. **Figure 4.2(a, b)** shows the SEM and EDS images of the Al_2O_3 and Cr_2O_3 coating powders.

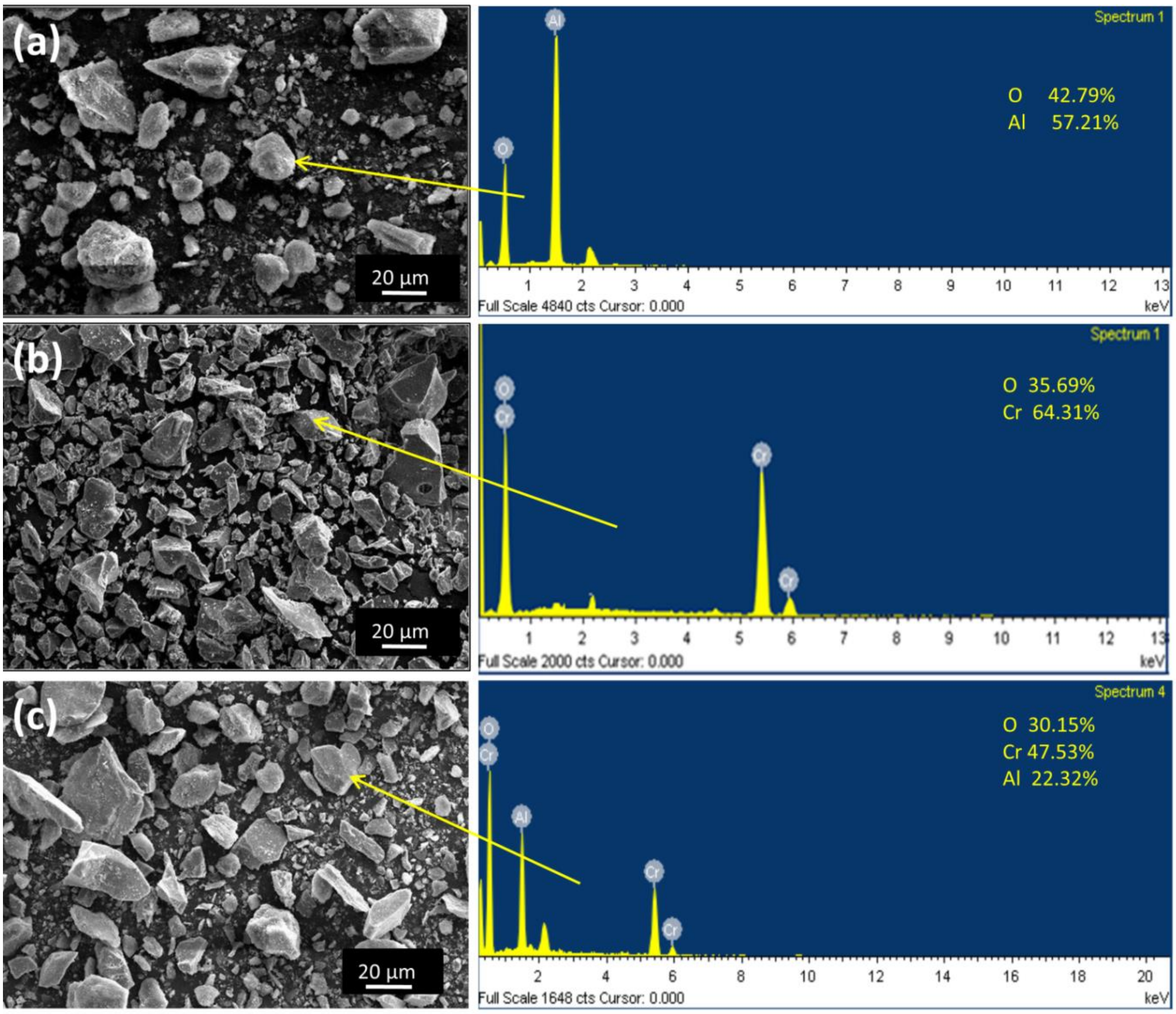

Figure 4.2. SEM and EDS Images of (a) Al_2O_3 (b) Cr_2O_3 (c) 55% Cr_2O_3+45% Al_2O_3 powders.

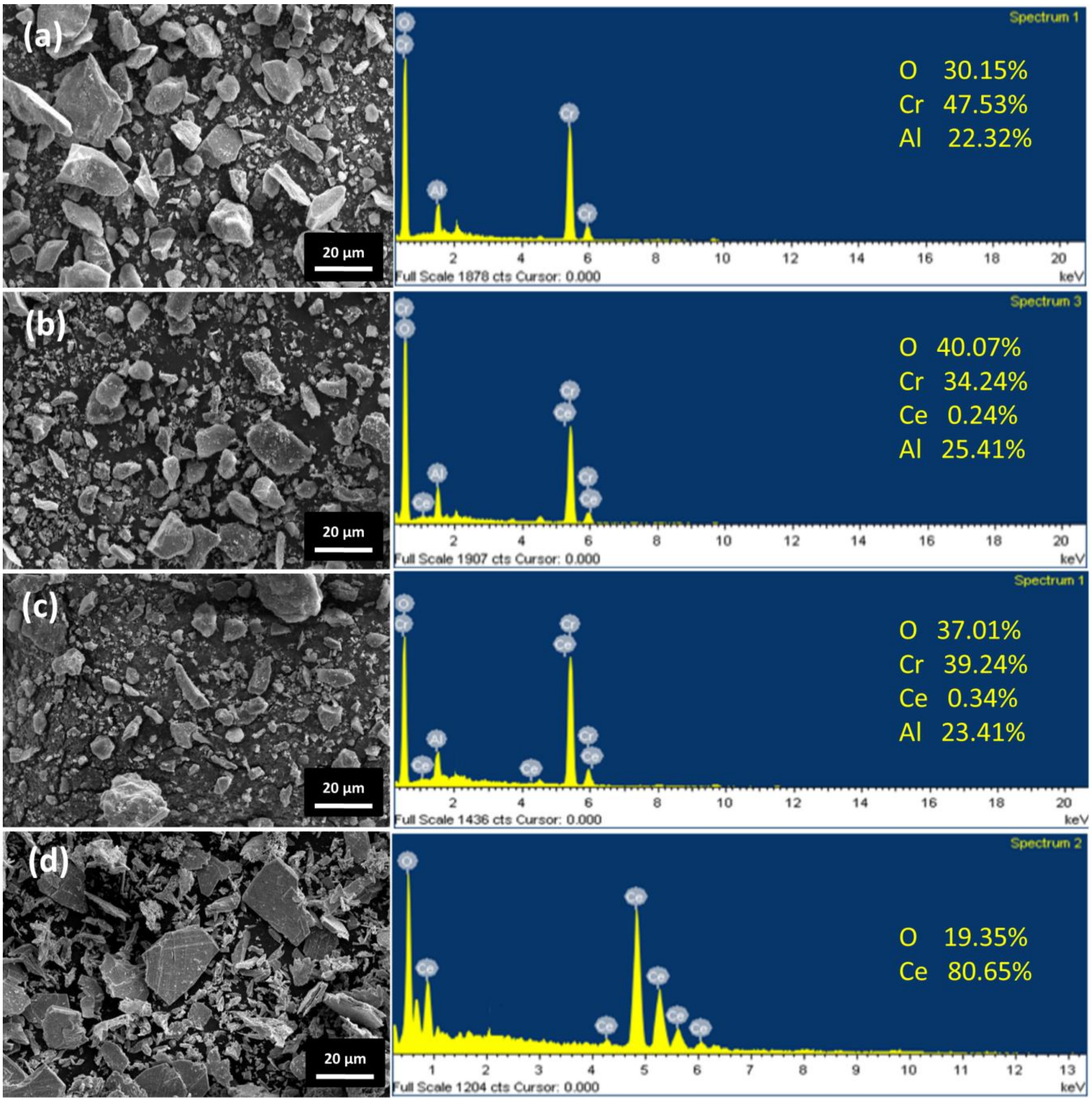

Figure 4.3. SEM and EDS Images of (a) 65%Cr_2O_3+35%Al_2O_3, (b) 65%Cr_2O_3+34.5%Al_2O_3+0.5%CeO_2, (c) 65%Cr_2O_3+34%Al_2O_3+1%CeO_2, and (d) CeO_2 coatings.

4.2.2 Blending of coating powders

Before coating deposition, the coating powders were blended with the help of ball milling process. For 55% Cr_2O_3 +45% Al_2O_3 coating powder, the requisite weight percentages of powders are mixed and put into the container with the ball bearings of different diameters. The container having the powder and the ball bearings have been rotated on lathe machine for a time period of nearly 100 hours for proper blending of coating powders. **Figure 4.2(c)** shows the SEM and EDS images of the blended 55% Cr_2O_3 +45% Al_2O_3 coating powder. The SEM image for Al_2O_3 as in **Figure 4.2(a)** shows the powder was found to have mixed ellipsoid and cubical particles. The EDS spectrum shows the percentage of O and Al as 42.79% and 57.21%. **Figure 4.2(b)** shows particles are mostly angular and elongated for Cr_2O_3 powder according to SEM image and the EDS shows the presence of O and Cr in the proportions of 35.69% and 64.31% while the EDS of composite coating depicts Cr, Al and O having percentage as 47.53%, 22.32%, and 30.15% by weight respectively, as shown in **Figure 4.2(c)**. The SEM and EDS images of 65%Cr_2O_3+35%Al_2O_3, 65%Cr_2O_3+34.5%Al_2O_3+0.5%CeO_2, 65%Cr_2O_3+34%Al_2O_3+1%CeO_2, and CeO_2 coatings powders are shown in **Figure 4.3**.

Table 4.2: Parameters of the HVOF process.

Spraying Constituents	**Spraying Distance (mm)**	**Powder supply rate (g/min)**	**Flow Rate (SLPM/min)**	**Pressure (kg/cm^2)**
Air	---	---	655	5.2
Oxygen	152	37	265	9.3
Fuel	---	---	70	7.2

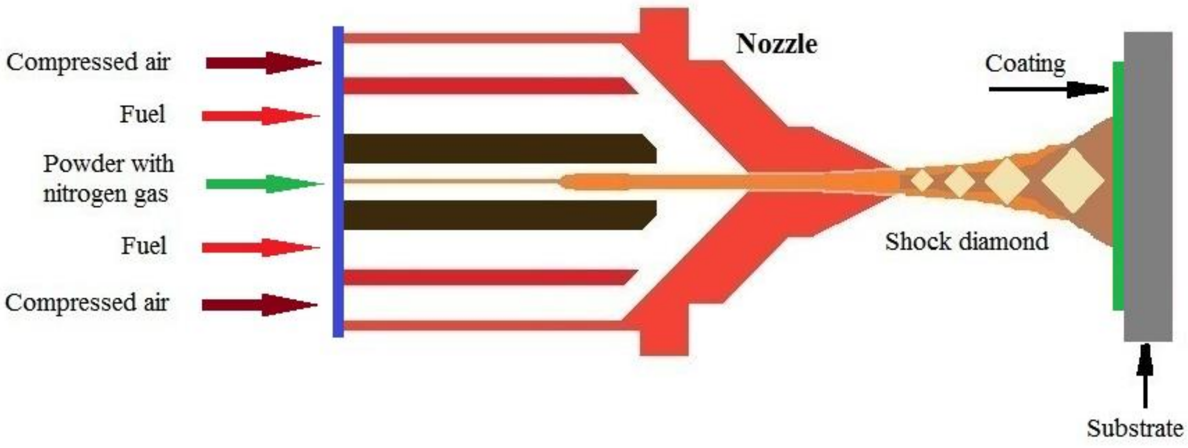

Figure 4.4. Schematic diagram of HVOF coating deposition process.

4.2.3 *Coating process*

The coating process employed for deposition of the requisite powders on the substrate material is HVOF. The thermal spray torch HIPOJET 2700 was accessible at M/s Harsha Weldings Panchkula, India was used for depositing the requisite coatings on the substrate. The test specimens were firstly sand blasted with a view to boom the roughness of the surface in order that right coating is adhered. The schematic of HVOF coating deposition process is shown in **Figure 4.4**. The flame temperature for the HVOF process is around 3000ºC which is quite very high temperature and is sufficient for ceramics. The parameters used during coatings are listed in **Table 4.2**.

4.3 EROSION TESTER AND TESTING PROCEDURE

The silt slurry erosion testing is done by using the pot tester for evaluating resistance for the coated and uncoated samples to silt slurry erosion. Ducom Instruments, Bangalore manufactured test rig was utilized to conduct the silt slurry erosion experiments. The actual picture of the pot tester used in the present study is shown in **Figure 4.5**.

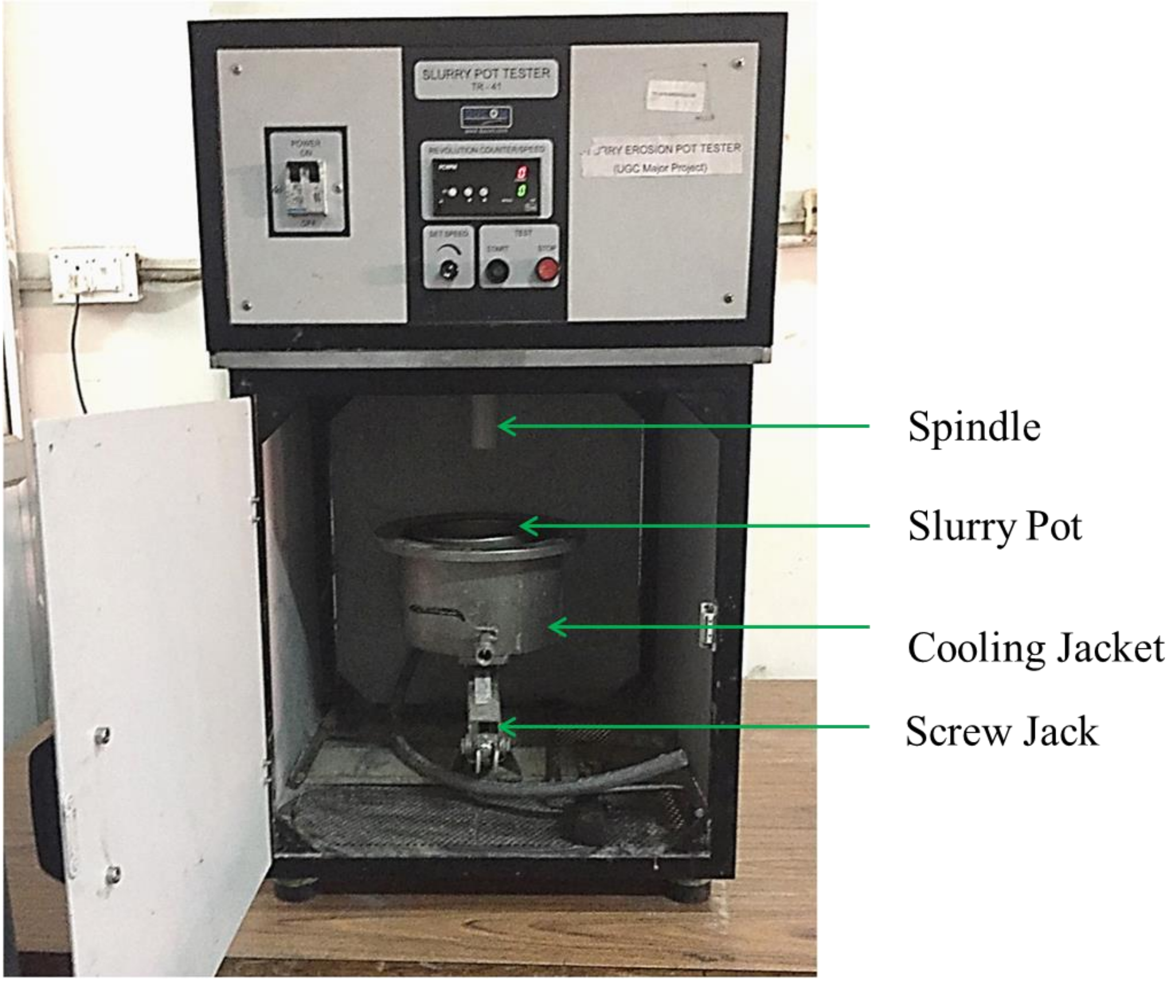

Figure 4.5. Actual picture of slurry pot tester used in the present study.

4.3.1 Construction of pot tester

Figure 4.6 presents the various sub-assemblies of the pot tester. It has a cube shell with two cylindrical metallic pot-shaped beakers of varying diameters in between. The small diameter cylindrical pot is used for preparing the slurry. The dimensions of the pot are 118×118 mm^2. The screw jack can be used to adjust the height of the pot so that the specimen is entirely immersed in the slurry. At the top inside of the chamber is a cylindrical screw-threaded spindle which is used for supporting the requisite work piece for experimentation with the help of the screw bolt impeller to tighten the work piece to the spindle. A knob is provided for changing the spindle speed to the maximum value of 1500 rev/min. Above the knob are also provided with the two digital meters which display the rotational speed and the rotation counter of the specimen.

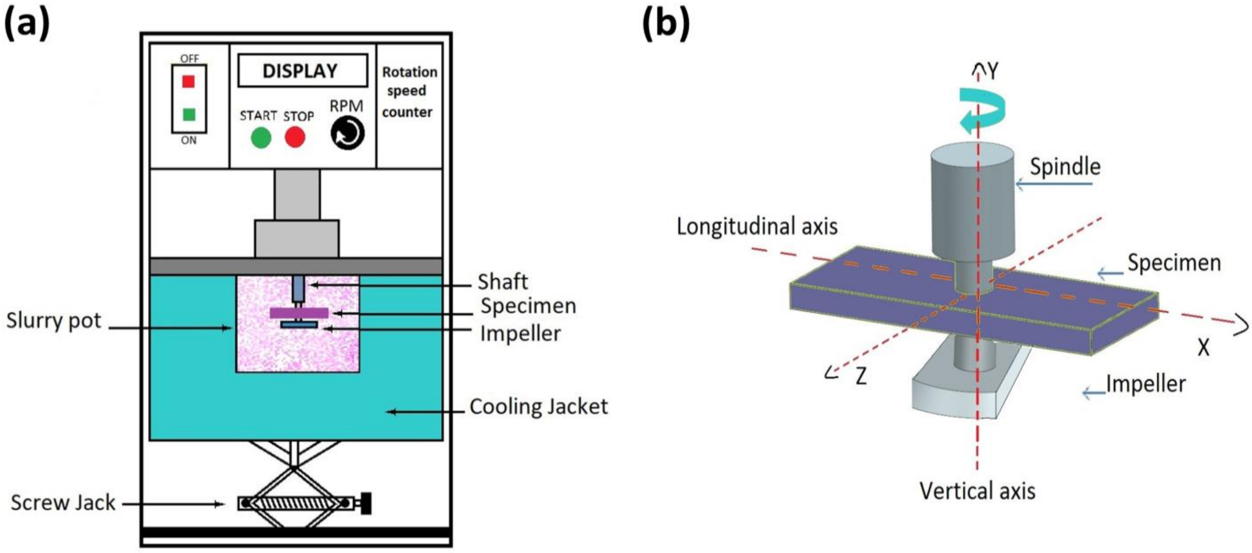

Figure 4.6. (a) Schematic diagram of slurry pot tester, and (b) specimen fixture.

4.3.2 Experimental procedure

The slurry pot device involves the test specimens clamped through the impeller and rotated at desired speed inside a pot type arrangement filled with medium of silt slurry. The slurry is composed of tap water and particular mesh size of silt of known standard concentration. The rotation of test specimens inside the slurry medium produces a relative motion between silt slurry complex and specimens. The collision of the silt particles in the slurry causes the erosion of specimens. The specimen, bare as well as coated which are used for conducting the studies are first weighed using a CAY 220 electronic weight balance (South Korea) having least count of 0.001 g. For performing slurry erosion testing, samples were cleaned in acetone and then dried so that whole of the moisture get eliminated. Thereafter the test rig is then made to run for total time span of four hours. Weight measurements were done every one hour by using the measuring weight balance so as to monitor the weight loss of the specimen as a result of the impingement of the solid silt particles on the specimen which is a measure of erosion wear which has taken place in the specimen. The erosion experiments were accomplished out on the bare SS-304 and HVOF coated substrate specimens using a pot tester at a particular rotating speed, silt concentration, different particle sizes and for a specific time length in four trails. Slurry erosion tests are used to calculate the change in mass of the specimen that occurs as a result of the specimen being impinged by the slurry during the testing. After obtaining the experimental data, several graphs involving erosion wear versus diverse operating testing parameters as time duration, rotational speed, concentration and particle size.

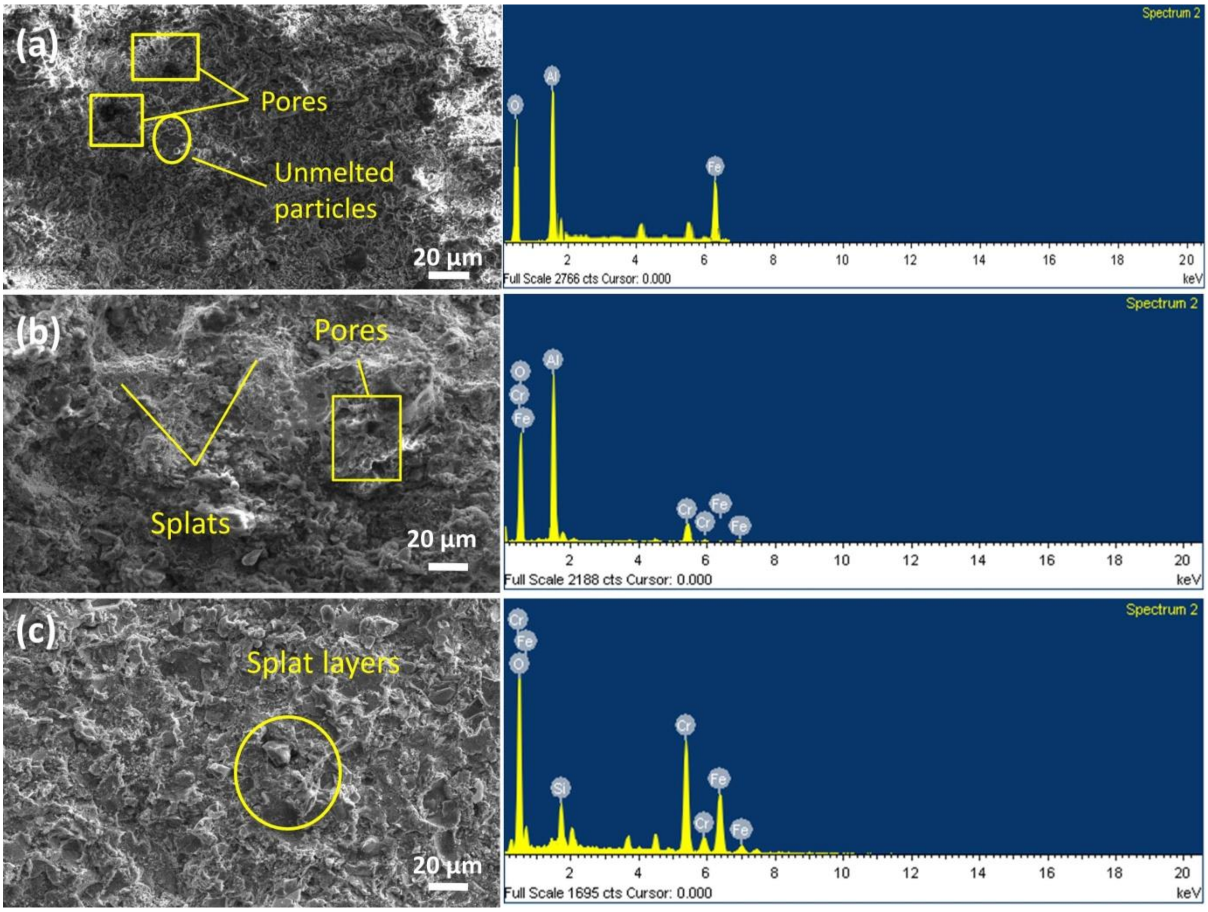

Figure 4.7. SEM and EDS images of as sprayed coated samples (a) Al_2O_3, (b) 55% Cr_2O_3 + 45% Al_2O_3, and (c) Cr_2O_3.

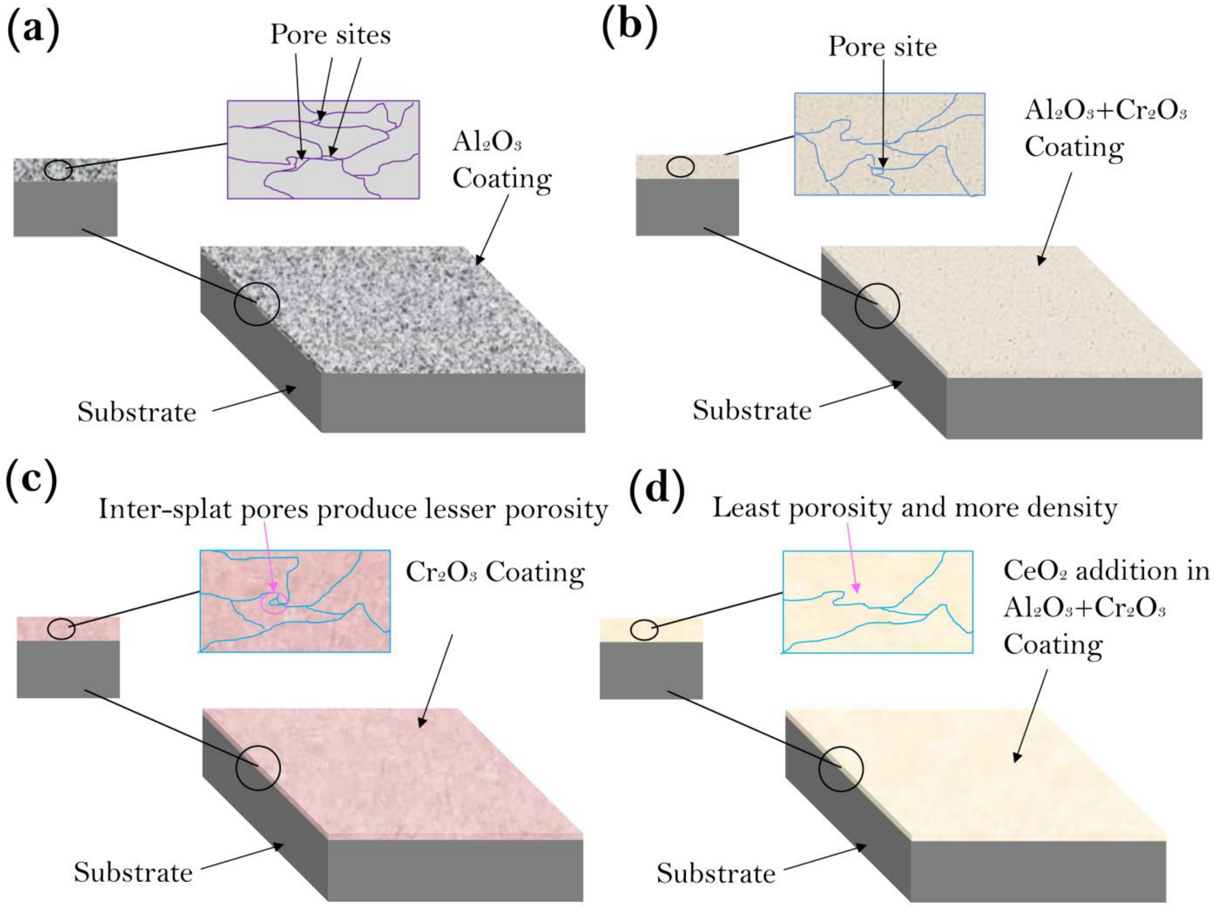

Figure 4.8. Schematic diagram of porosity in (a) Al_2O_3, (b) $Cr_2O_3+Al_2O_3$ coatings, (c) Cr_2O_3, and (d) effect of 0.5% CeO_2 reinforcement in $Cr_2O_3+Al_2O_3$ coatings.

4.4 PRE-EXPERIMENTAL ANALYSIS

4.4.1 Microstructural analysis

The microstructure analysis of the coated samples before and after erosion testing has been done by using the Scanning Electron Microscopy (SEM). The instrument is Netherlands made (JEOL) of model JSM-6510L. The surface morphology of the coated samples and the coated eroded samples has been studied by the SEM analysis. **Figure 4.7** shows the SEM micrographs of Al_2O_3, 55% Cr_2O_3 + 45% Al_2O_3 and Cr_2O_3 deposited coatings. As shown in **Figure 4.7(a)**, more of the pores and the unmelted loosely bonded particles were appeared in the coating. **Figure 4.7(b)** indicates the presence of some pores as well as splatted layers of 55% Cr_2O_3+45% Al_2O_3 composite coating. **Figure 4.7(c)** shows the dense splat layers in Cr_2O_3 coating. The eroded coated samples have also been analysed through SEM micrographs. A schematic diagram of porosity of coatings is shown in **Figure 4.8**. In case of Al_2O_3, the more pores is present which can contribute in erosion (**Figure 4.8a**). However, the porosity of 55% Cr_2O_3 + 45% Al_2O_3 composite coating was found lesser than Al_2O_3 coating due to the densification which contributes in lesser pores (**Figure 4.8c**). As shown in **Figure 4.8(c)**, the Cr_2O_3 coating possesses porosity in inter-splat region which is also observed in SEM image. The as-sprayed and eroded samples were examined micro structurally using a SEM. The SEM micrographs of different as-sprayed coatings have been shown in **Figure 4.9**. The deposited coatings show the presence of semi-melted particles on the surface. The semi-melted particles can be seen on the surface due to the rapid cooling by atmospheric air. Al-Fadhli et al. (2006) reported that the semi-melted particles were present because of the high cooling rate of splats or sometime due to non-uniformity of powder manufactured. This air pressure also results in the smoother regions. The addition of 1.5%, 1% and 0.5% CeO_2 resulted in the more reduction in porosity and matrix densification respectively, as shown in **Figure 4.8(d)**.

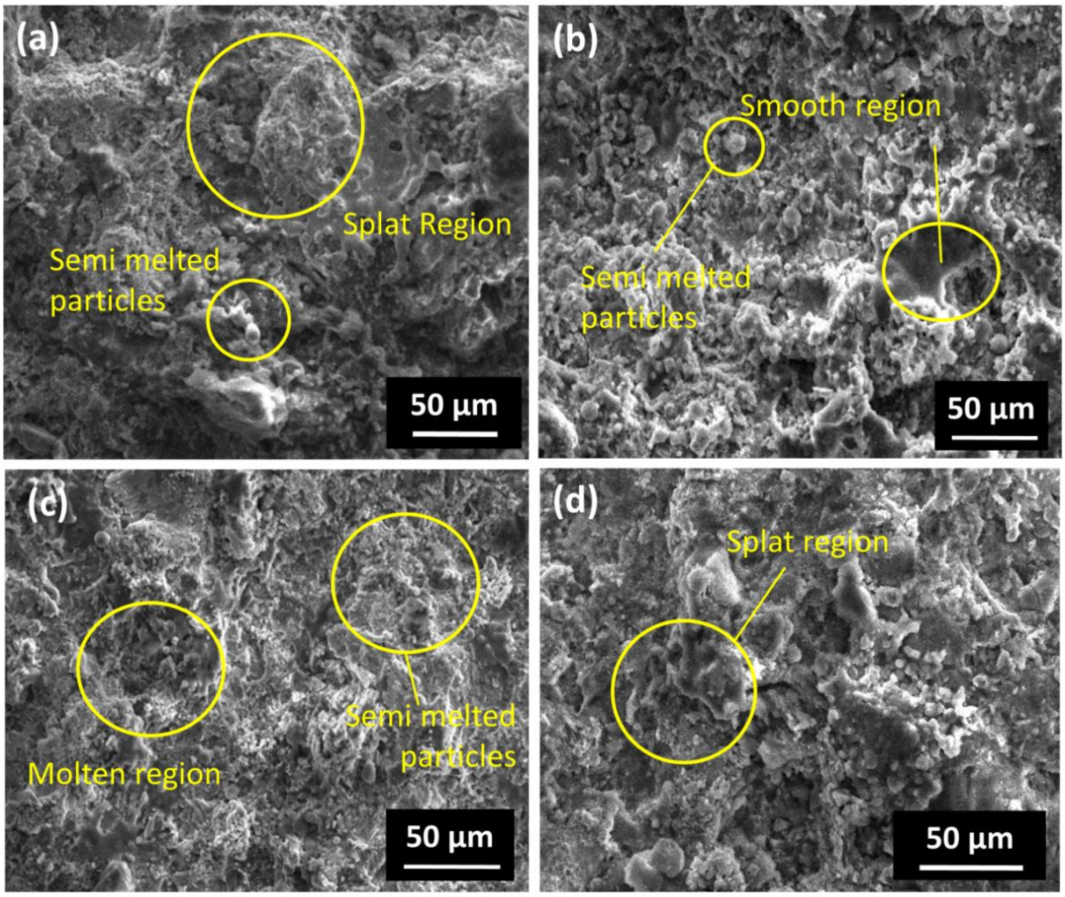

Figure 4.9. SEM micrographs of as sprayed (a) 65% Cr_2O_3+35% Al_2O_3, (b) 65% Cr_2O_3+34.5% Al_2O_3+0.5% CeO_2, (c) 65% Cr_2O_3+34% Al_2O_3+1% CeO_2, and (d) 65% Cr_2O_3+33.5% Al_2O_3+1.5% CeO_2 coatings.

Table 4.3: Average hardness, porosity and roughness values of investigated specimens.

S. No.	Coatings	Average hardness ±6%	Porosity	Average roughness
1	SS-304	284.29 HV	0	0.43 µm
2	Cr_2O_3	1190 HV	1.29%	5.84 µm
3	Al_2O_3	970 HV	3.28%	6.92 µm
4	55% Cr_2O_3 + 45% Al_2O_3	1005 HV	2.44%	4.55 µm
5	65%Cr_2O_3+35%Al_2O_3	1030 HV	2.20%	2.73 µm
6	65%Cr_2O_3+34.5%Al_2O_3+0.5%CeO_2	1140 HV	1.35%	1.65 µm
7	65%Cr_2O_3+34%Al_2O_3+1%CeO_2	1080 HV	1.75%	2.50 µm
8	65%Cr_2O_3+34%Al_2O_3+1.5%CeO_2	1045 HV	2.65%	3.13 µm

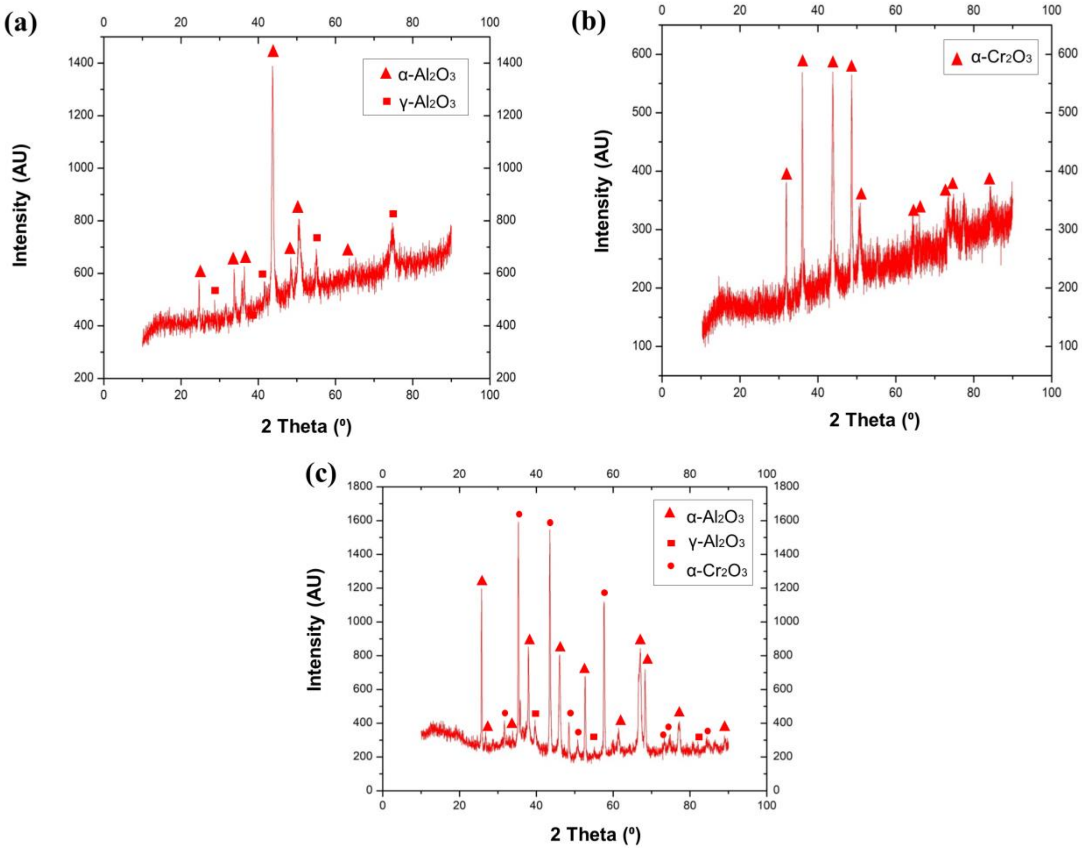

Figure 4.10. XRD patterns of (a) Al_2O_3, (b) Cr_2O_3, and (c) 55% Cr_2O_3 + 45% Al_2O_3 HVOF coatings.

4.4.2 XRD analysis

The phase compositions of the as sprayed HVOF coatings were identified by X-Ray diffraction. The XRD pattern analyses were executed in the 2θ range from 10º to 90º. By analysing the intensities of the greatest diffraction peaks for Al_2O_3 HVOF coating as depicted in **Figure 4.10(a)**, mostly γ-Al_2O_3 and α- Al_2O_3 phases are present. For the Cr_2O_3 coating in **Figure 4.10(b)**, mostly α-Cr_2O_3 phase is visible and having maximum peak (2θ) observed at nearly 43.7º. Also in the XRD spectrum of 55%Cr_2O_3+45%Al_2O_3 HVOF coating, the γ-Al_2O_3 and α-Al_2O_3 phases were appeared, as shown in **Figure 4.10(c)**. As, it is also evident from the measured porosities values of coatings it signifies that the addition of Cr_2O_3 is conducive to the densification of coating which can be attributed to phase interface strengthening and so responsible for more erosion resistance as compared to Al_2O_3 coating. Also, the XRD was carried to examine the various phases formed during the HVOF spraying of 0.5% and 1% added CeO_2 to the composite Cr_2O_3+Al_2O_3 as shown in **Figure 4.11**. The spectra show the presence of α-Al_2O_3, γ-Al_2O_3, α-Cr_2O_3, CeO_2, and Al-CeO_2 phases in both 0.5% and 1% added CeO_2 in Cr_2O_3+Al_2O_3 coating.

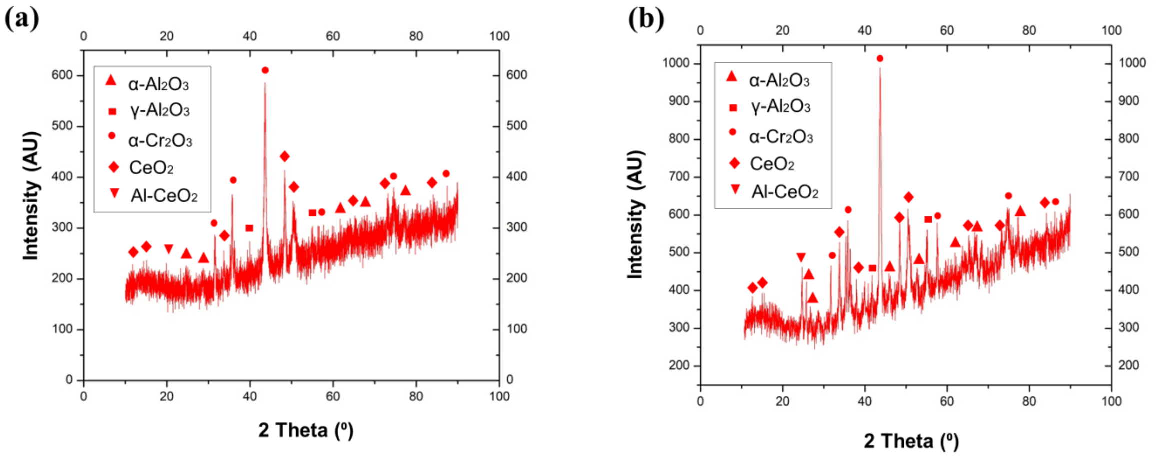

Figure 4.11. XRD patterns of (a) 65%Cr_2O_3+34.5%Al_2O_3+0.5%CeO_2, and (b) 65%Cr_2O_3+34%Al_2O_3+1%CeO_2 HVOF coatings.

4.4.3 Microhardness testing

After deposition of HVOF coatings, coated samples are also analysed for the Vickers microhardness, porosity and surface roughness values which are shown in **Table 4.3**. An MVH-1 digital micro hardness tester made by Metatech Pune, India was utilized for measuring the microhardness of coated and uncoated samples. During the testing, the 1000 g load was applied for a dwell time of 20 sec. In four trials, the average Micro hardness of SS-

304 was measured as 284 HV. The microhardness values of SS-304 sprayed HVOF coatings indicate a substantial increase, with the greatest value observed for the Cr_2O_3 coating. After reinforcement with 0.5% CeO_2, the SS-304 sprayed HVOF coatings show a significant increase in the values of micro hardness having the maximum value. The similar type of results of ceria incorporation has showed increase in hardness for flame sprayed Nickel based coatings which is attributed to refinement in the grain structure by the addition of ceria (Sharma et al., 2008).

4.4.4 Porosity testing

The porosities of the coatings were measured using image processing using an Image Analyzer ASPM V276 software package. This software works on the principle of grid method. It divides the area into the grid and marks the pores as red spots. Afterwards, the area of red spots was calculated for measurement of porosity (%). The image is calibrated first by using the scale bar of the SEM image. Afterwards, the threshold value is adjusted to make visible the pored region. Then the area of the pored region is calculated by measuring the perimeter of all pores. Typical image processed porosity images of conventional coatings are shown in **Figure 4.12**. The lowest porosity value has been observed for Cr_2O_3 coating amongst all the coatings. **Figure 4.13** shows image processed porosity images of CeO_2 reinforced coatings. From **Figure 4.13**, it was also observed that the coating with 0.5% CeO_2 inclusion had the lowest porosity value.

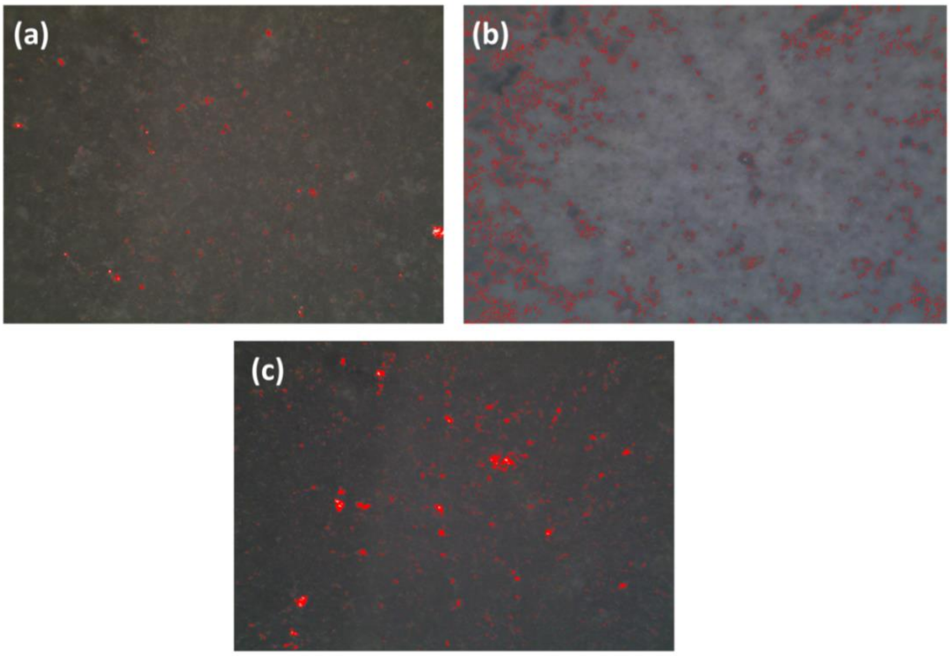

Figure 4.12. Porosity of (a) Cr_2O_3, (b) Al_2O_3, and (c) 55% Cr_2O_3 + 45% Al_2O_3 coatings.

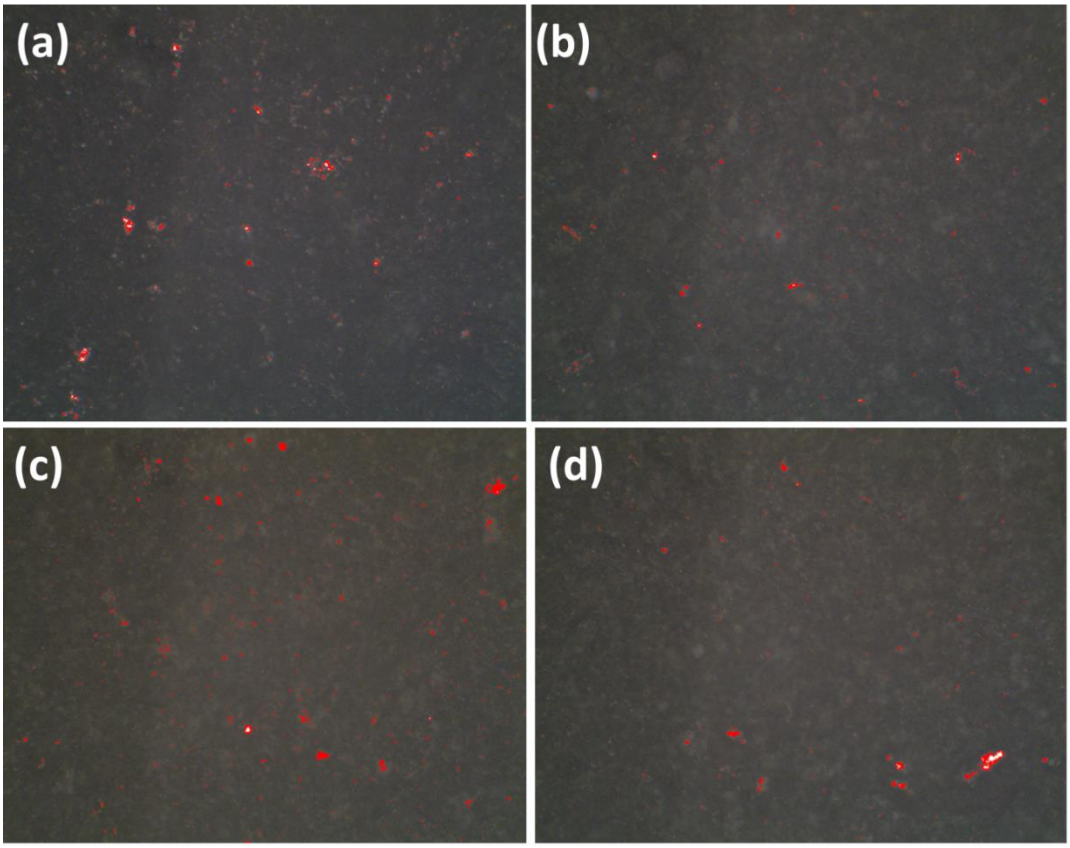

Figure 4.13. Porosity of (a) $65\%Cr_2O_3+35\%Al_2O_3$, (b) $65\%Cr_2O_3+34.5\%Al_2O_3+0.5\%CeO_2$, (c) $65\%Cr_2O_3+34\%Al_2O_3+1\%CeO_2$, and (d) $65\%Cr_2O_3+34\%Al_2O_3+1.5\%CeO_2$ coatings.

4.4.5 Roughness testing

The average roughness of the HVOF-coated surface was measured using an SJ-400 surface test roughness tester of make Mitutoyo (USA). The roughness testing was also done in four trials. The surface roughness values of coatings are summarized in **Table 4.3**. The typical roughness plots of conventional coatings for a testing length of 4 mm are shown in **Figure 4.14(a)**. Among the conventional coatings, Al_2O_3 coating has higher value of roughness. Also, the coating of composition with the addition of 0.5% CeO_2 has least value of roughness amongst all the CeO_2 reinforced coatings. The maximum value of roughness has been analysed for coating of composition 1.5% CeO_2 addition to the $Al_2O_3+Cr_2O_3$ coating, as observed from **Figure 4.14(b)**.

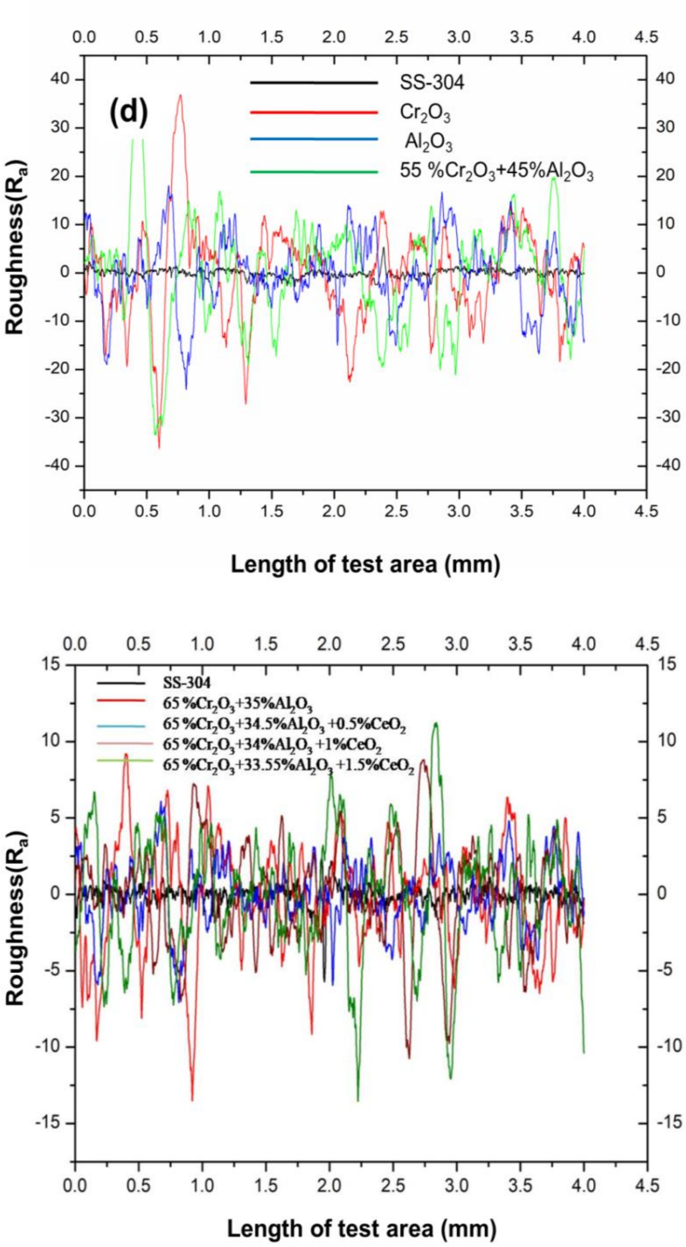

Figure 4.14. Roughness profiles of SS-304 and coatings.

4.5 PART I: SILT EROSION PERFORMANCE OF CONVENTIONAL COATINGS

4.5.1 Influence of time duration

The silt erosion testing conditions and parameters for analysing the time duration effects has been shown in **Table 4.4** and the findings of the silt slurry erosion experiment were produced in graphical form by using the different silt sizes in the range 212-250 µm, 150-212 µm, 106-53 µm and <53 µm while maintaining speed at 1500 rev/min and silt concentration as 30%. The erosion wear and commutative erosion wear curves are drawn using the average weight loss of four samples coated and untreated subject to a 4 hours slurry erosion testing.

Table 4.4. Silt slurry erosion testing parameters.

S. No.	Silt Erodent size	212-250 μm	150-212 μm	106-53 μm	<53 μm
1	Concentration (wt.%)	30	30	30	30
2	Rotational speed (rev/min)	1500	1500	1500	1500
3	Time (hours)	4	4	4	4

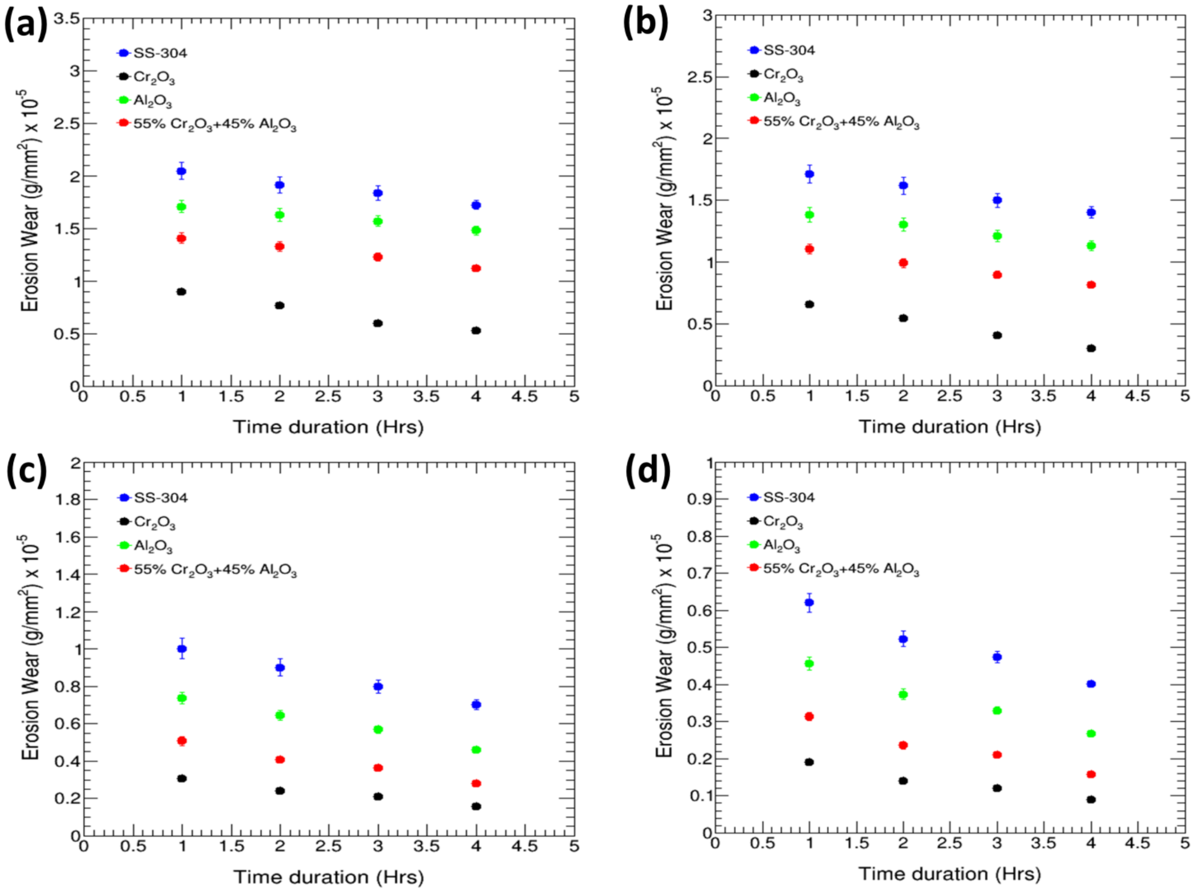

Figure 4.15. Silt erosion graphs as a behaviour of time for uncoated and HVOF sprayed Al_2O_3, Cr_2O_3 and 55% Cr_2O_3 + 45% Al_2O_3 coated SS-304 substrates at rotational speed 1500 rev/min and 30% silt concentration (a) 212-250 μm (b) 150-212 μm (c) 53-106 μm particle size (d) <53 μm.

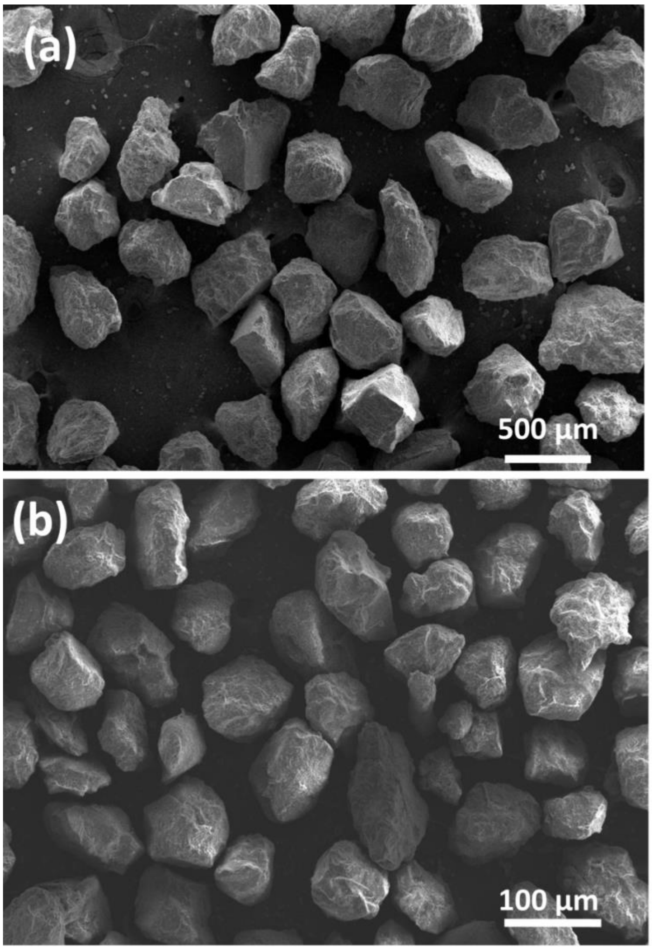

Figure 4.16. SEM morphology of silt (a) before erosion and (b) after erosion.

Figure 4.15(a) exhibits the erosion wear of HVOF sprayed coatings and bare SS-304 at particle size of 212-250 µm, rotational speed of 1500 rev/min and silt concentration as 30% for the test duration of 4 hours. In the current examination, the erosion wear is measured as relative weight loss of sample and is expressed in (g) per unit area (mm^2). It has been examined that the erosion wear is greater in the first hour and consequently gets decreased for the second, third and fourth hour. The erosion wear for the first hour for Cr_2O_3 coating is 0.9×10^{-5} g/mm^2 which gets decreased to the value of 0.53×10^{-5} g/mm^2 for the fourth hour. For the uncoated SS-304 the maximum and the minimum value for erosion wear has been examined as 2.046×10^{-5} g/mm^2 and 1.725×10^{-5} g/mm^2 for the first and the fourth hour. This occurred because the erosion wear process alters particle characteristics (Kishor et al., 2018) and may be attributed to loss of angularity of silt erodent particles due to repeated impact as shown in **Figure 4.16** and in accordance with investigators findings (Thakur and Arora, 2013). Among all the coatings the Al_2O_3 has shown the minimum resistance to wear with the erosion wear values as 1.71×10^{-5} g/mm^2 and 1.48×10^{-5} g/mm^2 for the first and the fourth hour. The maximum and the least erosion wear values for the coating of composition 55% Cr_2O_3 + 45% Al_2O_3 has been examined as 1.408×10^{-5} g/mm^2 and 1.122×10^{-5} g/mm^2 for the first and the fourth hour. The erosion wear of specimens by using the particle size of silt in the ranges of 150-212 µm, 53-106 µm, and <53 µm for all coatings and bare SS-304 follows a similar pattern for the time duration effects. The trend of erosion versus time curves is consistent with previous studies (Singh et al., 2020; Singh, 2021a, 2021b, 2021c; Singh et al., 2019b, 2019c; Singh and Singh, 2021a).

Figures 4.17(a-c) shows the commutative erosion wear as a function of time for all coatings and uncoated steel. The commutative values are obtained by adding value of erosion wear to its predecessor value. The erosion curves in **Figures 4.17(a-c)** show that commutative erosion wear has grown over time, which can be accredited to the repeated impingement of silt particles on the specimen's surface. The similar types of observations were observed by the investigators (Gupta et al., 1995; Singh et al., 2021a, 2021b; Singh and Singh, 2021b). Among all the coatings Cr_2O_3 coating has exhibited the least weight loss measurements and has the highest erosion resistance when compared to a composite composition 55% Cr_2O_3 + 45% Al_2O_3 and Al_2O_3 coating at all the particle size in the range of 212-250 µm, 150-212 µm, 53-106 µm, <53 µm at rotational speed of 1500 rev/min and at 30% silt concentration. All the coatings outperformed SS-304 in all of the testing parameters and showed an improvement in silt slurry erosion behaviour for erosion wear. It was also seen that the particles lose their angular edges after the erosion process, as seen in **Figure 4.16**.

4.5.2 Influence of rotational speed

Figure 4.18 shows the response of rotational speed on erosion wear of requisite samples with a particle range of 212-250 µm and a silt concentration of 30% for up to 4 hours. The relative weight loss from the sample for the erosion wear measurement is expressed in weight loss (g) per unit area (mm^2). Erosion wear was found to escalate with increasing rotational speed. The increment in the rotational speed is accompanied by the escalation in collision efficiency and higher inertia which gets imparted to the specimen so responsible for high wear (Clark, 1993, 1991). Erosion wear as observed for rotational speed at values of 600, 900, 1200 and 1500 rev/min for which peak erosion was observed at value of 1500 rev/min. It has also been noticed that the dominant erosion wear is observed for bare SS-304 to the value of 7.487×10^{-5} g/mm^2 and the minimum erosion wear is observed for Cr_2O_3 coating having value as 2.735 $\times10^{-5}$ g/mm^2.

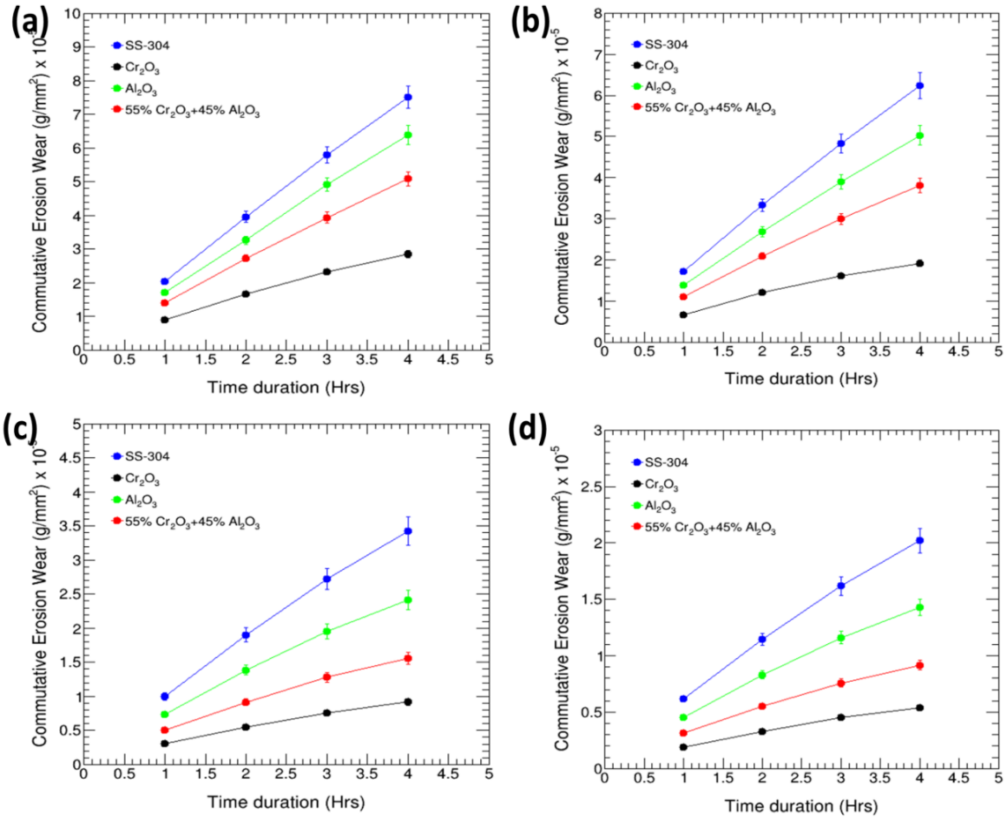

Figure 4.17. Commutative erosion wear curves as a function of time for uncoated and HVOF sprayed Al_2O_3, Cr_2O_3 and 55% Cr_2O_3 + 45% Al_2O_3 coated SS-304 substrates at rotational speed 1500 rev/min and 30% silt concentration (a) 212-250 µm, (b) 150-212 µm, (c) 53-106 µm, and (d) <53 µm particle size.

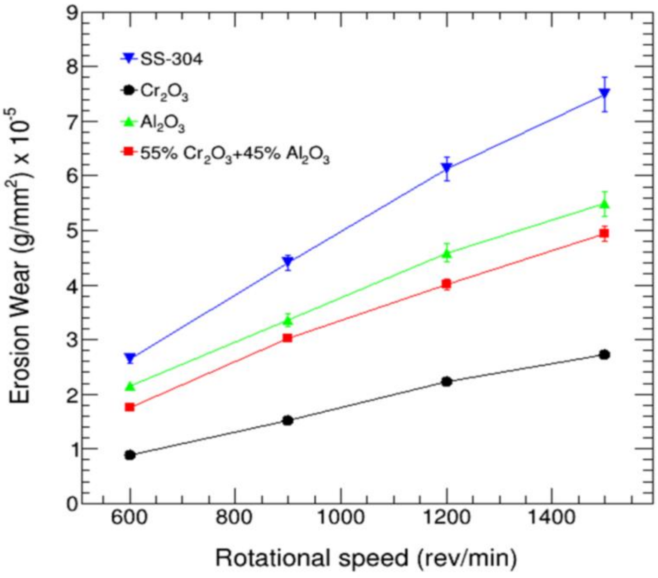

Figure 4.18. Influence of rotational speed on erosion wear.

4.5.3 Influence of concentration

Figure 4.19 illustrates the effect of variation of silt concentration on the specific erosion wear of coated specimens and bare SS-304. The tests were carried out using four distinct silt concentrations i.e., 12, 22, 32 and 42% at maximum speed of rotation as 1500 rev/min for maximum time span of four hours at a granular silt range of 212-250 μm to evaluate the impact of silt slurry concentration. Erosion wear surge with increasing silt concentration. This may be due to the fact that the area of particles in the specimen's striking zone rises, resulting in significant erosion wear at high concentrations (Arji et al., 2009; Sidhu et al., 2007). The maximum erosion wear take place at the concentration of 42% for all the test specimens for which the maximum erosion wear is observed for bare SS-304 having value as 9.906×10^{-5} g/mm^2 and the maximum resistance to erosion has been shown by Cr_2O_3 coating having value as 3.490×10^{-5} g/mm^2.

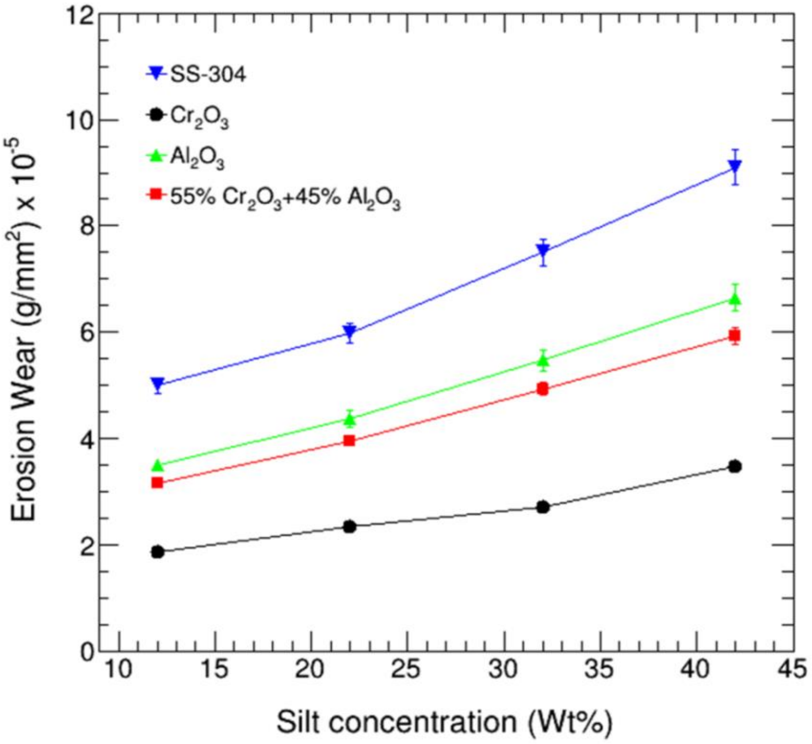

Figure 4.19. Influence of concentration on erosion wear.

4.5.4 Influence of silt particle size

To explore the action of silt particle size range on erosion wear, trails were performed by using particle size ranges 212-250 μm, 150-212 μm, 106-53 μm and <53 μm to the utmost speed of 1500 rev/min with silt concentration maintained at 30% as shown in **Figure 4.20**. Larger particle sizes have been shown to increase erosion wear as shown in **Figure 4.21**. This is due to the large momentum or energy transfer associated with large particles compared to small particles, consistent with the previous results (Singh, 2021d, 2021e; Singh and Singh, 2022). Silt with a particle size of 212-250 µm showed maximum erosion wear. Maximum erosion wear was observed on bare SS-304 with a value of 7.5215×10^{-5} g/mm^2, and in addition to a value of 2.86×10^{-5} g/mm^2, minimum erosion wear of the Cr_2O_3 coating was observed. So, for the effects of speed of rotation, silt concentration and silt particle size the erosion wear of the specimens is found in the following order as SS-304> Al_2O_3>55% Cr_2O_3 +45% Al_2O_3 > Cr_2O_3.

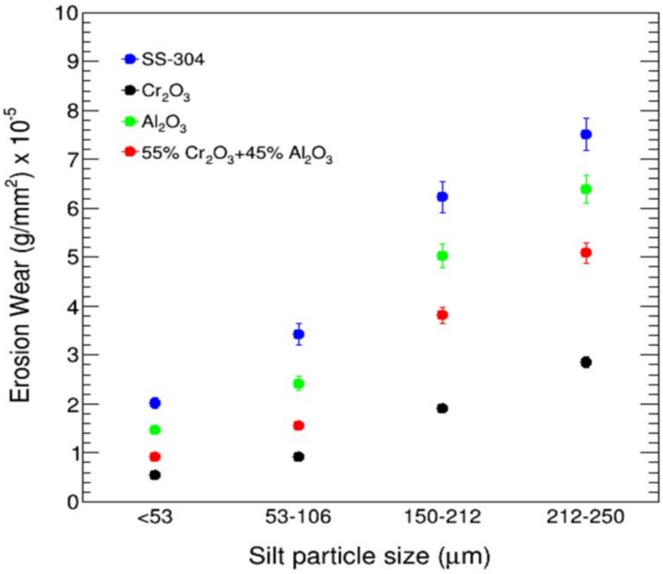

Figure 4.20. Influence of particle size on erosion wear.

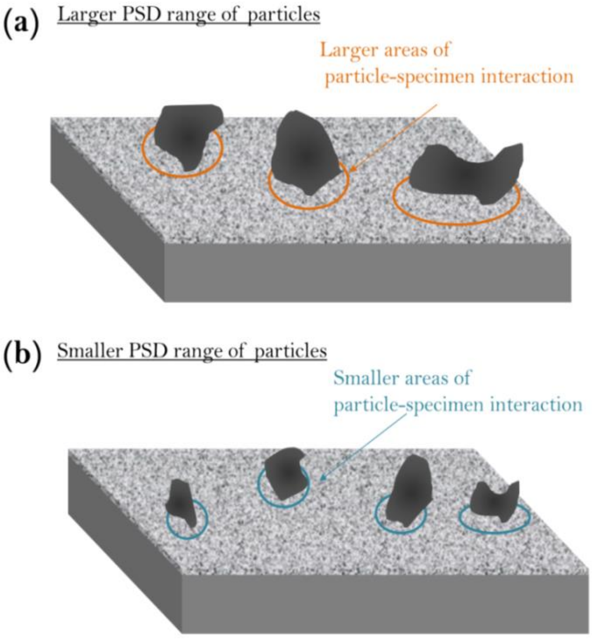

Figure 4.21. Schematic diagram on effect of particle size on erosion.

As for all the effect of various parameters 4.5.1, 4.5.2, 4.5.3, 4.5.4 it was observed that Cr_2O_3 coating showed highest erosion among all. It may be due to the higher hardness of chromia coating as compared to others which can be confirmed from **Table 4.3**. Also, as depicted in **Figure 4.10(c),** the XRD graphs for the composite composition show the presence α- Al_2O_3. The addition of Cr_2O_3 to Al_2O_3 stabilizes the α- Al_2O_3 which leads to more refinement in grain structures as compared to Al_2O_3 coating as has been reported by Yang.et.al (2011) for Al_2O_3-Cr_2O_3 composite coatings developed by atmospheric plasma spraying method.

4.5.5 Post-erosion microstructural characterization

The microstructural analysis of the eroded samples has been analysed by a scanning electron microscope. The SEM micrographs of eroded samples have been shown in **Figure 4.22**. **Figure 4.22(a)** shows the erosion wear process of SS-304 at 1000 rev/min, with the particle size of silt as 350-450 µm and the concentration of silt as 50%. **Figure 4.22(a)** shows the presence of crater, pits and ploughing. Also, the size and depth of the crater is much smaller as compare to other crater created with higher rotational speed.

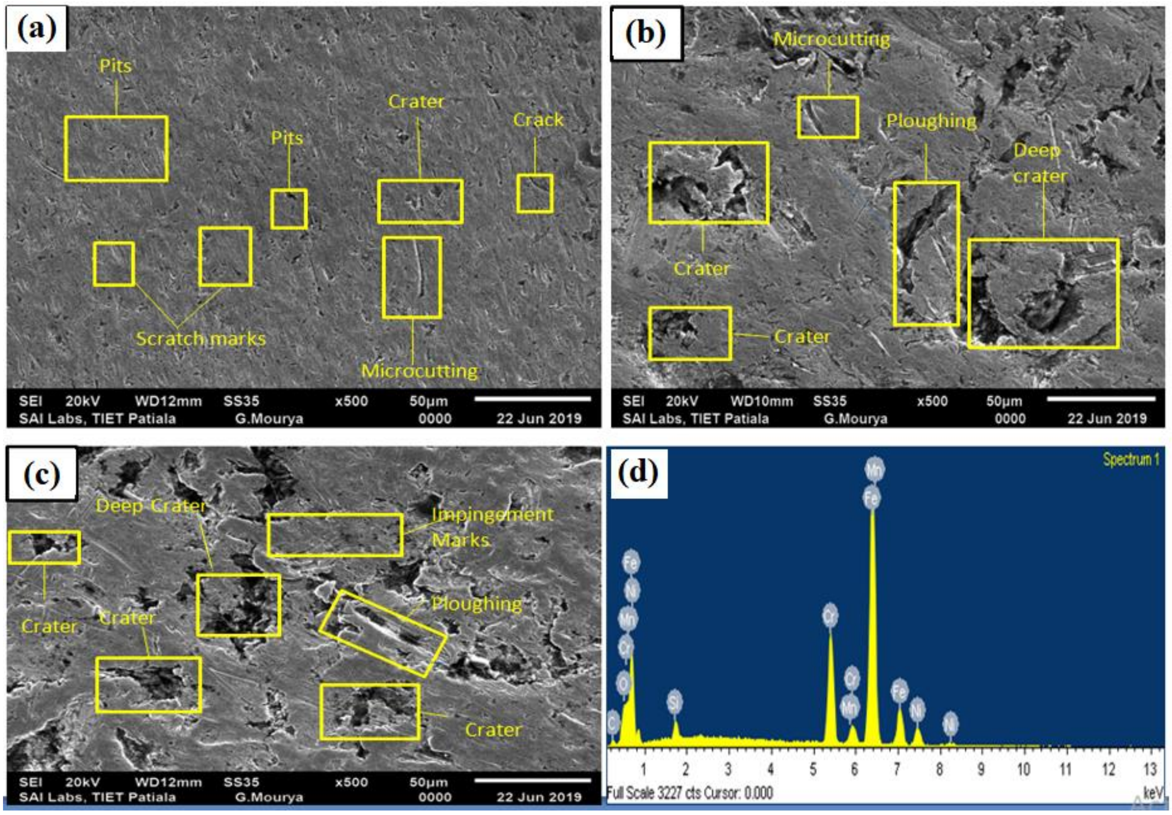

Figure 4.22. SEM images of eroded SS-304 substrates at particle size 350-450 µm and 50% silt concentration at rotational speed of (a) 1000, (b) 1250 and (c) 1500 rev/min, and (d) EDS analysis at rotational speed of 1500 rev/min for 4 hours.

The wear mechanism shows the formation of pits, craters, and some areas of scratch marks, as the speed increased to a value of 1250 rev/min (**Figure 4.22b**). As the rev/min is further increased to 1500 for testing the next specimen whose SEM micro characterization and EDS are shown in **Figure 4.22(c, d)**. This too shows the presence of various wear mechanisms as ploughing and deep craters but the severity of ploughing and crater depth is much more than at values at the lower rev/min counterparts. The EDS shows the presence of various elements in SS-304 as C, O, Si, Cr, Mn, Ni, and Fe to the percentage of 0.12%, 3.07%, 1.68%, 17.29%, 1.20%, 8.35%, and 68.29%. Also, it is clear from the SEM micrograph that the severity of erosion also increases as the rotational speed was increased from the lower to the higher values.

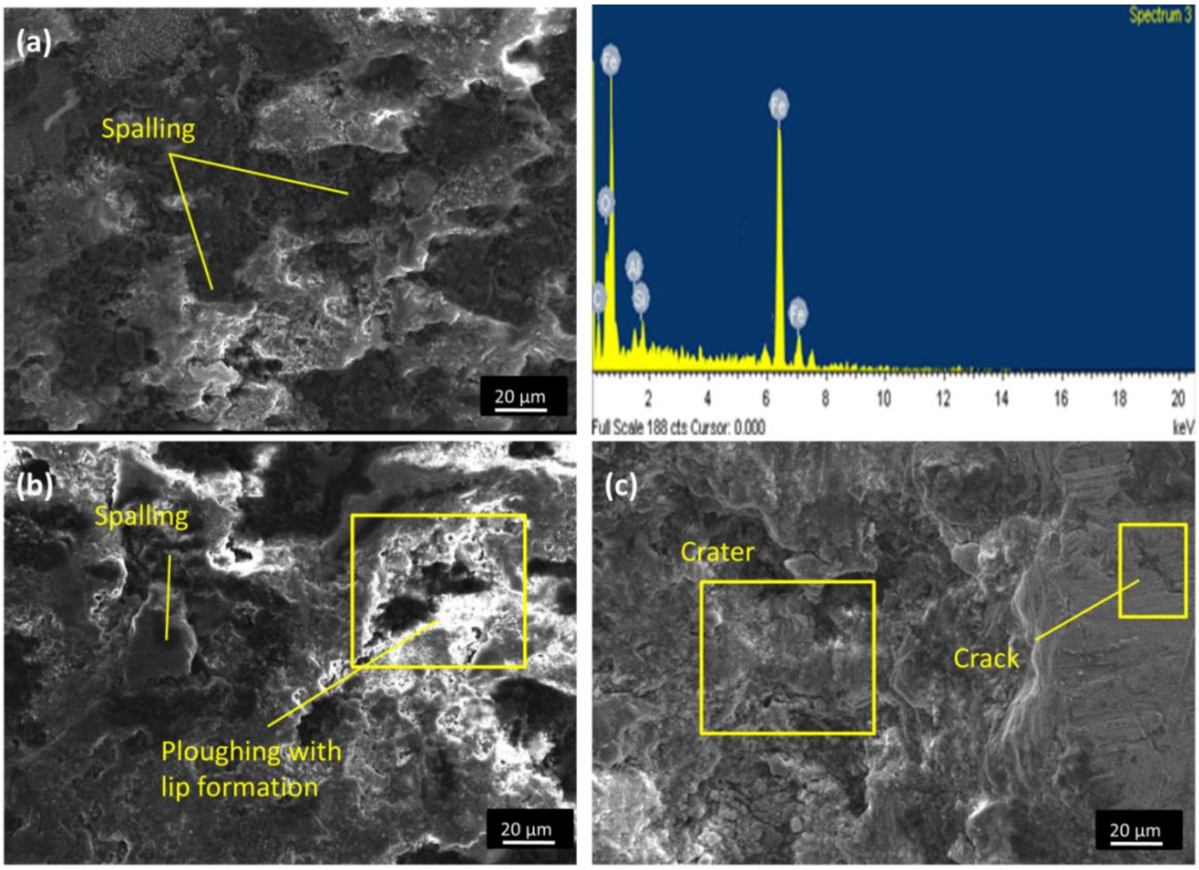

Figure 4.23. SEM Images of eroded Al_2O_3 coated substrates at rotational speed 1500 rev/min and 30% concentration (a) silt particle size: 212-250 µm (with EDS), (b) silt particle size: 150-212 µm, and (c) silt particle size: 53-106 µm.

Figure 4.23 shows the eroded Al_2O_3 sprayed HVOF coating. From **Figure 4.23(a)**, it can be remarked that the major mechanism of material removal is spalling of Al_2O_3 and craters however eroded Al_2O_3 coating also shows the ploughing, cracks and craters for smaller sizes particles, as seen in **Figure 4.23(b, c)**. **Figure 4.24(a)** shows the eroded Al_2O_3 coating spall-out due to the spalling of Al_2O_3. This may be attributed to low cohesive strength between the deposited particles (Ahmed, 2002; Yang et al., 2016). Also, as the coating have more unmelted particles as shown in **Figure 4.23(a)** which can be removed easily during the testing conditions so responsible for more wear. The EDS of HVOF coated Al_2O_3 eroded substrate at rotational speed of 1500 rev/min, 30% silt concentration having particle size 212-250 µm is shown in **Figure 4.23(a)**. EDS spectrum illustrates the presence of elements as C, O, Al, Si and Fe to the percentages of 1.13%, 26.58%, 20.02%, 3.05%, 49.22%.

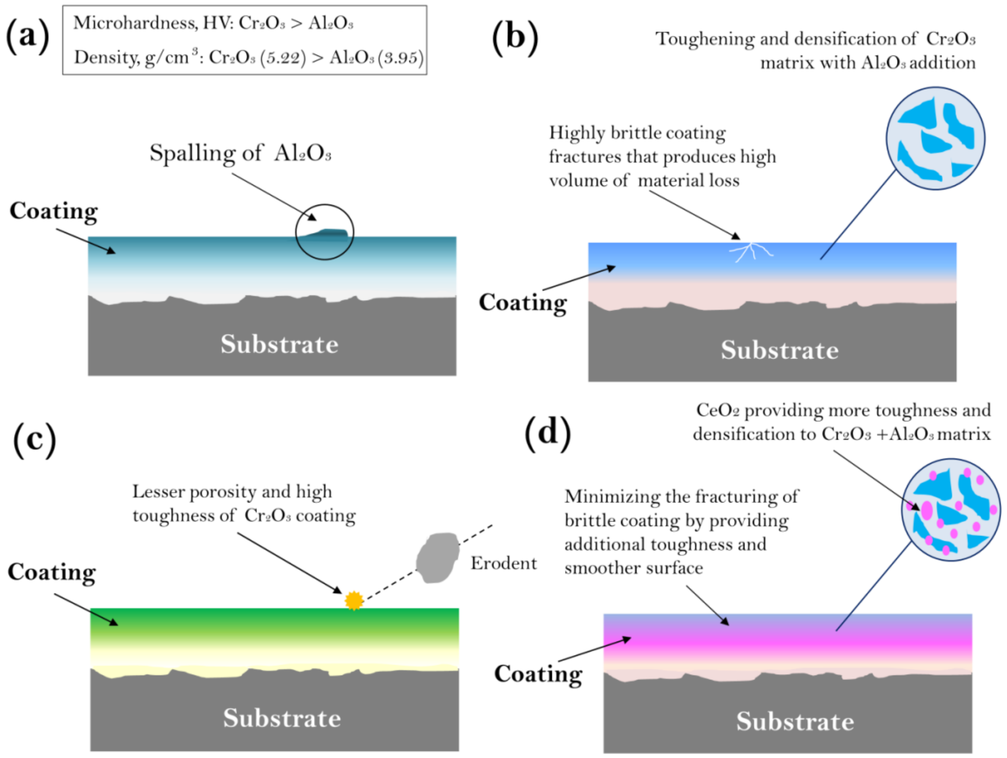

Figure 4.24. Schematic diagram of erosion mechanisms in (a) Al_2O_3, (b) 55% Cr_2O_3 + 45% Al_2O_3, (c) Cr_2O_3 sprayed coatings, and (d) 0.5% CeO_2 added Cr_2O_3+ Al_2O_3.

Figure 4.25 shows the eroded samples of composite coating of composition 55%Cr_2O_3 + 45%Al_2O_3. As depicted in **Figure 4.25(a-c)** the mechanism responsible for erosion wear are pull of particles, ploughing, micro-cracks and signs of microcutting are also visible. The mechanism of erosion wear as observed for this coating is mostly mixed as ploughing and micro cutting are responsible for ductile erosion wear behaviour as researched by various authors (Ahmed Elkholy, 1983; Gandhi et al., 2003). Also traces of brittle mode of material removal was observed as it involves the presence of pull off, cracking and splat removal as supported by researchers (Singh et al., 2022; Vashishtha et al., 2017). The composite coating has shown enhanced resistance to erosion wear as compared to Al_2O_3 coating for all testing conditions for silt slurry and at all testing parameters. This may be attributed to the increase in cohesive strength of Al_2O_3 by the addition of Cr_2O_3 which act as a density enhancer and binder for Al_2O_3 which has been investigated by Yang et al. (2016) for plasma sprayed alumina based coatings. This phenomenon is schematically shown in **Figure 4.24(b)**. In **Figure 4.24(b)**, it is also represented that the brittle-matrix and brittle-reinforcement produces more brittle coating which can fracture under the erosion action. The EDS of HVOF coated 45% Al_2O_3+55%Cr_2O_3 eroded substrate at 1500 rev/min, 30% silt concentration having silt particle size 212-250 µm corresponding to **Figure 4.25(a)** highlights the presence of traces of C, O, Al, Si, Cr and Fe to the values of 2.12%, 24.47%, 10%, 3.25%, 20.12% and 40.04%.

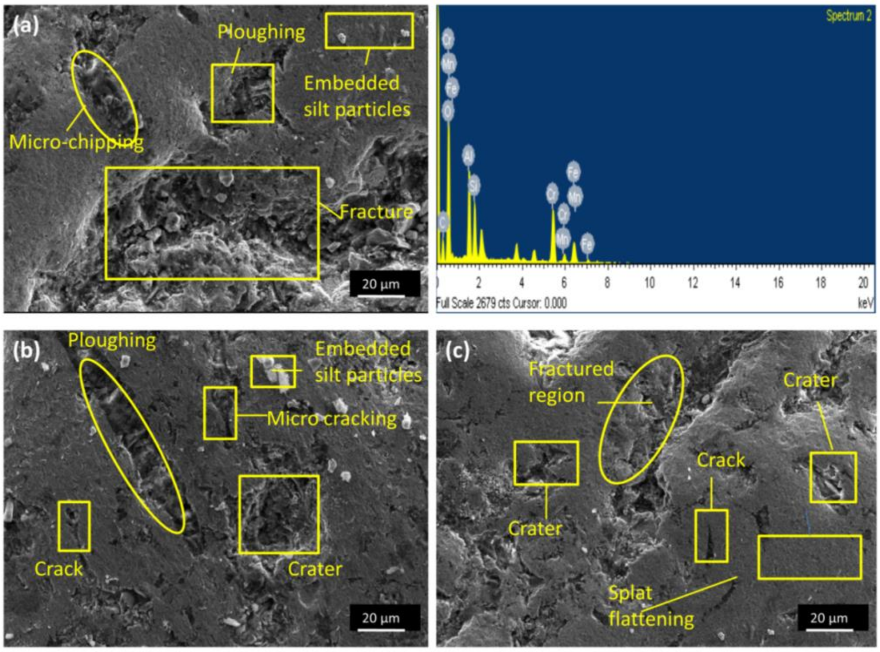

Figure 4.25. SEM Images of eroded 55% Cr_2O_3 + 45% Al_2O_3 coated substrates at rotational speed 1500 and 30% concentration (a) silt particle size: 212-250 µm and EDS, (b) silt particle size: 150-212 µm, and (c) silt particle size 53-106 µm.

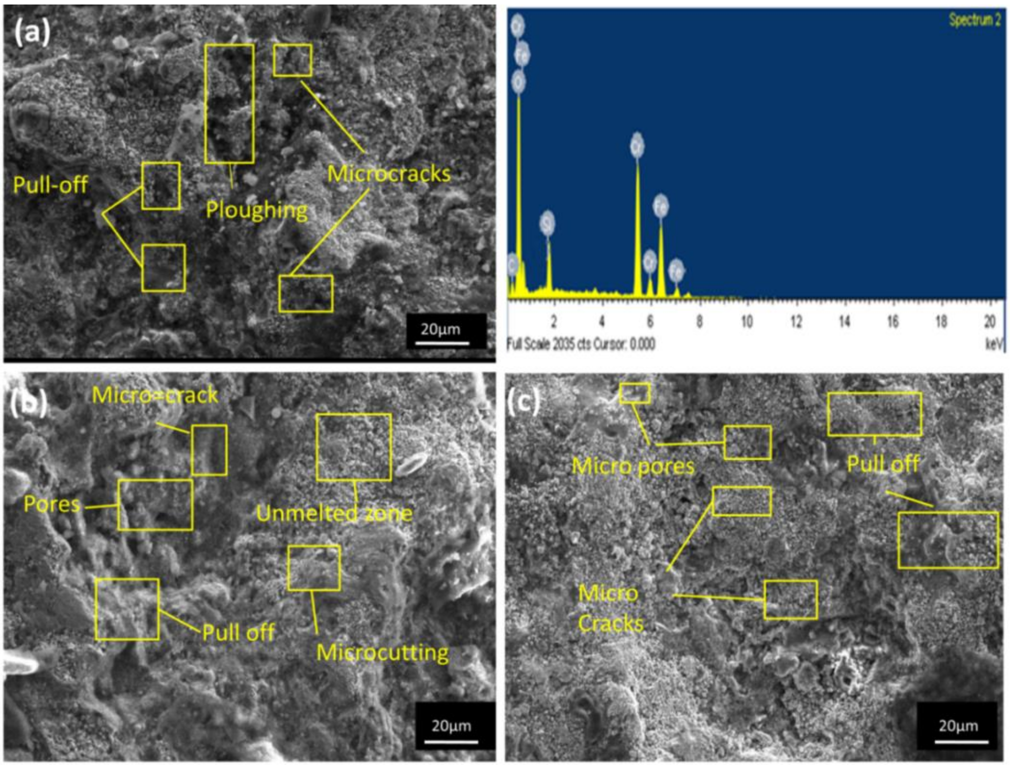

Figure 4.26. SEM Images of eroded Cr_2O_3 coated substrates at rotational speed 1500rev/min and 30% concentration: (a) silt particle size: 212-250 µm and EDS, (b) silt particle size: 150-212 µm, and (c) silt particle size: 53-106 µm.

Figure 4.26 shows the eroded samples of HVOF coated pure Cr_2O_3 coating. The wear mechanism shows the presence of micro cutting, ploughing, and craters along with micro-cracks at some portions. Also, the presence of unmelted particles as visible from **Figures 4.26(a-c)** has not detached from the coated surface during the experimentation. This may be attributed to good adhesion of particles. Further of all the coatings, Cr_2O_3 has high hardness and low porosity values as shown in **Table 4.3**. Moreover, the lesser porosity, tough matrix, and higher hardness resist the impact of silt, as illustrated in **Figures 4.24(c)**. This can be attributed to more increase in resistance to erosion wear by the coating. Similar analogical studies has been reported for HVOF sprayed WC-17Co and WC-120Co coatings for which increase in material hardness leads to improved wear resistance as well (Kumar et al., 2022; Saha et al., 2010). Porosity too has an influence on the erosion properties of thermally sprayed coatings as it influences the strength between the lamellae and is also responsible for micro cracks that contribute to the loss of lamellae and thus to the coating removal (Hearley et al., 1999). The EDS of HVOF coated Cr_2O_3 eroded substrate at rotational speed of 1500 rev/min, 30% silt concentration having silt particle size 212-250 µm corresponding to **Figure**

4.26(a) shows constituent elements as C, O, Si, Cr and Fe having percentages as 0.85%, 25.23%, 4.55%, 36.26%, and 33.11% respectively. **Figure 4.23, 4.24** and **4.26** depicts that the coating exhibits the brittle mode of failure.

4.6 EROSION PERFORMANCE OF CERIA REINFORCED COATINGS

4.6.1 Influence of rotational speed

The effect of the rotating speed on the erosion wear of coated and uncoated SS-304 is shown in **Figure 4.27** at particle size of silt as 212-250 µm and concentration of silt as 30%. The relative weight loss from the specimen is measured as weight loss in (g) per unit area (mm^2) in the current investigation. It has been discovered that as rotational speed increases erosion wear also escalates. It is because the silt particles gain high momentum which in turn gets transferred to specimen under pot silt slurry conditions and similar results have been found by the investigators (Grewal et al., 2013b; Zu et al., 1990) which depicts surge in rotational speed increases erosion wear. At a rotational speed of 1500 rev/min the highest erosion wear was observed. It has also been observed that the maximum erosion wear occurs for bare SS-304 to the value of 7.4875×10^{-5} g/mm^2 and the least erosion wear is shown by the coating having 0.5% CeO_2 addition having erosion wear as 2.99×10^{-5} g/mm^2.

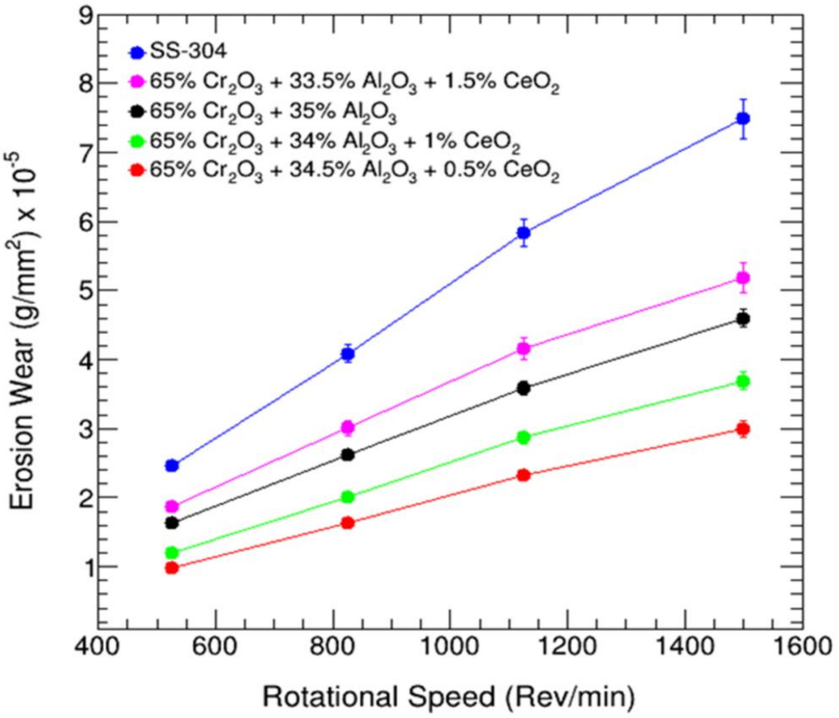

Figure 4.27. Effect of rotational speed on erosion wear for various coatings and SS-304.

4.6.2 Influence of concentration

Figure 4.28 shows the comparison of specific erosion wear of coated surfaces and bare SS-304 with varied silt concentration at maximum rotational speed of 1500 rev/min for maximum time duration of 4 hours at a particle size of 212-250 µm to evaluate the impact of slurry concentration. It has been determined that the erosion wear increases as silt concentration rises which could be due to more solid silt particles per unit volume of water in the experimental conditions. As a result, a higher erosion rate is caused by a larger aggregation of impacting erodent particles. Various researchers (Hong et al., 2013; Mann, 2000; Santa et al., 2009, 2007) have reached similar conclusions. For all the testing conditions the maximum erosion wear take place at the concentration of 40 wt.%.The maximum erosion wear is observed for bare SS-304 having value as 8.985×10^{-5} g/mm^2 and the maximum resistance to erosion has been shown by the coating having 0.5% CeO_2 addition which has minimum value of erosion wear as 3.864×10^{-5} g/mm^2.

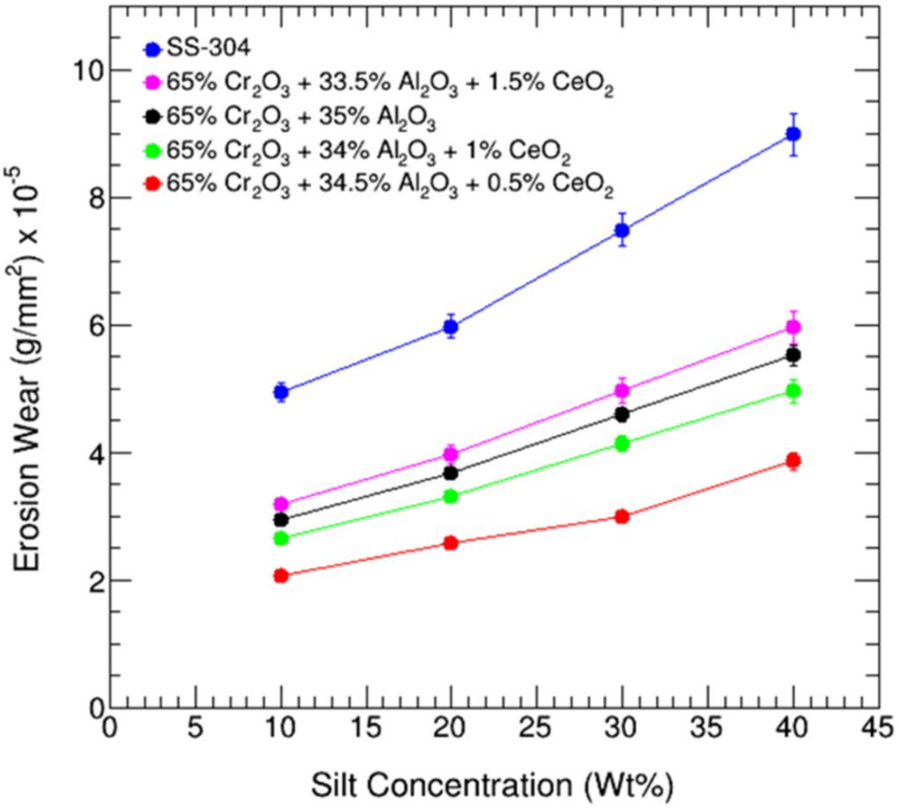

Figure 4.28. Effect of silt concentration on erosion wear for various coatings and SS-304.

4.6.3 Influence of silt particle size

To move further and evaluate the effect of silt particle size range on erosive wear, experiments were conducted at 212-250 µm, 150-212 µm, and 53-106 µm at maximum rotational speed of 1500 rev/min with silt concentration as 30% as shown in **Figure 4.29**. It has been shown that when particle size grows, erosion wear increases which is owing to the significant momentum or energy transfer associated with large particles as compared to small particles which is coherent with the findings of authors (Jonda et al., 2023; Łatka et al., 2023; Szala et al., 2020, 2014). The silt of particle size 212-250 µm has shown the maximum erosion wear. The maximum erosion wear has been observed for bare SS-304 having value as 7.4875×10^{-5} g/mm^2. Minimum erosion wear has been observed for the coating of 0.5% CeO_2 addition to the value of 3.2207 ×10^{-5} g/mm^2.

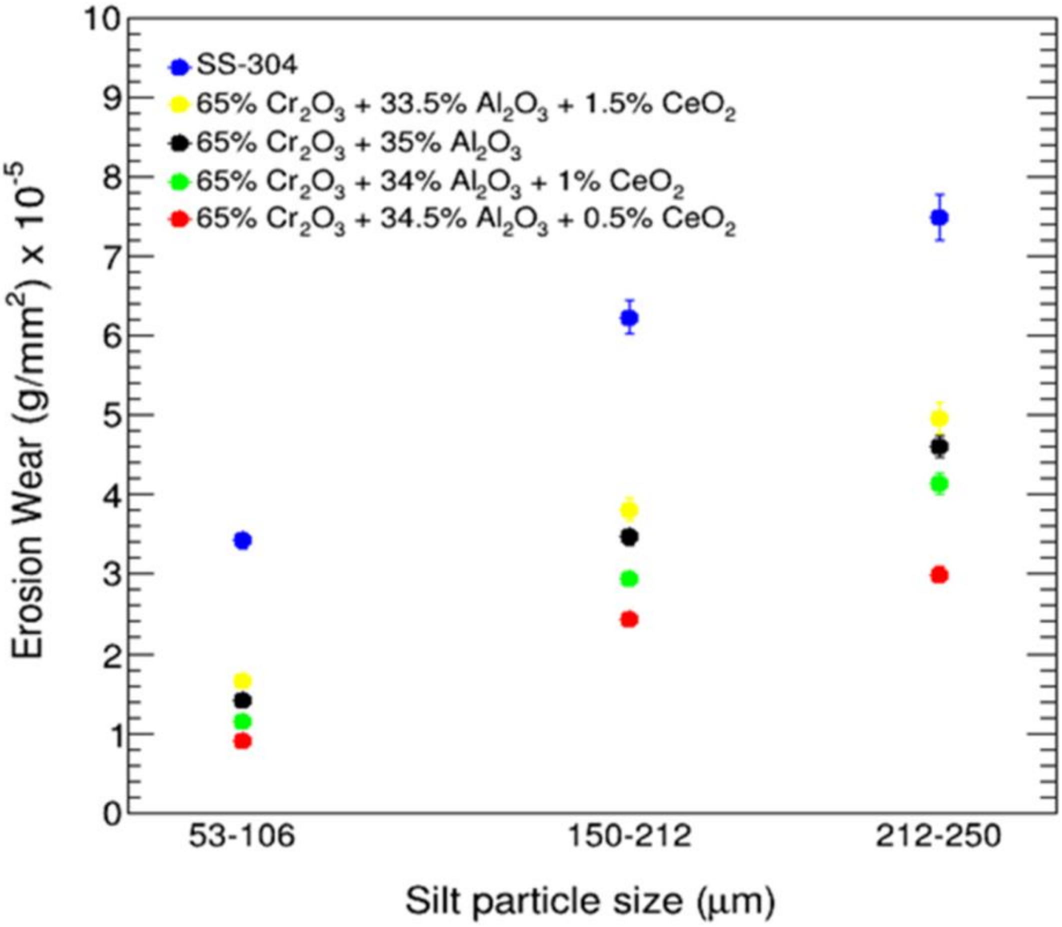

Figure 4.29. Effect of particle size of silt on erosion wear for various coatings and SS-304.

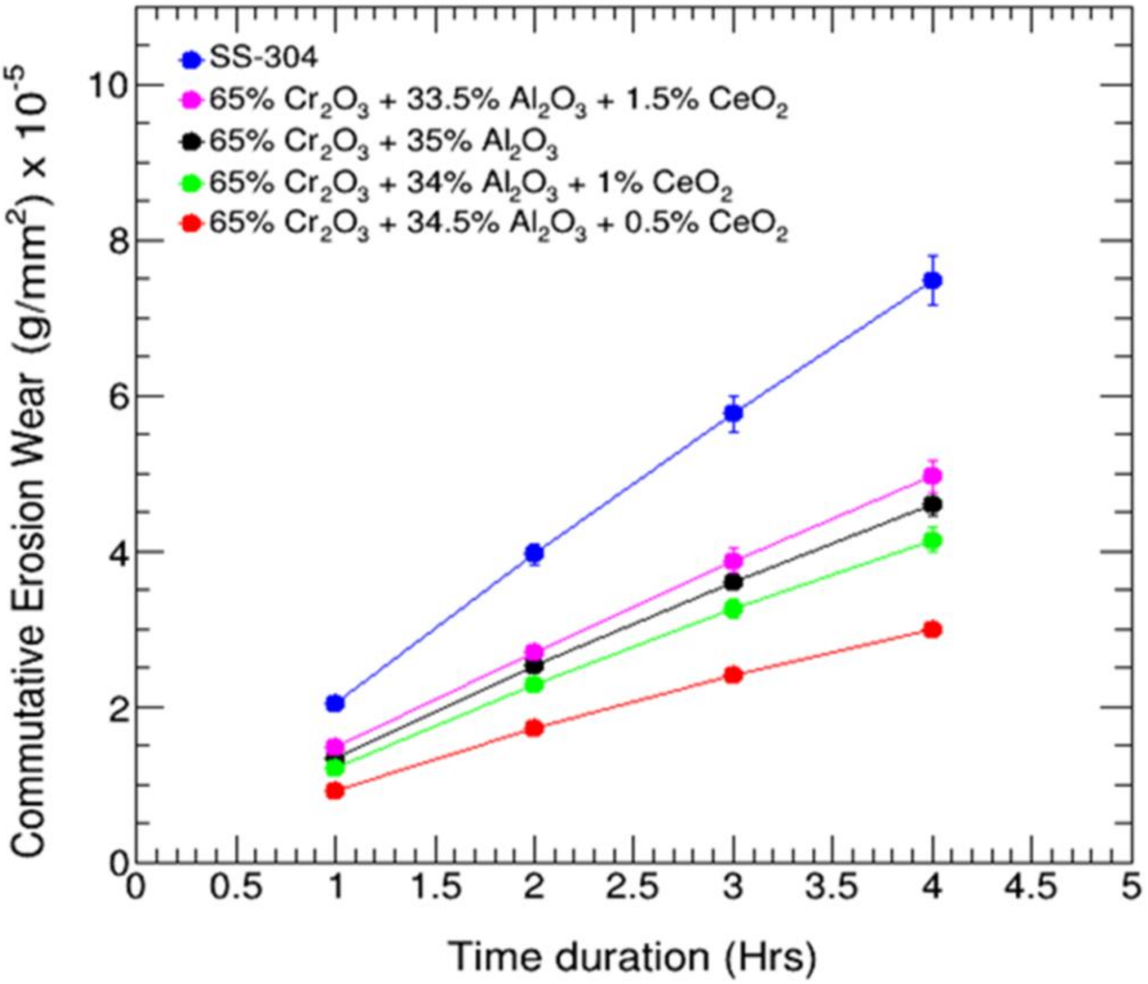

Figure 4.30. Effect of time duration on erosion wear for various coatings and SS-304.

4.6.4 Influence of time duration

In **Figure 4.30** at particle size 212-250 µm, concentration 30% and rotational speed 1500 rev/min, it has been examined that as the experimentation time progressed the relative erosion wear decreases and the commutative erosion wear increases. During the initial phase it has been found that the erosion wear is more and consequently decreases towards the fourth hour. This can be attributed to the rounding of the sharp angular particles of erodent as consonance with the findings of the investigator (Thakur and Arora, 2013). The utmost erosion wear has been observed for SS-304 to the value of 2.046×10^{-5} g/mm^2 for the first hour and commutative value of 7.4875×10^{-5} g/mm^2 for four hours. For all the coatings for the time period of initial 1-hour minimum erosion wear was found out to be 0.922×10^{-5} g/mm^2 for 0.5% CeO_2 addition and the maximum erosion wear has been shown by coating composition having 1.5% CeO_2 to the value of 1.417×10^{-5} g/mm^2. When compared to bare SS-304, the coatings outlined above for the major impacting parameters shows a significant improvement for the erosion wear. The addition of CeO_2 to the composite coating to the value of 0.5%, 1%, and 1.5% has significantly enhanced the hardness of the composite coating which is an indispensable property for showing the increased resistance to erosion wear. Similar results have been obtained by the authors which shows that the erosion resistance has been increased due to increase in the hardness of the coating (Buszko and Krella, 2017; Sharma et al., 2020). As for all the parameters discussed for erosion wear given in section 4.6.1, 4.6.2, 4.6.3, 4.6.4, it was observed that when compared among all the deposited coatings with and without CeO_2 addition, coating with 0.5% CeO_2 has a strong erosion resistance. This is owing to the coating high hardness and low porosity value. The coatings with addition of 1% and 1.5% CeO_2 have low values of hardness and high values of porosity as compared to coating of 0.5% CeO_2 addition thereby showing more erosion wear. Porosity has an impact on the erosion properties of thermally sprayed coatings because it affects the inter lamella strength and is also responsible for micro cracks that contribute to lamella loss and hence coating removal (Hearley et al., 1999).

It was also reported that there is substantial change in microstructure of the coating when low quantity of ceria was added. The mechanism underlying this can be explained by the propensity for increased grain formation and subsequent growth in crystal nuclei, which resulted in grain refinement. As rare earth has high atomic radii, it tends to occupy the site at the grain border, which inhibits grain formation and eventually affects hardness and wear property of materials. The property of CeO_2 being playing a vital role in microstructure refinement has been reported by Zhang et al. (2007).

Apart from all the factors discussed above, it was also noticed that the sample size has a great impact on erosion wear. It was observed that the leading edges of the specimen get eroded more severely as compared to the central part of the specimen. A similar result has been reported elsewhere (Singh et al., 2020).

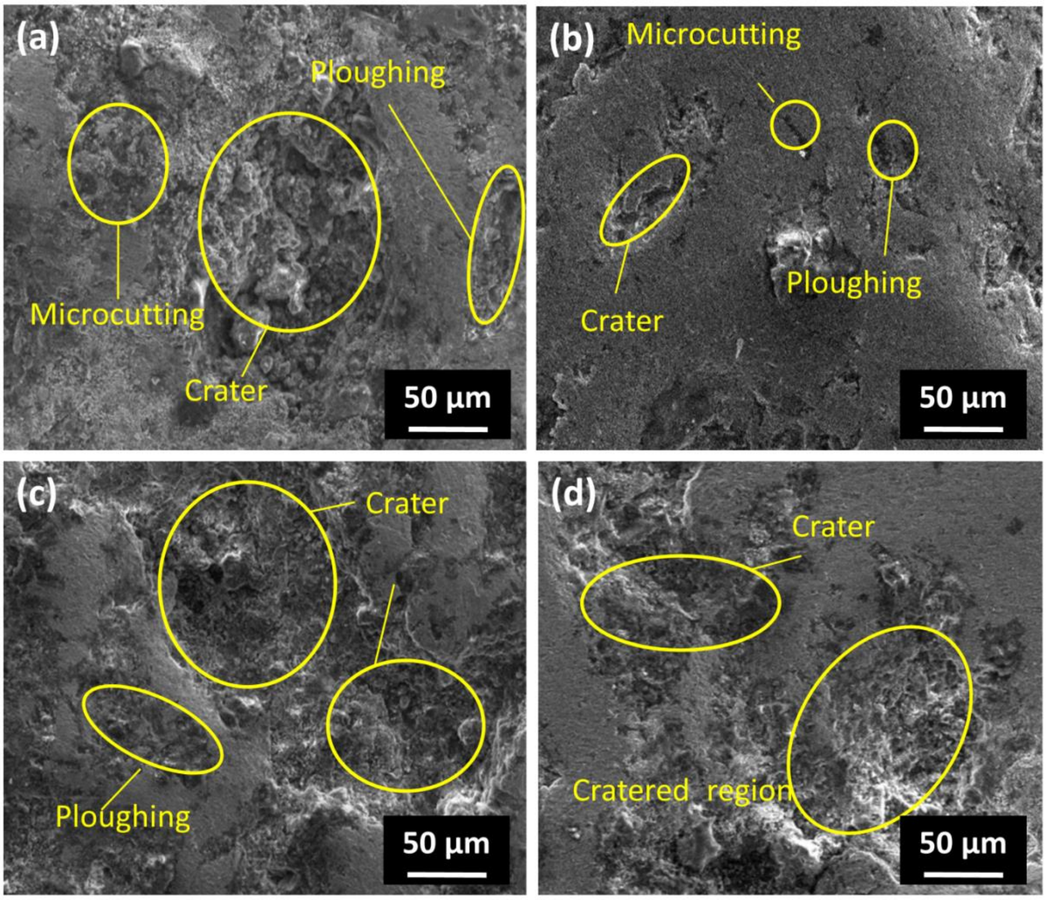

Figure 4.31. SEM micrographs of eroded samples at silt particle size of 212-250 µm of coating (a) 65% Cr_2O_3+35% Al_2O_3, (b) 65% Cr_2O_3+34.5% Al_2O_3+0.5% CeO_2, (c) 65% Cr_2O_3+34% Al_2O_3+1% CeO_2, and (d) 65% Cr_2O_3+33.5% Al_2O_3+1.5% CeO_2.

4.6.5 Post-erosion microstructural characterization

The as-sprayed and eroded samples were examined micro structurally using a SEM machine built in Netherland with the model number JSM-6510L. The SEM micrographs of the eroded substrates for the different coatings using different silt particle size of range 212-250 µm and 150-212 µm at rotational speed of 1500 rev/min and at 30% silt concentration for time duration 4 hours has been shown in **Figure 4.31** and **4.32**. **Figure 4.31** shows the erosion wear mechanism of deposited coatings subjected to silt slurry of 30% concentration, rotational speed of 1500 rev/min and at particle size of value 212-250 µm. It shows the presence of craters, ploughing, micro-cutting and relatively pulls out at some places. As can be observed from the SEM micrograph in **Figure 4.31(d)** of coating composition 65%Cr_2O_3+33.5%Al_2O_3+1.5%CeO_2, the severity of erosion is more as the eroded ploughing region has been spread to the larger surface area compared to other coated counterparts. Also, the erosion wear is more here which is evident from the erosion wear graphs. Erosion wear mechanism is a complex phenomenon which depends upon the type of material, velocity of particles and also on shape and size of particles which has been mentioned by many investigators (Gandhi et al., 2003; Manisekaran et al., 2007; Vashishtha et al., 2017).

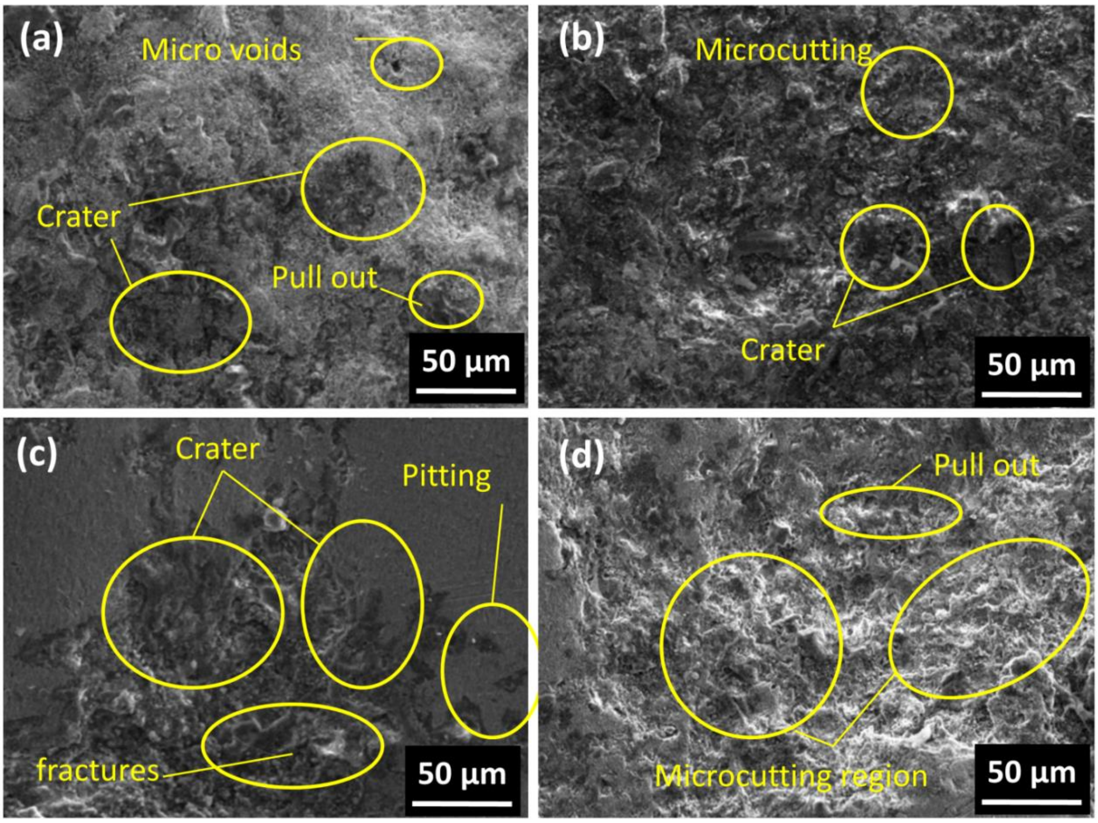

Figure 4.32. SEM micrographs of eroded samples at silt particle size of 150-212 µm of coating (a) 65% Cr_2O_3+35% Al_2O_3, (b) 65% Cr_2O_3+34.5% Al_2O_3+0.5% CeO_2, (c) 65% Cr_2O_3+34% Al_2O_3+1% CeO_2, and (d) 65% Cr_2O_3+33.5% Al_2O_3+1.5% CeO_2.

Figure 4.32 shows the erosion wear mechanism of mentioned coatings at a particle size of 150-212 µm at rotational speed of 1500 rev/min at 30% silt concentration. The SEM micrographs reveal the presence of craters, micro-cutting, and most notably ploughing for the eroded samples. Also, the SEM micrographs in **Figure 4.32(d)** of coating composition 65%Cr_2O_3+33.5%Al_2O_3+1.5%CeO_2 shows the more austerity of erosion as ploughing is severe as compared to other coated counterparts. Least erosion wear is shown by the coating of 65% Cr_2O_3+34.5% Al_2O_3+0.5% CeO_2. It may be due to the higher hardness and toughness of 0.5% CeO_2 added coating as shown in **Table 4.3**. It was very well known that hardness plays a vital role in providing the resistance to the erosion wear (Buszko and Krella, 2017). The examination of the eroded samples reveals that the size, depth of craters and ploughing increases predominantly as the range of the silt size particles for erosion increases from 150-212 µm to 212-250 µm. This has also been backed by several researchers (Desale et al., 2011, 2008, 2005) who looked into the influence of different particle sizes on erosion wear and found that wear increases as erodent particle size increases. Of all the cases discussed above for the different range of silt sizes it has been examined that the coating of composition with 0.5% CeO_2 addition has better resistance and low wear rate to silt slurry erosion as compared to the other developed HVOF coatings in the study which may be attributed to significant increase in hardness and low porosity values when compared with other coatings. This examines that there is an ideal CeO_2 composition for maximizing erosion wear resistance which has also been reported for laser clad coatings (Wang et al., 2001).

4.7 REMARKS

- As the rotational speed of the substrate in the silt slurry increases the weight loss of the substrate also increases thereby increasing the erosion rate.
- As time progressed the weight loss tends to increase but the erosion rate is found to be decreased.
- For HVOF coated and uncoated substrates the following order of erosion wear is observed as SS-304 > Al_2O_3>45% Al_2O_3+55%Cr_2O_3 > Cr_2O_3.
- For HVOF coated and uncoated substrates the following order of erosion wear is observed as SS-304 > 65%Cr_2O_3+34%Al_2O_3+1.5%CeO_2 > 65%Cr_2O_3+35%Al_2O_3 > 65%Cr_2O_3+34%Al_2O_3+1%$CeO_2$$Cr_2O_3$ > 65%Cr_2O_3+34.5%Al_2O_3+0.5%CeO_2.

CHAPTER 5

EFFECT OF INFLUENCING PARAMETERS ON SILT EROSION

In this chapter, the effect of different influencing parameters has been studied using Taguchi’s method. The design of experiment is the arrangement of condition for collection and analysis of data in a manner that aims to combine relevance to the research purpose with economy in procedure. For the experimental design Taguchi’s method has been selected for the optimization of output parameter in terms of erosion wear (Taguchi, 1990).

5.1 MATERIAL USED FOR DESIGN OF EXPERIMENTS

Stainless steel of grade 304 has been used as the base material. The specimens are cut from a long rectangular bar to the dimensions of 65×25×5 mm. Specimen geometry is illustrated in previous chapter. In order to conveniently attach specimen to the test apparatus for carrying out investigation a hole of 8 mm diameter is drilled through the centre of specimen.

Table 5.1: Average hardness, porosity and roughness values of investigated specimens.

Material/Coating composition	Average hardness (HV) ± (6%)	Porosity (%)	Average roughness (µm)
SS-304	284	---	0.43
75%Cr_2O_3+25%Al_2O_3	1230	1.15	6.01
85%Cr_2O_3+15Al_2O_3	1275	1.01	6.35

To enhance the surface morphology of the bare stainless steel for increased resistance to erosion wear the samples are coated by developing HVOF sprayed coatings of composition 75%Cr_2O_3+25%Al_2O_3 and 85%Cr_2O_3+15%Al_2O_3. The requisite compositional powders are then ball milled for 100 hours to obtain the homogeneity in mixing of powders. The coating powders are also examined using SEM and EDS to be recognizable with the morphology and elemental make up. The SEM image of Al_2O_3 and Cr_2O_3, and SEM-EDS images of 85%Cr_2O_3+15% Al_2O_3 powders is shown in **Figure 5.1**. The samples are analysed for Vickers micro hardness, surface roughness and porosities values. The properties of deposited coatings are highlighted in **Table 5.1**. In four trails conducted SS-304 has an average micro hardness of 284 HV. Furthermore, the micro hardness values of SS-304 sprayed HVOF coatings significantly increase being the greatest value being measured in case of 85%Cr_2O_3+15Al_2O_3 coating.

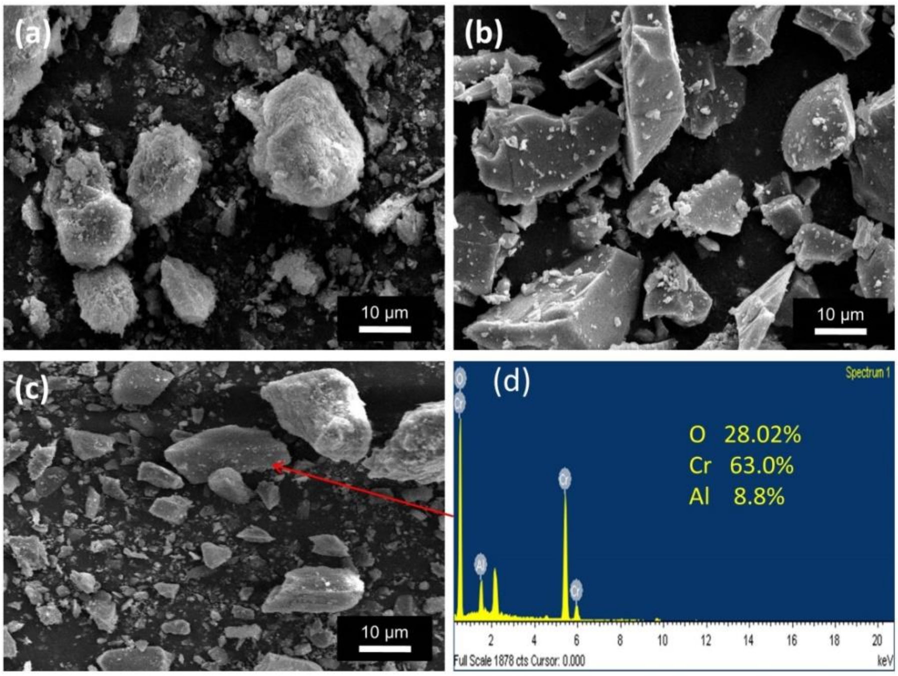

Figure 5.1. (a) SEM image of Al_2O_3 Powder, (b) SEM image of Cr_2O_3 Powder, and (c and d) SEM-EDS images of 85%Cr_2O_3+15% Al_2O_3 composite powder.

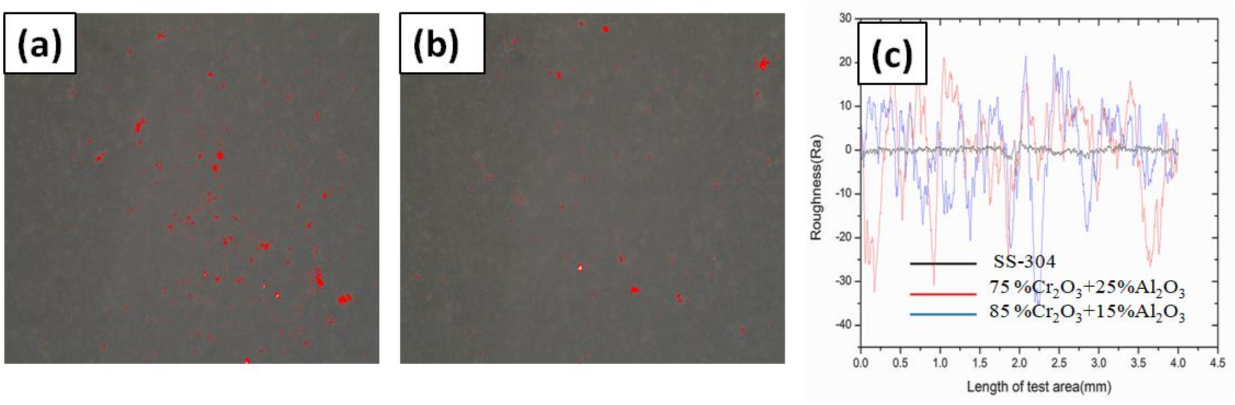

Figure 5.2. Porosity of (a) 75%Cr_2O_3+25%Al_2O_3 (b) 85%Cr_2O_3+15Al_2O_3 sprayed coatings (d) roughness profile of SS-304 and sprayed coatings

For measuring the porosities of the HVOF sprayed coating, the image processing technique was used and the lowest value for porosity has been observed for 85%Cr_2O_3+15Al_2O_3 coating. The porosity and roughness profiles of 75%Cr_2O_3+25%Al_2O_3 and 85%Cr_2O_3+15Al_2O_3 sprayed coatings are shown in **Figure 5.2(a, b)**. The average roughness of uncoated and HVOF coated surfaces was measured using an SJ-400 surface test roughness tester made by Mituto (USA). From **Figure 5.2(c)**, the roughness of 85%Cr_2O_3+15Al_2O_3 coating was found more than the 75%Cr_2O_3+25%Al_2O_3 coating.

5.2 TAGUCHI'S METHOD

The erosion wear is expressed in terms of g/mm^2. Three input factors were considered in current study and each parameter can be varied to four levels as shown in **Table 5.2**. For determining the quality of output characteristic signal to noise (S/N) ratio is used. By maximizing the S/N ratio, the loss associated can be minimized. The S/N ratio determines the most robust set of operating conditions from variation within the results. As the erosion wear is to be minimized the quality characteristic followed is smaller the better and the analytical expression is given as:

$$S/N = -10 \log [(1/n) \times \Sigma y_i^2] \qquad (5.1)$$

Where y_i is the result of experiment in each trail. Minitab 16 is used as the statistical tool for this purpose. In the current investigation the tribological erosion wear optimization experiments have been designed as per Taguchi's approach for uncoated and coated HVOF sprayed Al_2O_3 and Cr_2O_3 composite coatings. The experiments were conducted using silt as erodent material sieved to different particle size as <53 µm, 53-106 µm, 150-212 µm, and 212-250 µm. The erodent particle concentration has been varied to the range as 15%, 25%, 35%, and 45% by weight. The rotational speed is tuned to the values as 415, 715, 1015, and 1315 rev/min and the time duration for performing each trail is four hours with consecutive time interval of one hour. L_{16} orthogonal array is used for determining the S/N ratio for each process parameters as shown in **Table 5.3**.

Table 5.2: Control variables and their level of variation.

S. No.	Control variables	Level 1	Level 2	Level 3	Level 4
1	Rotational speed (*N*), rev/min	415	715	1015	1315
2	Concentration (*C*), wt.%	15	25	35	45
3	Particle size (*d*), (µm)	<53	53-106	150-212	212-250

Table 5.3: L_{16} Orthogonal Array and experimental results with different S/N ratios at divergent and varying parameters.

S. No.	Concentration (wt.%)	Particle size (µm)	Rotational speed (rev/min)	SS-304		75%Cr_2O_3+ 25%Al_2O_3 coating		85%Cr_2O_3+ 15%Al_2O_3 coating	
				Weight loss (g)	S/N ratio (negative)	Weight loss (g)	S/N Ratio (negative)	Weight loss (g)	S/N Ratio (negative)
1	15	<53	415	0.00636	43.9309	0.0023	52.7654	0.00160	55.9176
2	15	53-106	715	0.01900	34.4249	0.0068	43.3498	0.00490	46.1961
3	15	150-212	1015	0.07430	22.5802	0.0270	31.3727	0.01980	34.0667
4	15	212-250	1315	0.14910	16.5304	0.0546	25.2561	0.03970	28.0242
5	25	<53	715	0.02010	33.9361	0.0076	42.3837	0.00510	45.8486
6	25	53-106	415	0.01270	37.9239	0.0045	46.9357	0.00310	50.1728
7	25	150-212	1315	0.14750	16.6242	0.0531	25.4981	0.03900	28.1787
8	25	212-250	1015	0.10610	19.4857	0.0393	28.1121	0.02840	30.9336
9	35	<53	1015	0.08690	21.2196	0.0317	29.9788	0.02270	32.8795
10	35	53-106	1315	0.11040	19.1406	0.0413	27.6810	0.02950	30.6036
11	35	150-212	415	0.04130	27.6810	0.0148	36.5948	0.01120	39.0156
12	35	212-250	715	0.08790	21.1202	0.0327	29.7090	0.02390	32.4320
13	45	<53	1315	0.11610	18.7034	0.0456	26.8207	0.03100	30.1728
14	45	53-106	1015	0.10320	19.7264	0.0378	28.4502	0.02800	31.0568
15	45	150-212	715	0.06780	23.3754	0.0252	31.9720	0.01852	34.6472
16	45	212-250	415	0.06480	23.7685	0.0237	32.5050	0.01770	35.0405

5.3 EFFECT OF S/N RATIOS

For each level of parameters taken into consideration in reference for the erosion wear, the arithmetic mean of S/N ratio is calculated and has shown in **Table 5.4−5.6**. On the essence of the results of S/N ratios it is possible to determine the effect of most dominating parameters of the erosion wear. The S/N ratio values were used to evaluate the delta value for each individual factor as shown in **Table 5.4−5.6** for uncoated and coated SS-304. The smaller-the-better characteristic of S/N ratios served as the basis for the rank and delta values for the coated and the uncoated samples. **Table 5.4−5.6** provides a summary of the response table for various S/N ratios for erosion wear for uncoated and coated steel and the main effect plot for S/N ratios for uncoated and coated steel has been shown in **Figure 5.3−5.5**.

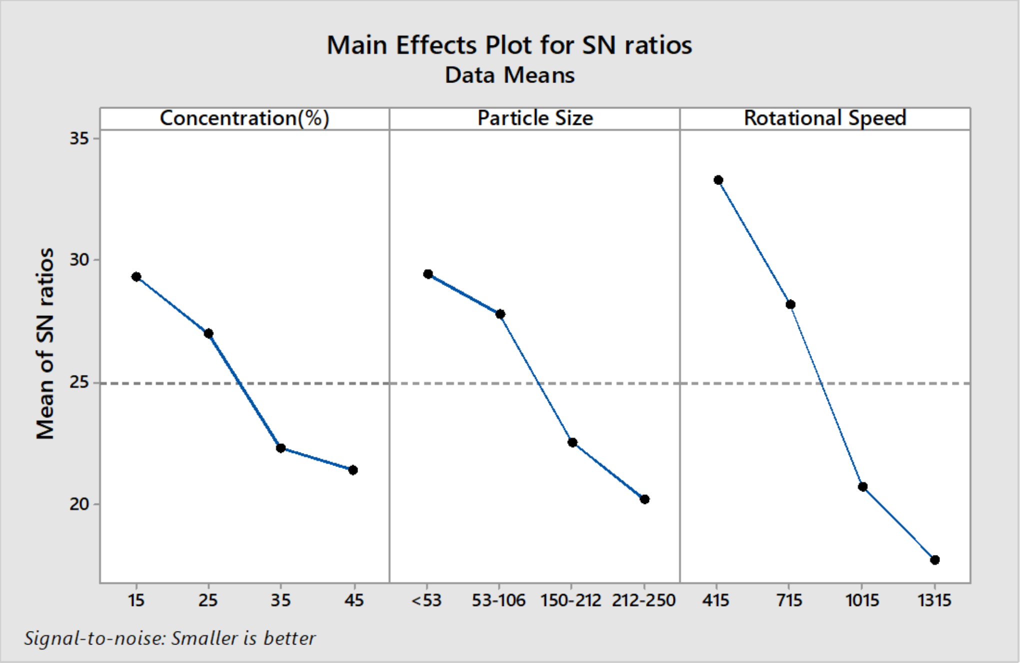

Figure 5.3. Main effects of S/N ratios for concentration, particle size and rotational speed for uncoated SS-304. (Means of S/N ratios are negative)

Table 5.4: Response table for means of signal to noise ratios for uncoated SS-304 steel.

Control Parameters	Level 1	Level 2	Level 3	Level 4	Delta	Rank
Concentration (wt. %)	29.37	26.99	22.29	21.39	7.97	3
Particle size (µm)	29.45	27.80	22.57	20.23	9.22	2
Rotational speed (rev/min)	33.33	28.21	20.57	17.75	15.58	1

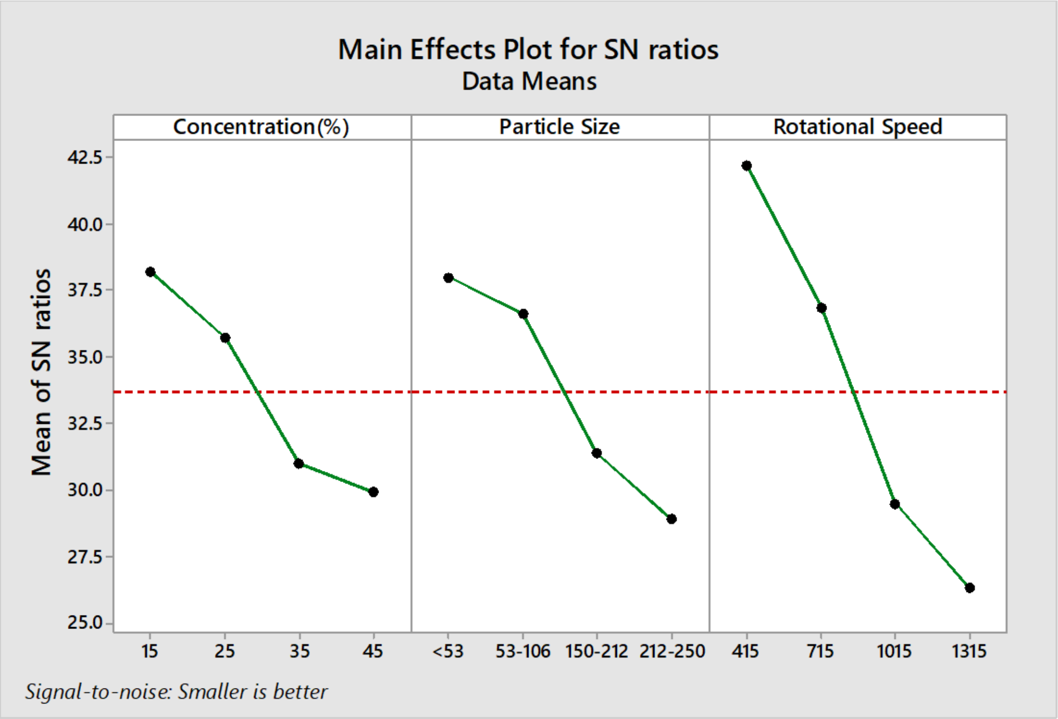

Figure 5.4. Main effect of S/N ratios for concentration, particle size and rotational speed for coated 75%Cr_2O_3+25%Al_2O_3. (Means of S/N ratios are negative)

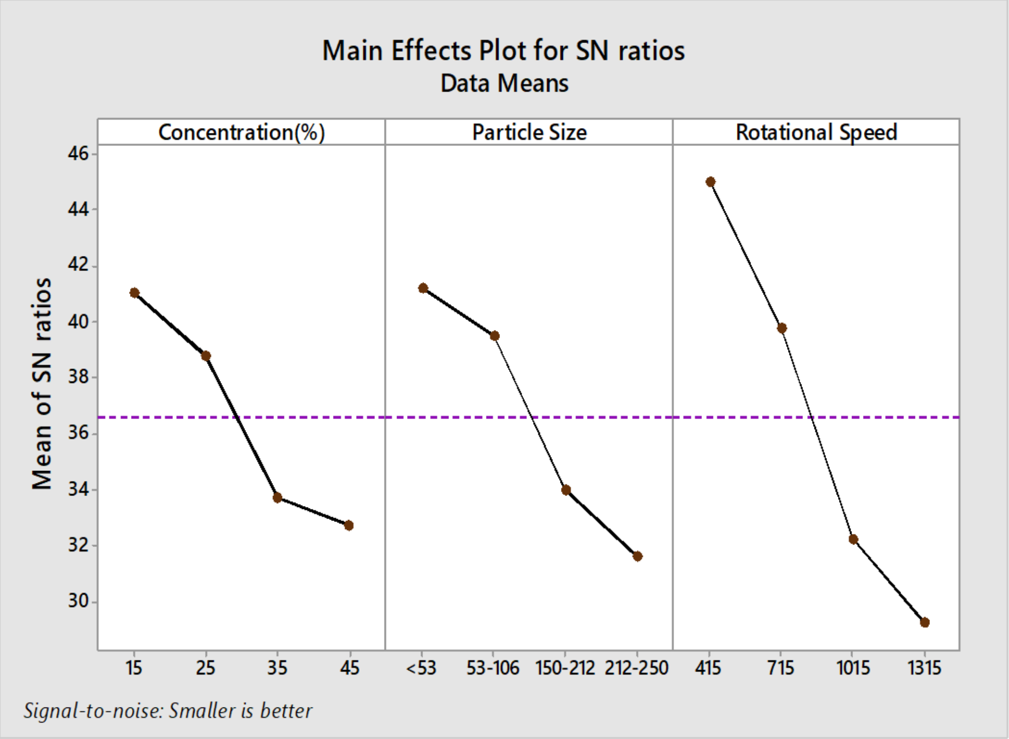

Figure 5.5. Main effect of S/N Ratios for concentration, particle size and rotational speed for coated 85%Cr_2O_3+15%Al_2O_3. (Means of S/N ratios are negative)

Table 5.5: Response table for means of signal to noise ratio for coated 75%Cr_2O_3+25%Al_2O_3

Control Parameters	**Level 1**	**Level 2**	**Level 3**	**Level 4**	**Delta**	**Rank**
Concentration (wt.%)	38.19	35.73	30.99	29.94	8.25	3
Particle size (μm)	37.99	36.60	22.57	31.36	9.09	2
Rotational speed (rev/min)	42.20	36.85	29.48	26.31	15.89	1

Table 5.6: Response table for means of signal to noise ratio for coated 85%Cr_2O_3+15%Al_2O_3

Control Parameters	**Level 1**	**Level 2**	**Level 3**	**Level 4**	**Delta**	**Rank**
Concentration (wt.%)	41.05	38.78	33.73	32.73	8.32	3
Particle size (μm)	41.20	39.51	33.98	31.61	9.60	2
Rotational speed (rev/min)	45.04	39.78	32.23	29.24	15.79	1

5.4 RESPONSE OF DIFFERENT PARAMETERS

From the tables it can be inferred that the value of delta is highest for the rotational speed indicating its greater influence followed by particle size and concentration. As shown in **Tables 5.6−5.8** for uncoated and coated SS-304 the erosion wear of process parameters was used to attain the mean value of erosion wear for each individual factor.

Table 5.7: Response table for mean erosion for concentration for uncoated and coated SS-304.

Concentration (wt.%)	**SS-304**	**75%Cr_2O_3+25%Al_2O_3**	**85%Cr_2O_3+15%Al_2O_3**
Level 1	0.0621	0.0226	0.0165
Level 2	0.0716	0.0261	0.0189
Level 3	0.0816	0.0301	0.0218
Level 4	0.0879	0.0330	0.0238

Table 5.8: Response table for mean erosion for particle size for bare and coated SS-304.

Particle size (μm)	**SS-304**	**75%Cr_2O_3+25%Al_2O_3**	**85%Cr_2O_3+15%Al_2O_3**
Level 1	0.0573	0.0218	0.0151
Level 2	0.0613	0.0226	0.0163
Level 3	0.0827	0.0300	0.0221
Level 4	0.101	0.0375	0.0274

Table 5.9: Response table for mean erosion for rotational speed for bare and coated SS-304.

Rotational speed (rev/min)	**SS-304**	**75%Cr$_2$O$_3$+25%Al$_2$O$_3$**	**85%Cr$_2$O$_3$+15%Al$_2$O$_3$**
Level 1	0.0312	0.0113	0.0084
Level 2	0.0487	0.0180	0.0131
Level 3	0.0926	0.0339	0.0247
Level 4	0.1307	0.0486	0.0348

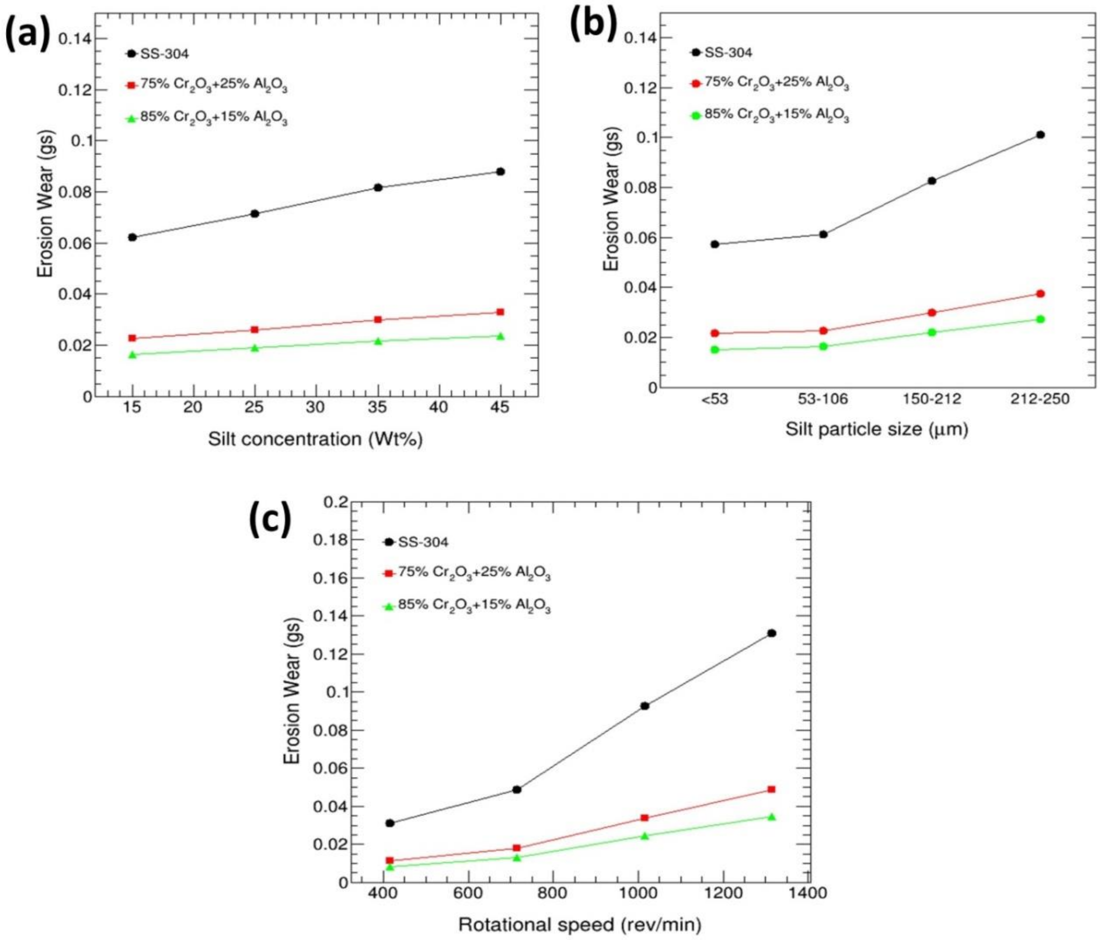

Figure 5.6. Influence of (a) silt concentration, (b) particle size, and (c) rotational speed on mean erosion wear at different levels for uncoated and coated stainless steel.

Figure 5.6(a) shows that the erosion increases with increase in silt concentration (wt.%) as too examined by numerous researchers (Kishor et al., 2018; Sidhu et al., 2007; Singh et al., 2018c). Also, the increase in granular size of silt shows upsurge in erosion for uncoated and coated specimens which is an analogy with the findings of various investigators (Ojala et al., 2016; Vuorinen et al., 2014). Similarly, the erosion shows elevation with escalation in rotational speed as also reported by various authors (Babu et al., 2021; Grewal et al., 2013).

In all the cases it has been analysed that the rotational speed has the most significant effect followed by the particle size and concentration on erosion wear for all uncoated and coated SS-304 samples. Additionally it can be deduced that the least erosion wear for process parameters has occurred at parametric combination of rotational speed (*N*) = 415 rev/min, concentration (*C*) = 15 wt.% and particle size range as <53 μm for uncoated and coated stainless steel shown in **Figure 5.6(a-c)**.

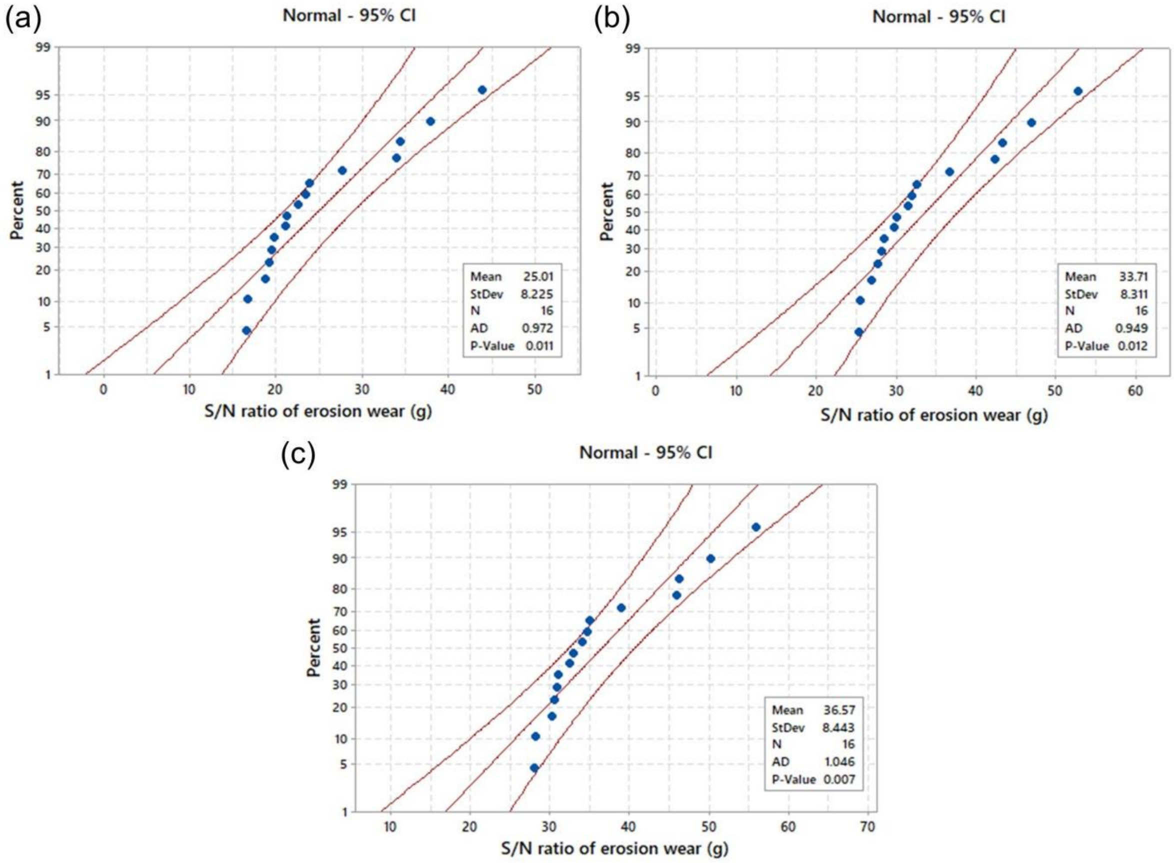

Figure 5.7. Probability plots for erosion of SS-304, 75%Cr_2O_3+25%Al_2O_3 and 85%Cr_2O_3+15%Al_2O_3.

5.5 ANALYSIS OF VARIANCE (ANOVA)

Many researchers used ANOVA to analysis the most significant factor on wear rate for various coatings and materials (Stojanovic et al., 2017; Veličković et al., 2017). ANOVA has been performed so as to determine the significance of each individual parameter on the erosion wear. **Table 5.10** displays the findings of the analysis of variance for S/N ratios for the erosion wear for uncoated SS-304 steel. The contributions of the various parameters were made by using the S/N ratio values. The highest contribution is seen for the factor of rotational speed having value as 59.23%, followed by particle size 22.21% and minimum contribution is seen for the concentration (*C*) as 17.10 for SS-304 as depicted in **Table 5.10**. **Tables 5.11** and **5.12** show the results for the coating 75% Cr_2O_3+25% Al_2O_3 and 85% Cr_2O_3+15% Al_2O_3 coatings respectively. Similarly the contributions obtained for the coating75% Cr_2O_3+25% Al_2O_3 are 59.67 % for rotational speed 21.36% for particle size and 17.66 % for concentration as in **Tables 5.11**. Also, the percentages obtained for coating of composition 85% Cr_2O_3+15% Al_2O_3 are 57.78%, 22.98% and 17.94% for rotational speed, particle size and concentration as shown in **Table 5.12**. The computed R-square values for uncoated SS-304, coated 75%Cr_2O_3+25%Al_2O_3 and 85%Cr_2O_3+15Al_2O_3 are obtained as 98.6%, 98.7% and 98.6% respectively. Probability plots were also drawn for the analysis of level of significance, as illustrated in **Figure 5.7**. It was observed that all data satisfies the 0.95 level of confidence having *p*-value of <0.5.

Table 5.10: ANOVA for S/N ratios for erosion wear of uncoated SS-304.

Source	**Degree of Freedom**	**Sum of Squares**	**Mean Square**	**F-value**	**Contribution (%)**	**Rank**
Concentration	3	173.55	57.848	23.61	17.10	3
Particle Size	3	225.44	75.145	30.67	22.21	2
Rotational Speed	3	601.03	200.345	81.78	59.23	1
Residual Error	6	14.70	2.450	---	1.44	---
Total	15	1014.72	---	---	---	---

Table 5.11: ANOVA for S/N ratios for erosion wear of 75% Cr_2O_3+25% Al_2O_3 coated SS-304.

Source	**Degree of Freedom**	**Sum of Squares**	**Mean Square**	**F ratio**	**Contribution (%)**	**Rank**
Concentration	3	183.02	61.006	27.56	17.66	3
Particle Size	3	221.40	73.832	33.35	21.36	2
Rotational Speed	3	618.29	206.098	93.09	59.67	1
Residual Error	6	13.28	2.214	---	1.28	---
Total	15	1036.09	---	---	---	---

Table 5.12: ANOVA for S/N ratios for erosion wear of 85% Cr_2O_3+15% Al_2O_3 coated SS-304

Source	**Degree of Freedom**	**Sum of Squares**	**Mean Square**	**F ratio**	**Contribution (%)**	**Rank**
Concentration	3	191.92	63.708	26.33	17.94	3
Particle Size	3	245.82	81.941	33.86	22.98	2
Rotational Speed	3	617.81	205.936	85.10	57.78	1
Residual Error	6	14.52	2.420	---	1.35	---
Total	15	1069.28	---	---	---	---

5.6 MECHANISMS OF EROSION

The erosion wear loss which has been observed least for the 85%Cr_2O_3+15Al_2O_3 coating as shown in **Table 5.1** can be attributed to high hardness of the coating (Hutchings and Shipway, 2017). Porosity too has an effect on the erosion behaviour of thermally sprayed coatings as the interlamella strength is affected and responsible for micro cracks for contribution to loss of lamella and hence coating removal (Rajahram et al., 2011). Also the examination of the eroded samples for micro structure characterization has been performed by using SEM. The mechanism of erosion wear is a complicated phenomenon that depends on the kind of material, the speed of the particles as well as their shape and size as examined by many investigators (Desale et al., 2008; Gandhi et al., 1999; Vashishtha et al., 2017). The erosion mechanism of SS-304 has been shown in **Figure 5.8(a)**. The SEM images show the presence of craters, ploughing and microcutting which shows the ductile nature of the material. **Figure 5.8(b, c)** shows the erosion wear process for the coatings of 75%Cr_2O_3+25%Al_2O_3, 85%Cr_2O_3+15Al_2O_3. It involves the presence of craters, microcutting, pits, ploughing and micro-fracture at some positions. However more deep craters have been observed for the 75%Cr_2O_3+25%Al_2O_3 coating as compared to 85%Cr_2O_3+15Al_2O_3 coating which might have caused the more erosion loss for the coating as is evident from the weight loss column. From the experimental analysis it is difficult to determine that the erosion wear of the requisite coatings is mostly brittle.

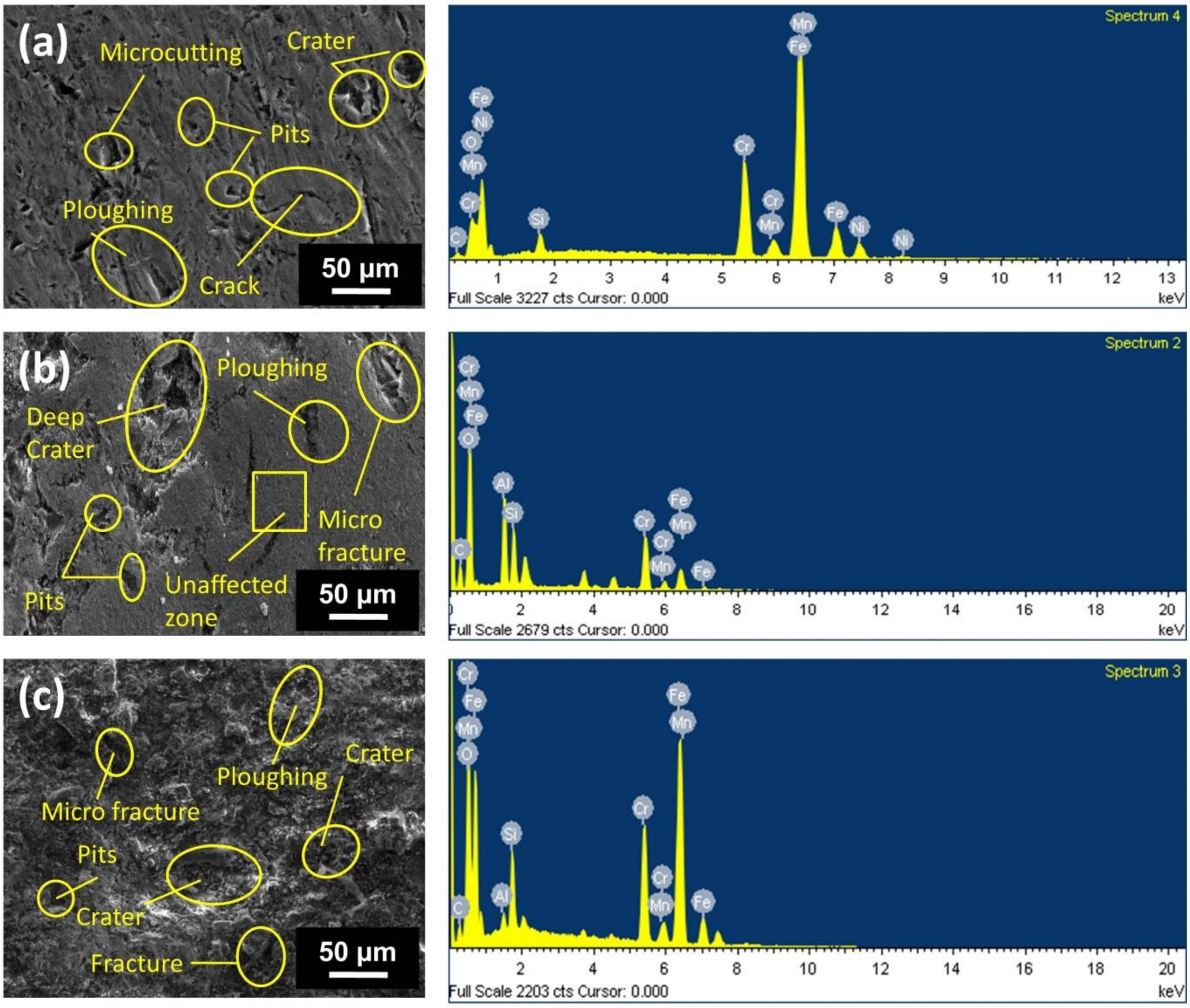

Figure 5.8. Erosion wear mechanism on surfaces of (a) SS-304, (b) 75%Cr_2O_3+25%Al_2O_3, and (c) 85%Cr_2O_3+15Al_2O_3 at (N) = 415 rev/min, concentration (C) of 15% and particle size <53 µm.

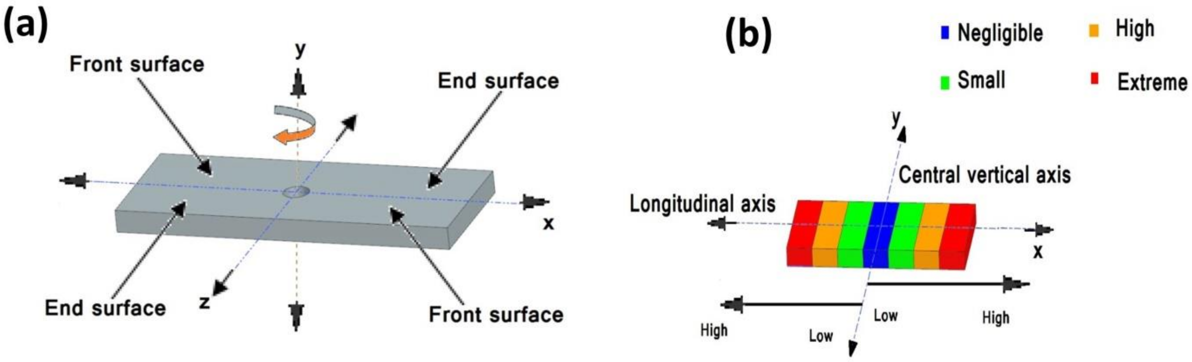

Figure 5.9. Erosion wear occurrence (a) front and end surfaces, and (b) along the longitudinal periphery of workpiece.

Moreover the specimen's erosion wear patterns show that the surfaces closest to the slurry particles erode more quickly than the surfaces that follow them. As, the specimen is rotated through the vertical axis, the occurrence of erosion wear gets changed on the specimen in pot tester in terms of intensity of erosion observed maximum at the utmost radius of the work piece from the central vertical axis, as shown in **Figure 5.9**. Similar investigation has been reported by the author (Singh et al., 2020; Singh, 2021c).

5.7 REMARKS

The influencing parameters such as rotational speed, solid concentration, and particle size were optimized using Taguchi's experimental design. Tribo-erosion performance of uncoated and 75% Cr_2O_3+25% Al_2O_3, 85% Cr_2O_3+15% Al_2O_3 HVOF sprayed coatings on SS-304 were analysed. The following conclusions are drawn on the basis of present investigation:

- From the main effect plots, the least erosion wear for process parameters has occurred at optimal parametric combination of rotational speed (*N*) = 415 rev/min, concentration (*C*) =15 wt.%, and particle size range as <53 µm for uncoated and coated stainless steel .
- The response of rotational speed is ranked ‘1’ which implies the most influential parameter amongst the concentration and particle size.
- The order of tribo-resistance has been observed as 85%Cr_2O_3+15%Al_2O_3 > 75%Cr_2O_3+25%Al_2O_3 > SS-304 which can be attributed to high hardness and low porosity value of the coating.

CHAPTER 6

CONCLUSIONS AND FUTURE SCOPES

It is required to summarize the major results of each aim and to define the scope of subsequent research that needs to be done in this area. This is necessary since the current study consisting of a range of investigations that were carried out. This chapter provides a summary of the overarching findings that may be taken from the on-going inquiry as well as suggestions for the next stage of the project.

6.1 SUMMARY

In the current investigation, silt slurry was used to evaluate the silt erosion of hydro turbine material SS-304 (18Cr10Ni) and various ceramics coatings. Spraying the various coating powders onto the materials of the pump was accomplished by a high-velocity oxy-fuel (HVOF) method. Conventional coatings namely Al_2O_3, Cr_2O_3 and composite coating of composition 55% Cr_2O_3 + 45% Al_2O_3 were deposited on SS-304 using the HVOF process. The HVOF sprayed 55%Cr_2O_3+45%Al_2O_3 coating was further modified into 65% Cr_2O_3+35% Al_2O_3. The conventional 65% Cr_2O_3+35% Al_2O_3 coating was also modified by using Ceria (CeO_2). Therefore, to analyse the effect of the addition of CeO_2 at different concentrations to the composite coatings for studying the silt erosion wear characteristics at different experimental testing parameters as limited literature is available in this context. The percentage of CeO_2 was varied as 0.5, 1.0, and 1.5% in 65% Cr_2O_3+Al_2O_3 coating with the percentage of Al_2O_3 as 34.5, 34, and 33.5% respectively. Experiments on silt erosion were carried out using a slurry pot tester at a variety of rotational speeds of the impeller (rpm), concentrations (wt.%), time durations (hours), and particle sizes (μm) to replicate the circumstances that exist in case of actual hydro turbine.

6.2 ACCOMPLISHMENT OF OBJECTIVES

- The first major objective of this was the characterization of silt erosion which was completed in Chapter 3.
- The second major objective was to analyse the effect of various parameters like rotational speed, solid concentration, and particle size on erosion wear characteristics of different hydro turbine materials and coatings which has been covered in Chapter 4.

- The last objective of this work was the optimization of various influencing parameters for erosion wear using the design of experiments which is also covered in Chapter 5.

6.3 CONCLUSIONS

The findings that were reported in the other chapters were used to draw the conclusions that are included in this section. From the experimental results and examination of microstructures of coated and uncoated SS-304 steel samples before and after experimentation the following conclusions are made:

1. All of the testing parameters including rotational speed, silt concentration, and particle size have a significant impact on the silt erosion performance of different coated and uncoated samples. As rotational speed, silt slurry concentration, and silt particle size increases, silt erosion in coated and bare samples increases significantly. As time progressed the cummutative weight loss tends to increase but the erosion rate is found to be decreased.
2. The HVOF sprayed Cr_2O_3, Al_2O_3, and 45% Al_2O_3+55%Cr_2O_3 coatings perform better surface resistance as compared to uncoated SS-304.
3. Out of all the HVOF coatings Cr_2O_3 coated substrate has the highest resistance to silt erosion at all the particle size range for a particular silt concentration, at specific rotational speeds for specific time durations.
4. The Cr_2O_3 coated substrate has a denser laminar structure as obtained from SEM micrographs and also due to its higher hardness and low porosity value shows a more positive response to an increase in its resistance to silt erosion.
5. The Cr_2O_3, Al_2O_3 and 45% Al_2O_3+55%Cr_2O_3 HVOF coatings considerably increased the micro hardness of SS-304 steel which proved to be a beneficial mechanical property for decreasing the erosion wear by silt slurry steering conditions.
6. For HVOF coated and uncoated substrates the following order of erosion resistance is observed as Cr_2O_3>45% Al_2O_3+55%Cr_2O_3 > Al_2O_3> SS-304
7. The composite coating has shown enhanced resistance to erosion wear as compared to Al_2O_3 coating for all testing conditions for silt slurry and at all testing parameters. This may be attributed to the increase in cohesive strength of Al_2O_3 by the addition of Cr_2O_3 which act as a density enhancer and binder for Al_2O_3.
8. The Cr_2O_3 has high hardness and low porosity values, tough matrix, and higher hardness resist the impact of silt. This can be attributed to more increase in resistance to erosion wear by the coating.

9. For comparison of coated and uncoated SS-304, the following order of erosion resistance was observed as 65% Cr_2O_3+34.5% Al_2O_3+0.5% CeO_2 > 65% Cr_2O_3+34% Al_2O_3+1% CeO_2 > 65% Cr_2O_3+35% Al_2O_3 > 65% Cr_2O_3+33.5% Al_2O_3+1.5% CeO_2 > SS-304.
10. The 0.5% CeO_2 addition to the HVOF sprayed Cr_2O_3+Al_2O_3 coatings has better resistance and low wear rate to silt slurry erosion as compared to the other developed HVOF coatings in the study which may be attributed to a significant increase in hardness and low porosity values when compared with other coatings. The deposited ceramics coatings aim as a viable option for increasing the wear resistance of hydro turbine components.
11. The major mechanism of material removal is spalling of Al_2O_3 and craters however eroded Al_2O_3 coating also shows the ploughing, cracks and craters for smaller sizes particles.
12. SEM micrograph of eroded 65%Cr_2O_3+33.5%Al_2O_3+1.5%CeO_2 depicts that the severity of erosion is more as the eroded ploughing region has been spread to the larger surface area compared to other 0, 0.5 and 1.0% CeO_2 added coating.
13. The examination of the eroded samples reveals that the size and depth of craters and ploughing increase predominantly as the range of the silt size particles for erosion increases from 150-212 µm to 212-250 µm.
14. From design of experiments, it has been analysed that among the three operating parameters such as rotational speed, solid concentration, and particle size; rotational speed is the dominant parameter affecting the erosion wear.

6.4 FUTURE SCOPE

This research has the potential to be expanded to investigate the endurance of cermet and metal composite coatings in a variety of environments. It would be in everyone's best interest to further expand the knowledge base by carrying out further research on the following subjects:

- Studies on the deterioration and wear of Cr_2O_3, Al_2O_3, and CeO_2-based coatings in different environments, such as applications involving salt water.
- An investigation of the erosion and corrosion of coatings made of CeO_2-added coatings brought on by the acidic nature of slurry.
- Investigations into the effects of erosion and abrasion were expanded as part of the research on ceramics coatings. The impellers, blades, runner, and guide vanes of hydro turbine are prone to erosion and abrasion over time. The life of hydro turbine may be

improved by conducting an erosion-abrasion study on a variety of innovative materials for use in the construction of hydro turbine components.

- An investigation for comparison of HVOF sprayed ceramic coatings with other coating deposition processes.
- Research should be expanded to include lower impact angles and greater velocities, as well as a broader range of impact velocities and solid concentrations under varying environmental conditions.
- To construct a numerical simulation tool, it is necessary to do CFD analysis on the various coatings used in the pot tester. Both time and money will be saved as a result of this improvement to the in-situ testing process.

LIST OF PUBLICATIONS

SCI/SCIE Indexed Publications (02)

1) Rajesh Kumar*, Satish Kumar, Deepa Mudgal, Silt erosion performance of high-velocity oxy-fuel (HVOF) sprayed Al_2O_3–Cr_2O_3 composite coatings on turbine steel. *Industrial Lubrication and Tribology* 2022, 74(5), pp. 572–579. https://doi.org/10.1108/ILT-08-2021-0346
2) Rajesh Kumar*, Satish Kumar, Deepa Mudgal, Deposition of Al_2O_3/Cr_2O_3 ceramics HVOF sprayed coatings for protection against silt erosion. *Surface Review and Letters* 2023, p. 2240008. https://doi.org/10.1142/S0218625X2240008X

Scopus Indexed Publication (01)

3) Rajesh Kumar*, Satish Kumar, Deepa Mudgal, Performance analysis of bare SS-304 using silt of size 350-450 μm at varying speed and at particular silt concentration. *AIP Conference Proceedings* 2021, 2341, p. 030037. https://doi.org/10.1063/5.0050223

Conference Proceedings Paper (01)

4) Rajesh Kumar*, Satish Kumar, Deepa Mudgal, Effect of multi sized silt for analyzing the erosion wear mechanism on 13Cr-4Ni steel. *Research Retrieval and Academic Letters* 2023, 02, pp. 244-247. https://doi.org/10.5281/zenodo.7935257

Conference Presentations (02)

1) Presented paper (S. No. 03) entitled "Performance Analysis of Bare SS-304 using silt of size 350-450 Micron meter at varying speed and at particular silt concentration" in the "National conference on materials, mechanics and modeling (NCMMM-2020)" organized by *Department of Mechanical Engineering, National Institute of Technology Jamshedpur, Jharkhand (India)* held during 29-30th August 2020.
2) Presented paper (S. No. 04) entitled "Effect of multi sized silt for analyzing the erosion wear mechanism on 13Cr-4Ni steel" in the *2nd international Scientific conference research retrieval and academic letters, Warsaw (Poland)* held during 11-12th May 2023.

REFERENCES

Agarwal, N., Chaudhari, G.P., Nath, S.K., 2014. Slurry and cavitation erosion of HSLA steel processed by warm multidirectional forging and inter-critical annealing. Tribol. Int. 70, 18–25.

Ahmed, R., 2002. Contact fatigue failure modes of HVOF coatings. Wear 253, 473–487.

Al-Bukhaiti, M.A., Abouel-Kasem, A., Emara, K.M., Ahmed, S.M., 2016. Particle shape and size effects on slurry erosion of AISI 5117 steels. J. Tribol. 138, 24503.

Al-Fadhli, H.Y., Stokes, J., Hashmi, M.S.J., Yilbas, B.S., 2006. The erosion–corrosion behaviour of high velocity oxy-fuel (HVOF) thermally sprayed inconel-625 coatings on different metallic surfaces. Surf. Coatings Technol. 200, 5782–5788.

Alam, T., Aminul Islam, M., Farhat, Z.N., 2016. Slurry erosion of pipeline steel: effect of velocity and microstructure. J. Tribol. 138, 21604.

Amarendra, H.J., Chaudhari, G.P., Nath, S.K., 2012. Synergy of cavitation and slurry erosion in the slurry pot tester. Wear 290, 25–31.

Arji, R., Dwivedi, D.K., Gupta, S.R., 2009. Some studies on slurry erosion of flame sprayed Ni-Cr-Si-B coating. Ind. Lubr. Tribol.

ASTM-G76-95, 2000. Standard test method for conducting erosion tests by solid particle impingement using gas jets. ASTM Int.

Awal, R., Chitrakar, S., Thapa, B.S., Neopane, H.P., 2019. Analysis A General Review on Methods of Sediment Sampling and Mineral Content Analysis. J. Phys. Conf. Ser 1266, 012005.

Babu, A., Arora, H.S., Singh, R.P., Grewal, H.S., 2021. Slurry Erosion Resistance of Microwave Derived Ni-SiC Composite Claddings. Silicon.

Bahadur, S., Badruddin, R., 1990. Erodent particle characterization and the effect of particle size and shape on erosion. Wear 138, 189–208.

Bajracharya, T.R., Acharya, B., Joshi, C.B., Saini, R.P., Dahlhaug, O.G., 2008a. Sand erosion of Pelton turbine nozzles and buckets: A case study of Chilime Hydropower Plant. Wear 264, 177–184.

Bajracharya, T.R., Acharya, B., Joshi, C.B., Saini, R.P., Dahlhaug, O.G., 2008b. Sand erosion of Pelton turbine nozzles and buckets: A case study of Chilime Hydropower Plant. Wear 264, 177–184.

Bartosik, A., 2010. Influence of Coarse-Dispersive Solid Phase on The “Particles-Wall”

Shear Stress in Turbulent Slurry Flow with High Solid Concentration. Arch. Mech. Eng. 57, 45–68.

Bellman, R., Levy, A., 1981. Erosion mechanism in ductile metals. Wear 70, 1–27.

Bong, E.Y., Eshtiaghi, N., Wu, J. and Parthasarathy, R., 2015. Optimum solids concentration for solids suspension and solid–liquid mass transfer in agitated vessels. Chem. Eng. Res. Des., 100, 148-156..

Bouwman, A.M., Bosma, J.C., Vonk, P., Wesselingh, J.A., Frijlink, H.W., 2004. Which shape factor(s) best describe granules? Powder Technol. 146, 66–72.

Brunetti, C., Belotti, L.P., Miyoshi, M.H., Pintaúde, G. and D'Oliveira, A.S.C.M., 2014. Influence of Fe on the room and high-temperature sliding wear of NiAl coatings. Surf. Coat. Technol. 258, 160-167.

Buszko, M., Krella, A., 2017. Slurry erosion-design of test devices. Adv. Mater. Sci. 17, 5–17.

Chandel, S., Singh, S.N., Seshadri, V., 2012. Experimental study of erosion wear in a centrifugal slurry pump using coriolis wear test rig. Part. Sci. Technol. 30, 179–195.

Chauhan, A.K., Goel, D.B., Prakash, S., 2008. Erosion behaviour of hydro turbine steels. Bull. Mater. Sci. 31, 115–120.

Chávez, J.C., Valencia, J.A., Jaramillo, G.A., Coronado, J.J. and Rodríguez, S.A., 2015. Failure analysis of a Pelton impeller. Eng. Fail. Anal. 48, 297-307.

Chitrakar, S., Dahlhaug, O.G., Neopane, H.P., 2018. Numerical investigation of the effect of leakage flow through erosion-induced clearance gaps of guide vanes on the performance of francis turbines. Eng. Appl. Comput. Fluid Mech. 12, 662–678.

Chitrakar, S., Neopane, H.P., Dahlhaug, O.G., 2016. Study of the simultaneous effects of secondary flow and sediment erosion in Francis turbines. Renew. Energy 97, 881–891.

Clark, H.M., 1991. On the impact rate and impact energy of particles in a slurry pot erosion tester. Wear 147, 165–183.

Clark, H.M., 1993. Specimen diameter, impact velocity, erosion rate and particle density in a slurry pot erosion tester. Wear 162, 669–678.

Clark, H.M., Hawthorne, H.M., Xie, Y., 1999. Wear rates and specific energies of some ceramic, cermet and metallic coatings determined in the Coriolis erosion tester. Wear 233, 319–327.

Clark, H.M.I., Wong, K.K., 1995. Impact angle, particle energy and mass loss in erosion by dilute slurries. Wear 186–187, 454–464.

Crawner, D., 2004. Thermal Spray Processes, Handbook of Thermal Spray Technology, J.

Int. ASM.

Dabirian, R., Mohan, R., Shoham, O., Kouba, G., 2016. Critical sand deposition velocity for gas-liquid stratified flow in horizontal pipes. J. Nat. Gas Sci. Eng. 33, 527–537.

Dasgupta, R., Prasad, B.K., Jha, A.K., Modi, O.P., S., D., Yegneswaran, A.H., 1998. Effects of sand concentration on slurry erosion of steels. Mater. Transections 39, 1185–1190.

Datta, P.K., Gray, J.S., 1993. Volume II: Engineering Applications.

Davis, J.R., 2004. Handbook of Thermal Spray Technology. ASM International, Materials Park, OH, U.S.A.

Desale, G.R., Gandhi, B.K., Jain, S.C., 2005. Improvement in the design of a pot tester to simulate erosion wear due to solid-liquid mixture. Wear 259, 196–202.

Desale, G.R., Gandhi, B.K., Jain, S.C., 2006. Effect of erodent properties on erosion wear of ductile type materials. Wear 261, 914–921.

Desale, G.R., Gandhi, B.K., Jain, S.C., 2008. Slurry erosion of ductile materials under normal impact condition. Wear 264, 322–330.

Desale, G.R., Gandhi, B.K., Jain, S.C., 2011. Development of correlations for predicting the slurry erosion of ductile materials. J. Tribol. 133, 1–10.

Din, M.Z.U. and Harmain, G.A., 2020. Assessment of erosive wear of Pelton turbine injector: Nozzle and spear combination–A study of Chenani hydro-power plant. Engineering Failure Analysis, 116, p.104695.

Divakar, M., Agarwal, V.K., Singh, S.N., 2005. Effect of the material surface hardness on the erosion of AISI316. Wear 259, 110–117.

Dong, S., Song, B., Hansz, B., Liao, H., Coddet, C., 2013. Improvement in the microstructure and property of plasma sprayed metallic, alloy and ceramic coatings by pre-/during-treatment of dry-ice blasting. Surf. Coatings Technol. 220, 199–203.

Edlmayr, V., Moser, M., Walter, C., Mitterer, C., 2010. Thermal stability of sputtered Al_2O_3 coatings. Surf. Coatings Technol. 204, 1576–1581.

Elkholy, A., 1983. Prediction of abrasion wear for slurry pump materials. Wear 84, 39–49.

Elkholy, Ahmed, 1983. Prediction of abrasion wear for slurry pump materials. Wear 84, 39–49.

Evans, A.G., Gulden, M.E., Rosenblatt, M., 1978. Impact damage in brittle materials in the elastic-plastic response regime. Proc. R. Soc. Lond. A. 361, 343–365.

Fauchais, P., Vardelle, A., 2012. Thermal sprayed coatings used against corrosion and corrosive wear. Adv. plasma spray Appl. 10, 34448.

Fecarotta, O., Messa, G.V., Pugliese, F., Carravetta, A., Malavasi, S., Giugni, M., 2018.

Preliminary Development of a Method for Impact Erosion Prediction in Pumps Running as Turbines. In: EWaS3 2018. MDPI, Basel Switzerland, p. 680.

Finne, I., 1960. Erosion of surfaces. Wear 3, 87–103.

Fraenkel, P., Paish, O., Bokalders, V., Harvey, A., Brown, A., Edwards, R., 1991. Micro-hydro Power. Intermed. Technol.

Gautam, S., Neopane H.P., Acharya N., Chitrakar S., Thapa B.S., and Zhu B. 2020. Sediment erosion in low specific speed francis turbines: A case study on effects and causes. Wear 442, p. 203152.

Gallani, G.R., Dalfre Filho, J.G., de Lima Branco, R., Malavasi, S., 2018. Equipment to avaliate erosion caused by water-solid mix on hydraulic surfaces. Rev. dos Trab. Iniciação Científica da UNICAMP.

Gandhi, B.K., Singh, S.N., Seshadri, V., 1999. Study of the parametric dependence of erosion wear for the parallel flow of solid-liquid mixtures. Tribol. Int. 32, 275–282.

Gandhi, B.K., Singh, S.N., Seshadri, V., 2003. A study on the effect of surface orientation on erosion wear of flat specimens moving in a solid-liquid suspension. Wear 254, 1233–1238.

Goel, D.B., Sharma, M.K., 1996. Present state of damages and their repair welding in Indian hydroelectric projects. In: Proc. Silt Damages to Equipment in Hydro Power Stations and Remedial Measures. New Delhi, India, pp. 137–152.

Goyal, D.K., Singh, H., Kumar, H., Sahni, V., 2012. Slurry erosive wear evaluation of HVOF-spray Cr_2O_3 coating on some turbine steels. J. Therm. Spray Technol. 21, 838–851.

Goyal, K., 2018. Experimental investigations of mechanical properties and slurry erosion behaviour of high velocity oxy fuel and plasma sprayed Cr_2O_3–50%Al_2O_3 coatings on CA6NM turbine steel under hydro accelerated conditions. Tribol. - Mater. Surfaces Interfaces 12, 97–106.

Grewal, H.S., Agrawal, A., Singh, H., 2013. Design and development of high-velocity slurry erosion test rig using CFD. J. Mater. Eng. Perform. 22, 152–161.

Grewal, H.S., Agrawal, A., Singh, H., 2013. Design and development of high-velocity slurry erosion test rig using CFD. J. Mater. Eng. Perform. 22, 152–161.

Grewal, H.S., Arora, H.S., Agrawal, A., Singh, H., Mukherjee, S., 2013. Slurry erosion of thermal spray coatings: Effect of sand concentration. Procedia Eng. 68, 484–490.

Grewal, H S, Arora, H.S., Singh, H., Agrawal, A., 2013a. Surface modification of hydroturbine steel using friction stir processing. Appl. Surf. Sci. 268, 547–555.

Grewal, H.S., Bhandari, S., Singh, H., 2012. Parametric study of slurry-erosion of hydroturbine steels with and without detonation gun spray coatings using taguchi technique. Metall. Mater. Trans. A 43, 3387–3401.

Grewal, H S, Singh, H., Agrawal, A., 2013b. Microstructural and mechanical characterization of thermal sprayed nickel–alumina composite coatings. Surf. coatings Technol. 216, 78–92.

Gupta, Rajat, Singh, S.N., Sehadri, V., 1995. Prediction of uneven wear in a slurry pipeline on the basis of measurements in a pot tester. Wear 184, 169–178.

Gupta, R., Singh, S.N., Seshadri, V., 1995. Study on the uneven wear rate in a slurry pipeline on the basis of mesurements in a pot tester. Wear 184, 169–178.

Hawthorne, H.M., 2002. Some Coriolis slurry erosion test developments. Tribol. Int. 35, 625–630.

Hearley, J.A., Little, J.A., Sturgeon, A.J., 1999. The erosion behaviour of NiAl intermetallic coatings produced by high velocity oxy-fuel thermal spraying. Wear 233, 328–333.

Heilbronner, R., Keulen, N., 2006. Grain size and grain shape analysis of fault rocks. Tectonophysics 427, 199–216.

Hentschel, M.L., Page, N.W., 2003. Selection of descriptors for particle shape characterization. Part. Syst. Charact. 20, 25–38.

Hong, S., Wu, Y., Wang, Q., Ying, G., Li, G., Gao, W., Wang, B., Guo, W., 2013. Microstructure and cavitation–silt erosion behavior of high-velocity oxygen–fuel (HVOF) sprayed Cr_3C_2–NiCr coating. Surf. Coatings Technol. 225, 85–91.

Hu, H.X., Guo, X.M., Zheng, Y.G., 2019. Comparison of the cavitation erosion and slurry erosion behavior of cobalt-based and nickel-based coatings. Wear 428, 246–257.

Hutchings, I., Shipway, P., 2017. Tribology: friction and wear of engineering materials. Butterworth-Heinemann.

International Energy Agency report (IEA), 2019. World Energy Outlook 2019. Paris. https://www.iea.org/reports/world-energy-outlook-2019

Islam, M.A., Alam, T., Farhat, Z.N., Mohamed, A., Alfantazi, A., 2015. Effect of microstructure on the erosion behavior of carbon steel. Wear 332–333, 1080–1089.

Islam, M.A., Farhat, Z.N., 2014. Effect of impact angle and velocity on erosion of API X42 pipeline steel under high abrasive feed rate. Wear 311, 180–190.

Iwai, Y., Miyajima, T., Mizuno, A., Honda, T., Itou, T., Hogmark, S., 2009. Micro-Slurry-jet Erosion (MSE) testing of CVD TiC/TiN and TiC coatings. Wear 267, 264–269.

Jain, A.., 1999. Silting problems in hydropower projects: Indian scenario. In: Proc. of 1st Int.

Conf. on Silting Problems in Hydro Power Plants. New Delhi, India, pp. 37–54.

Jonda, E., Szala, M., Sroka, M., Łatka, L., Walczak, M., 2023. Investigations of cavitation erosion and wear resistance of cermet coatings manufactured by HVOF spraying. Appl. Surf. Sci. 608, 155071.

Kapali, A., Chitrakar, S., Shrestha, O., Neopane, H.P., Thapa, B.S., 2019. A Review on Experimental Study of Sediment Erosion in Hydraulic Turbines at Laboratory Conditions. J. Phys. Conf. Ser. 1266.

Khurana, S., Varun, & Kumar, A. 2016. Silt erosion study on the performance of an impulse turbine in small hydropower. Int. J. Amb. Energ. 37(5), 520–527.

Karafyllias, G., Galloway, A., Humphries, E., 2019. The effect of low pH in erosion-corrosion resistance of high chromium cast irons and stainless steels. Wear 420–421, 79–86.

Karandikar, D.A., 2015. HVOF coatings to combat hydro abrasive erosion. In: Int. Conf. Hydropower Sustain. Dev. Dehradun, India, pp. 171–179.

Kishor, B., Chaudhari, G.P., Nath, S.K., 2014. Cavitation erosion of thermomechanically processed 13/4 martensitic stainless steel. Wear 319, 150–159.

Kishor, B., Chaudhari, G.P., Nath, S.K., 2016. Slurry erosion of thermo-mechanically processed 13Cr4Ni stainless steel. Tribol. Int. 93, 50–57.

Kishor, B., Chaudhari, G.P., Nath, S.K., 2018. Slurry erosion behaviour of thermomechanically treated 16Cr5Ni stainless steel. Tribol. Int. 119, 411–418.

Kjolle, A., 2014. No Title. Trondheim, Norway.

Kleis, I., Kulu, P., 2008. Influence of Particle Concentration. In: Solid Particle Erosion. Springer-Verlag London Limited, pp. 24–27.

Kumar, K., and Saini, R. P. 2022. Development of correlation to predict the efficiency of a hydro machine under different operating conditions. Sustain. Energ. Technol. Assess. 50, p. 101859.

Kumar, P., Kumar, S., Singh, V., Ratha, D., 2022. Surface erosion performance of Yttrium oxide blended WC-12Co thermally sprayed coating for mild steel. Surf. Rev. Lett.

Łatka, L., Szala, M., Nowakowska, M., Walczak, M., Kiełczawa, T., Sokołowski, P., 2023. The effect of microstructure and mechanical properties on sliding wear and cavitation erosion of plasma coatings sprayed from Al_2O_3 + 40 wt% TiO_2 agglomerated powders. Surf. Coatings Technol. 455, 129180.

Levy, A., Hickey, G., 2010. Surface degradation of metals in simulated synthetic fuels plant environments. California, USA.

Levy, A. V., Chik, P., 1983. The effects of erodent composition and shape on the erosion of steel. Wear 89, 151–162.

Levy, A. V, 1996. Solid Particle Erosion and Erosion-Corrosion of Materials, ASM International. ASM International, Ohio.

Li, H., Khor, K.A., Cheang, P., 2002. Titanium dioxide reinforced hydroxyapatite coatings deposited by high velocity oxy-fuel (HVOF) spray. Biomaterials 23, 85–91.

Liu, S.L., Zheng, X.P., Geng, G.Q., 2010. Influence of nano-WC-12Co powder addition in WC-10Co-4Cr AC-HVAF sprayed coatings on wear and erosion behaviour. Wear 269, 362–367.

Malavasi, S., Messa, G.V., Negri, M., 2018. Prediction of Erosion Damage in a Choke Valve Working in Severe Slurry Conditions. In: Pressure Vessels and Piping Conference. American Society of Mechanical Engineers, p. V007T07A022.

Manisekaran, T., Kamaraj, M., Sharrif, S.M., Joshi, S. V., 2007. Slurry erosion studies on surface modified 13Cr-4Ni steels: Effect of angle of impingement and particle size. J. Mater. Eng. Perform. 16, 567–572.

Mann, B.S., 1999. An experimental study to determine the effects of low and high-energy particle impact on the erosion of hydraulic turbine material and protective hard coating.

Mann, B.S., 2000. High-energy particle impact wear resistance of hard coatings and their application in hydroturbines. Wear 237, 140–146.

Mansouri, A., Arabnejad, H., Karimi, S., Shirazi, S.A., McLaury, B.S., 2015. Improved CFD modeling and validation of erosion damage due to fine sand particles. Wear 338–339, 339–350.

Mansouri, A., Shirazi, S.A., McLaury, B.S., 2014. Experimental and numerical investigation of the effect of viscosity and particle size on the erosion damage caused by solid particles. In: Fluids Engineering Division Summer Meeting. American Society of Mechanical Engineers, p. V01DT31A002.

Maruszczyk, A., Dudek, A., Szala, M., 2017. Research into morphology and properties of TiO2–NiAl atmospheric plasma sprayed coating. Adv. Sci. Technol. Res. J. 11, 204–210.

Messa, G. V, Malavasi, S., Zhang, J., Shirazi, S.A., 2019. Numerical prediction of the impact erosion produced by dense slurry jets. In: 19th International Conference on Transport & Sedimentation of Solid, South Africa.

Ministry of Power report, 2019. https://powermin.nic.in/sites/default/files/uploads/MOP_Annual_Report_Eng_2018-

19.pdf%0A

Mittal, G., Donga, R., Kumar, A. and Karn, A., 2019, Identification of Silt Erosion Areas on Francis Turbine Guide Vanes Through Numerical Simulation. In Proceedings of 46th National Conference on Fluid Mechanics and Fluid Power (FMFP).

Naidu, B.S., 1997. Addressing the problems of silt erosion at hydro plants. Int. J. Hydropower Dams. 4, 72–77.

Nayak, S.K., Satapathy, A., Mantry, S., Besra, L., 2022. Erosion Response of High-Velocity Oxy-Fuel Sprayed Marble Dust-NiCr Coatings. Trans. Indian Ceram. Soc. 81, 149–157.

Nayak, S.K., Satapathy, A., Mantry, S., Besra, L., 2023. Deposition of Coatings of Waste Marble Dust Pre-Mixed with Nickel Chrome Powder by High-Velocity Oxy-Fuel Spraying Route. JOM 1–12.

Neopane, H.P., Chitrakar, S., Dahlhaug, O.G., 2019. Role of Turbine Testing Lab for overcoming the challenges related to hydropower development in Nepal. IOP Conf. Ser. Earth Environ. Sci. 240.

Nowakowska, M., Łatka, L., Sokołowski, P., Szala, M., Toma, F.-L., Walczak, M., 2022. Investigation into microstructure and mechanical properties effects on sliding wear and cavitation erosion of Al_2O_3–TiO_2 coatings sprayed by APS, SPS and S-HVOF. Wear 508–509, 204462.

Ojala, N., Valtonen, K., Antikainen, A., Kemppainen, A., Minkkinen, J., Oja, O., Kuokkala, V.T., 2016. Wear performance of quenched wear resistant steels in abrasive slurry erosion. Wear 354–355, 21–31.

Oka, Y.I., Okamura, K., Yoshida, T., 2005. Practical estimation of erosion damage caused by solid particle impact: Part 1: Effects of impact parameters on a predictive equation. Wear 259, 95–101.

Padhy, M.K., Saini, R.P., 2009. Effect of size and concentration of silt particles on erosion of Pelton turbine buckets. Energy 34, 1477–1483.

Padhy, M.K., Saini, R.P., 2012. Study of silt erosion mechanism in Pelton turbine buckets. Energy 39, 286–293.

Peña Ballesteros, D.Y., Mendez Camacho, Y.E., Barreto Hernandez, L.V., 2016. Evaluation of the Synergistic Effect of Erosion-Corrosion on AISI 4330 Steel in Saline-Sand Multiphase Flow by Electrochemical and Gravimetric Techniques. Int. J. Electrochem. 2016, 1–7.

Pintaude, G., Bernardes, F.G., Santos, M.M., Sinatora, A. and Albertin, E., 2009. Mild and severe wear of steels and cast irons in sliding abrasion. Wear 267(1-4), 19-25.

Pintaude, G., Rovani, A.C., das Neves, J.C.K., Lagoeiro, L.E., Li, X. and Dong, H.S., 2019. Wear and corrosion resistances of active screen plasma-nitrided duplex stainless steels. J. Mater. Eng. Perform. 28, 3673-3682.

Pintaude, G., Tanaka, D.K. and Sinatora, A., 2003. The effects of abrasive particle size on the sliding friction coefficient of steel using a spiral pin-on-disk apparatus. Wear 255(1-6), 55-59.

Prakash, G., Nath, S.K., 2018. Studies on enhancement of silt erosion resistance of 13/4 martensitic stainless steel by low-temperature salt bath nitriding. J. Mater. Eng. Perform. 27, 3206–3216.

Prasad, B.K., Jha, A.K., Modi, O.P., Yegneswaran, A.H., 2004. Effect of sand concentration in the medium and travel distance and speed on the slurry wear response of a zinc-based alloy alumina particle composite. Tribol. Lett. 17, 301–309.

Prasad, B.K., Modi, O.P., 2009. Slurry wear characteristics of zinc-based alloys: Effects of sand content of slurry, silicon addition to alloy system and traversal distance. Trans. Nonferrous Met. Soc. China 19, 277–286.

Prasad, K. V, Hiriyannaiah, A., Keshavamurthy, R., 2022. Investigation on Slurry Erosive Wear Behaviour of HVOF-Sprayed Al_2O_3–CeO_2 Coatings on AZ91 Alloy. J. Inst. Eng. Ser. D 1–15.

Purkayastha, S., Dwivedi, D.K., 2012. Effect of CeO_2 on the friction and sliding wear performance of Ni/WC coatings. In: International Conference on Advances in Electrical And Mechanical Engineering Phuket Thailand. pp. 18–19.

Rai, A. K., Kumar, A., & Staubli, T. 2020. Effect of concentration and size of sediments on hydro-abrasive erosion of Pelton turbine. Renew. Energ. 145, 893-902.

Rajahram, S.S., Harvey, T.J., Wood, R.J.K., 2009. Erosion-corrosion resistance of engineering materials in various test conditions. Wear 267, 244–254.

Rajahram, S.S., Harvey, T.J., Wood, R.J.K., 2011. Electrochemical investigation of erosion-corrosion using a slurry pot erosion tester. Tribol. Int. 44, 232–240.

Ramesh, C.S., Devaraj, D.S., Keshavamurthy, R., Sridhar, B.R., 2011. Slurry erosive wear behaviour of thermally sprayed Inconel-718 coatings by APS process. Wear 271, 1365–1371.

Ranjan, A., Islam, A., Pathak, M., Khan, M.K., Keshri, A.K., 2019. Plasma sprayed copper coatings for improved surface and mechanical properties. Vacuum 168, 108834.

Ranjan, A., Priy, A., Ahmad, I., Pathak, M., Khan, M.K., Keshri, A.K., 2023. Heat Transfer Characteristics of Pool Boiling with Scalable Plasma-Sprayed Aluminum Coatings.

Langmuir.

Rao, K.V.S., Ramesh, C.S., Girisha, K.G., Rakesh, Y.D., 2017. Slurry Erosive Wear Behavior of Plasma Sprayed Cr_2O_3 Coatings on Steel Substrates. Mater. Today Proc. 4, 10283–10287.

Reddy, A.V., Sundrarajan, G., 1986. Erosion behaviour of ductile materials with a spherical non-friable erodent. Wear 111, 313–323.

Romo, S.A., Santa, J.F., Giraldo, J.E., Toro, A., 2012. Cavitation and high-velocity slurry erosion resistance of welded Stellite 6 alloy. Tribol. Int. 47, 16–24.

Saha, G.C., Mateen, A., Khan, T.I., 2010. Tribological Performance Study of HVOF-Sprayed Microstructured and Nanostructured WC-17wt.% Co Coatings. In: ASME International Mechanical Engineering Congress and Exposition. pp. 153–162.

Sangroula, D.P., 1970. Hydropower Development and Its Sustainability With Respect to Sedimentation in Nepal. J. Inst. Eng. 7, 56–64.

Santa, J.F., Baena, J.C., Toro, A., 2007. Slurry erosion of thermal spray coatings and stainless steels for hydraulic machinery. Wear 263, 258–264.

Santa, J.F., Espitia, L.A., Blanco, J.A., Romo, S.A., Toro, A., 2009. Slurry and cavitation erosion resistance of thermal spray coatings. Wear 267, 160–167.

Senapati, P., KR, R., Padhy, M.K. and Mohanty, U.K., 2017. Quantification of metal loss due to silt erosion under laboratory conditions. International Journal of Mechanical and Production Engineering Research and Development,7(5), 2017, 37-50.

Sharma, A., Kumar, A., Tyagi, R., 2015. Erosive wear analysis of medium carbon dual phase steel under dry ambient condition. Wear 334–335, 91–98.

Sharma, M., Goyal, D.K., Kaushal, G., 2020. Tribological investigation of HVOF sprayed coated turbine steel under varied operating conditions. Mater. Today Proc. 24, 869–879.

Sharma, S.P., Dwivedi, D.K., Jain, P.K., 2008. Effect of CeO_2 addition on the microstructure, hardness, and abrasive wear behaviour of flame-sprayed Ni-based coatings. Proc. Inst. Mech. Eng. Part J J. Eng. Tribol. 222, 925–933.

Shehadeh, M., Anany, M., Saqr, K.M., Hassan, I., 2014. Experimental investigation of erosion-corrosion phenomena in a steel fitting due to plain and slurry seawater flow. Int. J. Mech. Mater. Eng. 9, 1–8.

Shivamurthy, R.C., Kamaraj, M., Nagarajan, R., Shariff, S.M., Padmanabham, G., 2009. Influence of microstructure on slurry erosive wear characteristics of laser surface alloyed 13Cr-4Ni steel. Wear 267, 204–212.

Sidhu, H.S., Sidhu, B.S., Prakash, S., 2007. Solid particle erosion of HVOF sprayed NiCr and

Stellite-6 coatings. Surf. Coatings Technol. 202, 232–238.

Šimuvonic, K., 2010. Thermal spraying welding engineering and technology: thermal spraying. London Ed. Eolss Publ. 1–25.

Singh, A., Kumar, H., Kumar, S., 2022. Development and performance analysis of Ni–$15Cr_2O_3$–$5TiO_2$ and Ni–$15Al_2O_3$–$5TiO_2$ HVOF coatings in erosive fly ash slurry. Surf. Rev. Lett. 2240004.

Singh, B., Zafar, S., 2019. Effect of microwave exposure time on microstructure and slurry erosion behavior of Ni+ 20% Cr_7C_3 composite clads. Wear 426, 491–500.

Singh, J., 2019a. Analysis on suitability of HVOF sprayed Ni-20Al, Ni-20Cr and Al-20Ti coatings in coal-ash slurry conditions using artificial neural network model. Ind. Lubr. Tribol. 71, 972–982.

Singh, J., 2019b. Investigation on slurry erosion of different pumping materials and coatings. Thapar Institute of Engineering and Technology, Patiala, India.

Singh, J., 2021a. A review on mechanisms and testing of wear in slurry pumps, pipeline circuits and hydraulic turbines. J. Tribol. 143, 1–83.

Singh, J., 2021b. Wear performance analysis and characterization of HVOF deposited Ni–$20Cr_2O_3$, Ni–$30Al_2O_3$, and Al_2O_3–$13TiO_2$ coatings. Appl. Surf. Sci. Adv. 6, 100161.

Singh, J., 2021c. Application of Thermal Spray Coatings for Protection against Erosion, Abrasion, and Corrosion in Hydropower Plants and Offshore Industry. In: Thakur, L., Vasudev, H. (Eds.), Thermal Spray Coatings. CRC Press, Boca Raton, pp. 243–283.

Singh, J., 2021d. Slurry erosion performance analysis and characterization of high-velocity oxy-fuel sprayed Ni and Co hardsurfacing alloy coatings. J. King Saud Univ. - Eng. Sci.

Singh, J., 2021e. Tribo-performance analysis of HVOF sprayed 86WC-10Co4Cr & Ni-Cr_2O_3 on AISI 316L steel using DOE-ANN methodology. Ind. Lubr. Tribol. 73, 727–735.

Singh, J., Kumar, S., Gill, H.S., 2023. Review on testing facilities assisting in development of numerical models for erosion calculation in centrifugal slurry pumps. Int. J. Interact. Des. Manuf.

Singh, J., Kumar, S., Mohapatra, S.K., 2018a. Optimization of Erosion Wear Influencing Parameters of HVOF Sprayed Pumping Material for Coal-Water Slurry. Mater. Today Proc. 5, 23789–23795.

Singh, J., Kumar, S., Mohapatra, S.K., 2019a. Erosion wear performance of Ni-Cr-O and NiCrBSiFe-WC(Co) composite coatings deposited by HVOF technique. Ind. Lubr. Tribol. 71, 610–619.

Singh, J., Kumar, S., Mohapatra, S.K., 2019b. An erosion and corrosion study on thermally sprayed WC-Co-Cr powder synergized with $Mo_2C/Y_2O_3/ZrO_2$ feedstock powders. Wear 438–439, 102751.

Singh, J., Kumar, S., Mohapatra, S.K., 2019c. Tribological performance of Yttrium (III) and Zirconium (IV) ceramics reinforced WC–10Co4Cr cermet powder HVOF thermally sprayed on X2CrNiMo-17-12-2 steel. Ceram. Int. 45, 23126–23142.

Singh, J., Kumar, S., Mohapatra, S.K., 2020. Erosion tribo-performance of HVOF deposited Stellite-6 and Colmonoy-88 micron layers on SS-316L. Tribol. Int. 147, 105262.

Singh, J., Kumar, S., Mohapatra, S.K., 2021a. Study on Solid Particle Erosion of Pump Materials by Fly Ash Slurry using Taguchi's Orthogonal Array. Tribol. - Finnish J. Tribol. 38, 31–38.

Singh, J., Kumar, S., Singh, G., 2018b. Taguchi's Approach For Optimization Of Tribo-Resistance Parameters Forss304. Mater. Today Proc. 5, 5031–5038.

Singh, J., Kumar, Satish, Mohapatra, S.K., Kumar, Sagar, 2018c. Shape simulation of solid particles by digital interpretations of scanning electron micrographs using IPA technique. Mater. Today Proc. 5, 17786–17791.

Singh, J., Mohapatra, S.K., Kumar, S., 2021b. Performance analysis of pump materials employed in bottom ash slurry erosion conditions. J. Tribol. 30, 73–89.

Singh, J., Nath, S.K., 2022. Surface and bulk modification techniques to mitigate silt erosion in hydro turbines: a review of techniques and parameters. Surf. Eng. 38, 288–302.

Singh, J., Singh, J.P., 2021a. Numerical Analysis on Solid Particle Erosion in Elbow of a Slurry Conveying Circuit. J. Pipeline Syst. Eng. Pract. 12, 04020070.

Singh, J., Singh, J.P., 2022. Performance analysis of erosion resistant Mo_2C reinforced WC-CoCr coating for pump impeller with Taguchi's method. Ind. Lubr. Tribol. 74, 431–441.

Singh, J., Singh, J.P., Singh, M., Szala, M., 2019d. Computational analysis of solid particle-erosion produced by bottom ash slurry in 90° elbow. MATEC Web Conf. 252, 04008.

Singh, J., Singh, S., 2021b. Neural network prediction of slurry erosion of heavy-duty pump impeller/casing materials 18Cr-8Ni, 16Cr-10Ni-2Mo, super duplex 24Cr-6Ni-3Mo-N, and grey cast iron. Wear 476, 203741.

Singh, J.P., Kumar, S., Mohapatra, S.K., 2017. Head Loss Investigations Inside 90° Pipe Bend for Conveying Of Fine Coal–Water Slurry Suspension. Int. J. Coal Prep. Util. 00, 1–17.

Singh, V., Kumar, S., Ratha, D., 2020. Optimization of Al_2O_3 and TiO_2 Blends to be Used as Erosion Resistant Coating for Mild Steel. J. Tribol. 142.

Singh, V.P., Sil, A., Jayaganthan, R., 2012. Tribological behaviour of nanostructured Al_2O_3

coatings. Surf. Eng. 28, 277–284.

Singh, V.P., Sil, A., Jayaganthan, R., 2014. Evaluation of dry sliding and slurry erosion behaviour of plasma sprayed nanostructured Cr_2O_3–$3TiO_2$ coatings. Tribol. Surfaces Interfaces 8, 131–138.

Sobolev, V.V., Guilemany, J.M., Nutting, J., Joshi, S., 2004. High velocity oxy-fuel spraying: theory, structure-property relationships and applications. Maney London.

Stack, M.M., Pungwiwat, N., 1999. Slurry erosion of metallics, polymers, and ceramics: Particle size effects. Mater. Sci. Technol. 15, 337–344.

Stojanovic, B., Blagojevic, J., Babic, M., Velickovic, S., Miladinovic, S., 2017. Optimization of hybrid aluminum composites wear using Taguchi method and artificial neural network. Ind. Lubr. Tribol. 69, 1005–1015.

Sugiyama, K., Nakahama, S., Hattori, S., Nakano, K., 2005. Slurry wear and cavitation erosion of thermal-sprayed cermets. Wear 258, 768–775.

Sundararajan, G., Roy, M., Venkataraman, B., 1990. Erosion efficiency-a new parameter to characterize the dominant erosion micromechanism. Wear 140, 369–381.

Swarnakar, N.K., Rao, V.S., Tripathi, S., 2008. Innovative use of technology to curb the menace of silt erosion in hydro turbines. Water Energy Abstr. 18, 27–28.

Szala, M., Awtoniuk, M., Łatka, L., Macek, W., Branco, R., 2021. Artificial neural network model of hardness, porosity and cavitation erosion wear of APS deposited Al_2O_3-13 wt% TiO_2 coatings. J. Phys. Conf. Ser. 1736, 012033.

Szala, M., Hejwowski, T.J., Lenart, I., 2014. Cavitation erosion resistance of Ni-Co based coatings. Adv. Sci. Technol. Res. J. 8, 36–42.

Szala, M., Łatka, L., Walczak, M., Winnicki, M., 2020. Comparative Study on the Cavitation Erosion and Sliding Wear of Cold-Sprayed Al/Al2O3 and Cu/Al_2O_3 Coatings, and Stainless Steel, Aluminium Alloy, Copper and Brass. Metals 10, 1–24.

Szala, M., Łukasik, D., 2016. Cavitation Wear of Pump Impellers. J. Technol. Exploit. Mech. Eng. 2, 40–44.

Taguchi, G., 1990. Introduction to Quality Engineering. Tokyo.

Talib, R.J., Saad, S., Toff, M.R.M., Hashim, H., 2003. Thermal spray coating technology: A review. Solid State Sci Technol 11, 109–117.

Thakur, L., Arora, N., 2013. A comparative study on slurry and dry erosion behaviour of HVOF sprayed WC–CoCr coatings. Wear 303, 405–411.

Thapa, B., Brekke, H., 2004. Effect of sand particle size and surface curvature in erosion of hydraulic turbine. In: IAHR Symposium on Hydraulic Machinery and Systems.

Stockholm.

Tianmin, S., Meng, H., Yuen, T.H., 2003. Impact wear behavior of laser hardened hypoeutectoid 2Cr13 martensite stainless steel. Wear 255, 444–455.

Tilly, G.P., 1973. A two stage mechanism of ductile erosion. Wear 23, 87–96.

Tucker Jr, R.C., 1994. Advanced thermal spray deposition techniques. Handb. Depos. Technol. Film. Coatings.

Turenne, S., Châtigny, Y., Simard, D., Caron, S., Masounave, J., 1990. The effect of abrasive particle size on the slurry erosion resistance of particulate-reinforced aluminium alloy. Wear 141, 147–158.

Vashishtha, N., Khatirkar, R.K., Sapate, S.G., 2017. Tribological behaviour of HVOF sprayed WC-12Co, WC-10Co-4Cr and Cr_3C_2−25NiCr coatings. Tribol. Int. 105, 55–68.

Vasudev, H., Prashar, G., Thakur, L., Bansal, A., 2021. Electrochemical Corrosion Behavior and Microstructural Characterization of HVOF Sprayed Inconel-718 Coating on Gray Cast Iron. J. Fail. Anal. Prev. 21, 250–260.

Vasudev, H., Thakur, L., Singh, H., Bansal, A., 2020. A study on processing and hot corrosion behaviour of HVOF sprayed Inconel718-nano Al_2O_3 coatings. Mater. Today Commun. 25, 101626.

Vasudev, H., Thakur, L., Singh, H., Bansal, A., 2022. Effect of addition of Al_2O_3 on the high-temperature solid particle erosion behaviour of HVOF sprayed Inconel-718 coatings. Mater. Today Commun. 30, 103017.

Veličković, S., Stojanović, B., Babić, M., Bobić, I., 2017. Optimization of tribological properties of aluminum hybrid composites using Taguchi design. J. Compos. Mater. 51, 2505–2515.

Verdon, C., Karimi, A., Martin, J.-L., 1998. A study of high velocity oxy-fuel thermally sprayed tungsten carbide based coatings. Part 1: Microstructures. Mater. Sci. Eng. A 246, 11–24.

Verma, M., 1999. Silt friendly design of turbine and other water components. In: First International Conference on Silting Problem in Hydropower Plants (CBIP). New Delhi, pp. 1–10.

Vuorinen, P., Siitonen, P., Ojala, N., Valtonen, K., Kivikyto, P., Kuokkala, V., 2014. Effect of test parameters on large particle high speed slurry erosion testing. Tribology 8, 98–104.

Wada, S., Watanabe, N., 1987. Solid Particle Erosion of Brittle Materials (Part 3). J. Ceram. Assoc. Japan 95, 573–578.

Wahab, J.A., Ghazali, M.J., 2019. Erosion resistance of laser textured plasma-sprayed Al_2O_3-13%TiO_2 coatings on mild steel. Wear 432–433, 202937.

Walker, C.I., Hambe, M., 2015. Influence of particle shape on slurry wear of white iron. Wear 332–333, 1021–1027.

Wang, K.L., Zhang, Q.B., Sun, M.L., Wei, X.G., Zhu, Y.M., 2001. Rare earth elements modification of laser-clad nickel-based alloy coatings. Appl. Surf. Sci. 174, 191–200.

Wang, Y., Chen, W., Wang, L., 2003. Micro-indentation and erosion properties of thermal sprayed NiAl intermetallic-based alloy coatings. Wear 254, 350–355.

Wang, Y.F., Yang, Z.G., 2008. Finite element model of erosive wear on ductile and brittle materials. Wear 265, 871–878.

Wang, H.Z., Cheng, Y.H., Zhang, X.C., Yang, J.Y. and Cao, C.M., 2020. Effect of laser scanning speed on microstructure and properties of Fe based amorphous/nanocrystalline cladding coatings. Mater. Chem. Phys. 250, 123091.

Wang, H.Z., Cheng, Y.H., Yang, J.Y. and Wang, Q.Q., 2021. Influence of laser remelting on organization, mechanical properties and corrosion resistance of Fe-based amorphous composite coating. Surf. Coat. Technol. 414, 127081.

Wei, R., Langa, E., Rincon, C., Arps, J.H., 2006. Deposition of thick nitrides and carbonitrides for sand erosion protection. Surf. Coatings Technol. 201, 4453–4459.

Wiederhorn, S.M., Hockey, B.J., 1983. Effect of material parameters on the erosion resistance of brittle materials. J. Mater. Sci. 18, 766–780.

Woldman, M., van der Heide, E., Schipper, D.J., Tinga, T., Masen, M.A., 2012. Investigating the influence of sand particle properties on abrasive wear behaviour. Wear 294–295, 419–426.

Yadav, A.S., Mishra, S.B., 2013. Slurry erosive wear study of d-gun sprayed coatings on SAE 431. In: 2013 International Conference on Control, Computing, Communication and Materials (ICCCCM). IEEE, pp. 1–5.

Yang, K., Zhou, X., Zhao, H., and Tao, S. 2011. Microstructure and mechanical properties of Al_2O_3–Cr_2O_3 composite coatings produced by atmospheric plasma spraying. Surf. Coat. Technol. 206(6), 1362-1371.

Yang, K., Rong, J., Liu, C., Zhao, H., Tao, S., Ding, C., 2016. Study on erosion–wear behavior and mechanism of plasma-sprayed alumina-based coatings by a novel slurry injection method. Tribol. Int. 93, 29–35.

Yarrapareddy, E., Zekovic, S., Hamid, S., Kovacevic, R., 2006. The development of nickel-tungsten carbide functionally graded materials by a laser-based direct metal deposition process for industrial slurry erosion applications. Proc. Inst. Mech. Eng. Part B J. Eng. Manuf. 220, 1923–1936.

Yuan, J., Cheng, Y., Jing, Z., Xu, L., Mao, J., Lu, W., Zhang, Z. and Liang, X., 2023. Properties of Al-Based Amorphous Coatings Prepared by Low-temperature HVOF Spraying. Journal of Therm. Spray Technol. https://doi.org/10.1007/s11666-023-01555-9

Zamani, P., Valefi, Z., Jafarzadeh, K., 2022. Comprehensive study on corrosion protection properties of Al_2O_3, Cr_2O_3 and Al_2O_3–Cr_2O_3 ceramic coatings deposited by plasma spraying on carbon steel. Ceram. Int. 48, 1574–1588.

Zhang, D., Zhang, X., 2005. Laser cladding of stainless steel with Ni–Cr_3C_2 and Ni–WC for improving erosive–corrosive wear performance. Surf. Coatings Technol. 190, 212–217.

Zhang, Z., Lu, X., Han, B., and Luo, J. 2007. Rare earth effect on the microstructure and wear resistance of Ni-based coatings. Mater. Sci. Eng.: A 454, 194-202.

Zhang, Z., Yuan, J., Jing, Z., Cheng, Y. and Liang, X., 2022. Research Progress and Development Trend of Amorphous and Nanocrystalline Composite Coatings: A Review. JOM 74(12), 4597-4611.

Zou, R.P., Yu, A.B., 1996. Evaluation of the packing characteristics of mono-sized non-spherical particles. Powder Technol. 88, 71–79.

Zu, J.B., Ihtchings, I.M., Burstein, G.T., 1990. Design of a slurry erosion test rig. Wear 140, 331–344.

PERMISSIONS OF THIRD-PARTY MATERIAL

- Figure 1.2(a,b), *Copyright of reproduction in thesis on license number: 5562430707651, issued on date 05 Jun 2023 by Elsevier.*
- Figure 1.2(c), *Copyright of reproduction in thesis on license number: 45562400644423, issued on date 05 Jun 2023 by Elsevier.*
- Figure 1.5, *Copyright of reproduction in thesis on license number: 5562401304886, issued on date 05 Jun 2023 by Elsevier.*
- Figure 1.6, *Copyright of reproduction in thesis on license number: 5562410254129, issued on date 05 Jun 2023 by Elsevier.*
- Figure 1.8, *Copyright of reproduction in thesis on license number: 5562410618278, issued on date 05 Jun 2023 by Elsevier.*
- Figure 1.9, *Copyright of reproduction in thesis on license number: 5562421376306, issued on date 05 Jun 2023 by Elsevier.*
- Figure 1.10, *Copyright of reproduction under Creative Commons Attribution License (http://creativecommons.org/licenses/by/4.0) by Springer Nature.*
- Figure 1.11, *Copyright of reproduction in thesis on license number: 5562420352705, issued on date 05 Jun 2023 by Elsevier.*
- Figure 1.12, *Copyright of reproduction in thesis on license number: 5562430283366, issued on date 05 Jun 2023 by Springer Nature.*